Diss. 2011 - 05
August

Quasi-Free-Scattering and One-Proton-Removal Reactions with the Proton-Dripline Nucleus ^{17}Ne at Relativistic Beam Energies

Felix Wamers

(Dissertation der Technischen Universität in Darmstadt)

GSI Helmholtzzentrum für Schwerionenforschung GmbH
Planckstraße 1 · D-64291 Darmstadt · Germany
Postfach 11 05 52 · D-64220 Darmstadt · Germany

Institut für Kernphysik
Technische Universität Darmstadt

Kernreaktionen und
Nukleare Astrophysik
GSI Helmholtzzentrum für
Schwerionenforschung GmbH

Quasi-Free-Scattering and One-Proton-Removal Reactions with the Proton-Dripline Nucleus ^{17}Ne at Relativistic Beam Energies

Vom Fachbereich Physik
der Technischen Universität Darmstadt
zur Erlangung des Grades
eines Doktors der Naturwissenschaften
(Dr. rer. nat.)

genehmigte Dissertation von

Dipl.-Phys. Felix Wamers
aus Münster

Darmstadt 2011

D17

Referent:	Prof. Dr. Thomas Aumann
Korreferent:	Prof. Dr. Dr. h.c. RUS Dieter H. H. Hoffmann

Tag der Einreichung:	12.04.2011
Tag der mündlichen Prüfung:	18.05.2011

Abstract

The Borromean proton-dripline nucleus and two-proton-halo candidate ^{17}Ne has been studied in exclusive measurements of one-proton-removal reactions in inverse kinematics, *i.e.*, *via* ^{17}Ne(target,target+p)^{16}F$\rightarrow^{15}$O+p reactions observed at the R^{3}B/LAND setup at GSI in Darmstadt, Germany. Secondary ^{17}Ne beams at approximately 500 AMeV have been directed onto polyethylene (CH_2) and carbon (C) targets in order to examine the residues of proton-induced, *i.e.*, quasi-free (p,2p), as well as of carbon-induced one-proton removal from the ^{17}Ne = ^{15}O+2p three-body system. The excitation energy of the resulting unbound and instantly decaying ^{16}F has been measured *via* the relative energy between its projectile-like constituents, ^{15}O+p. The different channels of proton knockout from halo and core states in ^{17}Ne have been identified and separated *via* the selection of low- or high-energy regions in the ^{15}O+p relative-energy spectrum, corresponding either to low negative- or to high positive-parity states in ^{16}F, respectively.

The transverse (x/y) momentum distributions of the proton-unbound ^{16}F fragment after the halo-proton removal from ^{17}Ne have been reconstructed from experimental measurements and interpreted using a Glauber-model-based code. Calculated ^{16}F transverse-momentum distributions resulting from an s- or d-proton knockout from ^{17}Ne have been used to fit the experimental distributions in a weighted superposition. The fit describes the data very well, and relative weights for the s-content of $w_x(s^2) = 38.3\pm1.3(\text{stat})\,\%$ and $w_y(s^2) = 42.3\pm1.3(\text{stat})\,\%$ have been extracted within a single-particle picture. A weighted average of $w_{\text{avg}}(s^2) = 40.8\pm1.3(\text{stat})\pm4.0(\text{syst})\,\%$ has been determined.

While analysing the x and y projections of the momentum distribution separately, the s-wave content for the two valence protons in the ^{17}Ne ground state has been obtained from two independent measurements. Compared to theoretical predictions of 40-50 % for that s-wave content, the obtained averaged value of approximately 41 % is in good agreement, suggesting a moderately expressed halo- character of the ^{17}Ne = ^{15}O+2p system.

Quasi-free (p,2p) scattering reactions with ^{17}Ne beams on a proton-rich CH_2 target have been studied in inverse kinematics. The typical kinematical (angle and energy) correlations, known from free p-p scattering, have been observed for the (p,2p) proton pairs with high angular resolution. The background stemming from the carbon content of the CH_2 target does not show these kinematical correlations and can be understood qualitatively and quantitatively. In prospect to the future R^{3}B experiment at FAIR, quasi-free scattering in inverse kinematics has been shown to be a clean tool for nuclear-structure studies with exotic beams, being feasible even with thick compound targets like polyethylene.

The measurements have been performed in complete kinematics at the R^{3}B/LAND setup in Cave C at GSI. The final-state excitation energy in the exit channel of the reaction has been reconstructed using the invariant-mass technique. Tracking and identification of the incoming beam and of the outgoing fragments have been performed by means of time-of-flight and tracking techniques, combined with a charge-to-mass-ratio-based separation in the final state *via* the ALADIN dipole magnet.

Recoil protons from direct reactions, such as quasi-free (p,2p) scattering or carbon-induced knockout, have been detected at large angles using a new array of high-resolution Si-strip detectors (for the angular measurement) combined with the 2π-NaI-shell of the surrounding Crystal Ball (for proton-energy measurement and triggering). For this purpose, a new high-energy readout of the Crystal Ball was designed, tested, and installed within the framework of this thesis.

Zusammenfassung

Der borromäische Protonen-Dripline-Kern und Zwei-Proton-Halo-Kanditat ^{17}Ne wurde in direkten Reaktionen vom Typ ^{17}Ne(Target,Target+p)^{16}F$\rightarrow^{15}$O+p in inverser Kinematik am R^{3}B/LAND Aufbau an der GSI in Darmstadt untersucht. Dazu wurden sekundäre Strahlen von ^{17}Ne-Kernen bei relativistischen Energien (500 AMeV) in leichten Plastik- und Kohlenstoff-Targets mittels protonen-, d.h. quasifreier (p,2p)-, wie auch kohlenstoff-induzierter Ein-Protonen-Knockout-Reaktionen aufgebrochen und deren Fragmente kinematisch vollständig vermessen. Die Anregungsenergie des ungebundenen ^{16}F, welches aus der Herauslösung eines Protons aus dem ^{17}Ne = ^{15}O+2p Dreikörpersystem resultiert, wurde mittels der Relativenergie seiner projektilartigen instantanen Zerfallsprodukte bestimmt. Protonen-Knockout-Kanäle aus Kern- oder aus Halo-Zuständen des ^{17}Ne, welche zu Zuständen negativer oder positiver Parität des resultierenden ^{16}F führen, wurden als niedriger oder höher angeregte Regionen im ^{15}O+p Relativenergiespektrum identifiziert.

Die transversalen Impulsverteilungen des ungebundenen ^{16}F = ^{15}O+p Fragments nach Haloprotonablösung aus dem ^{17}Ne-Projektil sind experimentell bestimmt und mit Hilfe eines auf dem Glauber-Modell basierenden Programms interpretiert worden. Berechnete transversale ^{16}F Impulsverteilungen nach s- oder d-Protonen-Knockout aus ^{17}Ne sind an die experimentellen Verteilungen als gewichtete Superposition angepasst worden. Der Fit beschreibt die Daten sehr gut, und im Einteilchenbild wurde der relative s-Wellenanteil im ^{17}Ne-Valenzprotonenpaar in der x-Projektion zu $w_x(s^2) = 38.3\pm1.3(\text{stat})\,\%$, und in der y-Projektion zu $w_y(s^2) = 42.3\pm1.3(\text{stat})\,\%$ extrahiert. Ein gewichteter Mittelwert von $w_{\text{avg}}(s^2) = 40.8\pm1.3(\text{stat})\pm4.0(\text{syst})\,\%$ ist bestimmt worden.
In der unabhängigen Analyse der x- und y-Projektion der ^{16}F Transversalimpulsverteilung wurde der s-Wellenanteil der beiden Valenzprotonen des ^{17}Ne Grundzustands über zwei Messungen ermittelt. Im Vergleich zu theoretischen Vorhersagen von 40-50 % s-Wellenanteil erweist sich der innerhalb dieser Arbeit extrahierte Mittelwert von etwa 41 % in guter Übereinstimmung und stellt damit eine moderate Halo-Ausprägung im ^{17}Ne = ^{15}O+2p System dar.

Weiterhin wurden protoneninduzierte (p,2p) Knockout-Reaktionen an ^{17}Ne-Kernen in einem protonenreichen CH_2-Target untersucht, also quasifreie Streuung in inverser Kinematik. Die typischen, von freier pp-Streuung bekannten, kinematischen (Winkel- und Energie-) Korrelationen der (p,2p) Protonenpaare wurden mit hoher Winkelauflösung beobachtet. Der auf den Kohlenstoffinhalt des CH_2-Targets bezogene Untergrund ist qualitativ und quantitativ untersucht worden und weist diese kinematischen Korrelationen nicht auf. Im Ausblick auf das zukünftige R^{3}B-Experiment bei FAIR hat sich quasifreie Streuung als präzises Werkzeug für Untersuchungen zur Kernstruktur mit exotischen Strahlen erwiesen, auch unter Verwendung protonenreicher Mischtargets wie zum Beispiel CH_2.

Die Messungen wurden am kinematisch vollständigen R^{3}B/LAND-Aufbau in Cave C an der GSI durchgeführt. Die Anregungs- bzw. Relativenergie der Endzustandsprodukte einer Reaktion wurde über das Prinzip der invarianten Masse rekonstruiert. Die Identifikation

und die Charakterisierung der Strahlteilchen im Eingangskanal und der Fragmente im Ausgangskanal wurden mittels Flugzeit- und Tracking-Techniken in Kombination mit einer A/Q-Separation im ALADIN-Dipolmagneten realisiert.
Rückstoßprotonen aus direkten Reaktionen, wie zum Beispiel nach quasifreier (p,2p) Streuung, aber auch nach kohlenstoffinduziertem Knockout, wurden unter großen Laborwinkeln mit Hilfe eines neuartigen Aufbaus hochauflösender Silizium-Streifendetektoren (für die Winkelmessung) sowie in der 2π-NaI-Schale des umgebenden Crystal Balls (als Trigger und zur Messung der Protonenenergie) nachgewiesen. Zu diesem Zweck wurde im Rahmen dieser Arbeit eine neue zweistufige Auslese für Energieverlustmessungen im Crystal Ball entworfen, getestet und in Betrieb genommen.

Table of Contents

1 Introduction **1**

2 Light Exotic Nuclei **7**

2.1 Halo Nuclei 7

2.2 Direct Nuclear Reactions for Nuclear Spectroscopy 10

2.2.1 One-Nucleon-Removal Reactions on Light Nuclear Targets 13

2.2.2 Quasi-Free-Scattering Reactions on Protons 16

3 Experimental Setup **19**

3.1 The GSI Heavy-Ion Laboratory 19

3.1.1 The Fragment Separator FRS 20

3.2 The R^3B/LAND setup in Cave C 22

3.2.1 In Front of the Target 22

3.2.2 Behind the Target 24

3.2.3 At and Around the Target 26

3.2.4 Data Acquisition and Triggers 32

4 Calibration and Reconstruction **37**

4.1 Overview of the land02 Calibration and Analysis Software 37

4.2 Identification of the Incoming Beam 39

4.3 Identification of Outgoing Particles 39

4.3.1 Heavy Fragments 40

4.4 Calibration of the SST detectors 40

4.4.1 Charge and Position of Ion Hits 41

4.4.2 Inter-Strip Dependence and η-Correction 43

4.4.3 Gain Correction 43

4.4.4 Dead Strips and More 43

4.4.5 SSTs for Fragment-Charge Identification 45

4.5 Calibration of the Crystal Ball 46

4.5.1 Crystal Ball γ-Readout 47

4.5.2 Crystal Ball Proton Readout 52

4.6 Hit Reconstruction with the Crystal Ball 55

4.6.1 Addback Algorithm for Proton and Gamma Clusters 55

5 Analysis Techniques **59**
5.1 Reaction Cross Sections . . . 59
5.1.1 Formalism and Approximations . . . 60
5.1.2 Background Subtraction . . . 61
5.1.3 Fragment-Mass Cut . . . 61
5.2 Tracking: Fragments and Protons . . . 63
5.2.1 Angle Measurement at the Target . . . 64
5.3 The Invariant-Mass Technique . . . 68

6 Results and Discussion **71**
6.1 Quasi-Free (p,2p) Scattering in Inverse Kinematics . . . 71
6.1.1 Recoil-Proton Multiplicity . . . 72
6.1.2 Angular Correlations Between Recoil-Proton Pairs . . . 73
6.1.3 Kinetic Energy of Recoil Protons . . . 78
6.1.4 Improvements of the Recoil-Proton Detection — a Discussion . . . 80
6.1.5 Inverse-Kinematics QFS — Conclusions . . . 81
6.2 One-Proton Removal from ^{17}Ne — Relative Energy of the Unbound ^{16}F . . . 81
6.2.1 Projectile-like Protons . . . 81
6.2.2 ^{15}O+p Relative-Energy Spectrum . . . 83
6.3 Inclusive Two-Proton-Removal Cross Sections . . . 84
6.4 Transverse-Momentum Distributions of Fragments . . . 85
6.4.1 Angular Resolution of the Setup . . . 87
6.4.2 Transverse-Momentum Resolution . . . 89
6.4.3 ^{16}F Transverse-Momentum Distributions . . . 91

7 Conclusions and Outlook **95**

A Crystal Ball Randomisation **97**
A.1 Purpose of the Program . . . 97
A.2 Programme Source and Usage . . . 97
A.2.1 geom_input . . . 98
A.2.2 standalone . . . 98
A.2.3 rootplugin . . . 98
A.3 Programme Working Principle . . . 99
A.3.1 Overview . . . 99
A.3.2 Details . . . 99
A.4 Overlapping Crystals . . . 100

B Simulation of the Crystal Ball Response to High-Energy Protons **103**

C Crystal Ball Puzzle **105**

Bibliography **116**

1

Introduction

The presented work adds to the field of nuclear-structure physics, the discipline which studies the properties of nuclei in terms of the arrangement of their intrinsic constituents, the protons and neutrons. The particular focus of this thesis is set on light and weakly bound nuclei, in the presented case onto the Borromean proton-dripline nucleus ^{17}Ne.

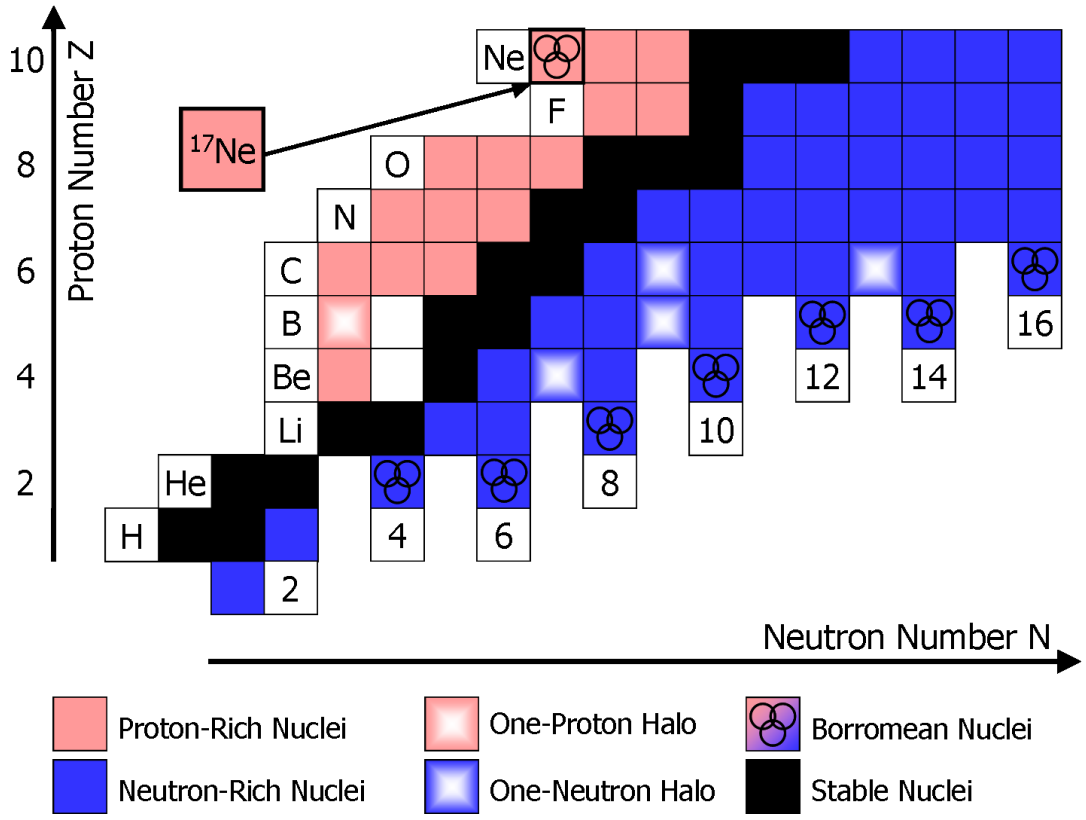

Figure 1.1: Origin of the chart of nuclides, showing light bound isotopes in the region of Z≤10 and N≤16. Black squares represent stable nuclides, whereas the red and blue ones are unstable towards β^+ and β^- decay, respectively. One-nucleon-halo nuclei and Borromean nuclei, which are typically two-nucleon halos, are indicated. The particular focus of interest of the present work, the Borromean proton-dripline nucleus ^{17}Ne, is located at the very top left of the diagram.

The origin of most of today's theoretical models that describe the structure of nuclei is the shell model developed in the late 1940s by Maria Goeppert-Mayer and Hans Jensen [1, 2]. By describing the nucleons as quantum-mechanical fermions, and their motion and interactions within a nucleus via a common radial potential — effectively created by the

superposition of two-body interactions within the whole ensemble of all nucleons, but acting as a mean potential on each individual of them — with a central and also a strong spin-orbit component (plus the Coulomb potential for the protons), many properties of stable nuclei with magic proton- and neutron numbers (2, 8, 20, 28, 50, 82, 126), can be reproduced and understood.

(a) Borromean rings formed from snap-light sticks.

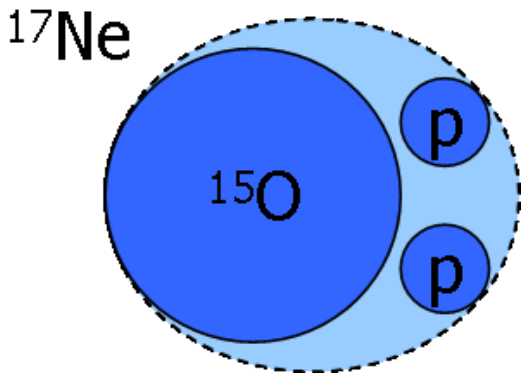

(b) Pictogram of the ^{17}Ne 3-body structure.

Figure 1.2: Artistic impressions of the ^{17}Ne structure. (a) A photograph of a Borromean-ring system made of three combinable plastic sticks (one pink, two yellow). (b) ^{17}Ne seen as consisting of a ^{15}O core and two valence-/halo-protons.

When moving away from the so-called valley of stability *via* the addition of large numbers of protons or neutrons to a nucleus, *i.e.*, when studying very neutron-proton-asymmetric nuclei, the description of the net forces between the nucleons assumed in the shell model becomes less and less valid. For example, the spin-orbit coupling between the nucleons decreases due to increasing diffuseness of the nuclear surface. As a consequence for very proton- or neutron-rich and thus weakly bound nuclei, established magic numbers may disappear and instead new ones can be found [3]. One finds also an inversion or rearrangement of energy levels for these nuclei. Structural novelties, like the formation of neutron skins around a proton-neutron-balanced core for medium-mass to heavy neutron-rich nuclei have been observed.

A particularly interesting phenomenon, discovered for very light exotic[1] nuclei, is the phenomenon of halos. Those are nuclei with a compact core and one or two relatively loosely bound nucleons at a considerably large average distance that in turn leads to a rather dilute matter distribution. Figure 1.1 shows the origin of the nuclear landscape, featuring the region of the lightest hydrogen (Z=1) to neon (Z=10) isotopes. Since the early 1980s a number of nuclei with a halo-like structure have been discovered close to the neutron dripline, for example ^{11}Be or ^{19}C with a one-neutron halo, or ^{11}Li and ^{6}He with a two-neutron halo. The valence neutrons that form these halos have all been found to reside in low-orbital-momentum states of either $l = 0$ (s) or $l = 1$ (p). Those are configurations with no (or a small) additional angular-momentum potential barrier, which in turn explains their feature of being found at relatively large, classically forbidden, distances from the centre

[1]The attribute 'exotic' has a similar in meaning as 'rare', or 'unstable', or 'radioactive'. It refers to the fact that such nuclei are not naturally found on Earth, but have to be artificially produced in laboratories.

of the nucleus. In comparison, protons as the valence nucleons of very proton-rich nuclei are subject to an additionally confining Coulomb-potential barrier, making nuclei with a strongly pronounced proton-halo less likely to exist. Nevertheless, some have been discovered, like the one-proton halos of ^{8}B and of the first excited state of ^{17}F. The strongest candidate for the first ever two-proton-halo nucleus to be discovered, however, is ^{17}Ne, the lightest bound neon isotope with a half-life of 109 ms [4]. ^{17}Ne is a ^{15}O+2p three-body system with the two valence protons very loosely bound by only S_{2p}=950 keV, and like the two-neutron halo nuclei it is a Borromean[2] system, *i.e.* all its binary subsystems (^{15}O+p, and p+p) are unbound. Figure 1.2a and figure 1.2b visualise the idea of Borromean rings and of the ^{17}Ne three-body structure.

Various experimental and theoretical studies have been undertaken in the recent 20 years in order to solve the question of the possible two-proton-halo nature of ^{17}Ne, and although a majority of reports confirm or favour that, yet a final conclusion is lacking as will be discussed in the following. Within the shell-model picture, a crucial role plays the configuration of the two valence protons, occupying either the $0d_{5/2}$ or $1s_{1/2}$ orbitals [5], as sketched in figure 1.3.

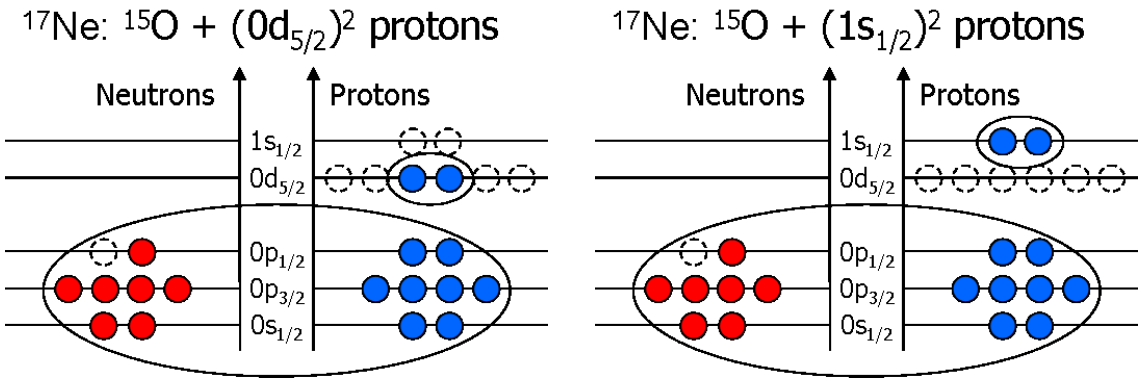

(a) Shell-model view of ^{17}Ne with its two valence protons in a d^2 configuration.

(b) Shell-model view of ^{17}Ne with its two valence protons in a s^2 configuration.

Figure 1.3: Shell-model description of the two predominant configurations of the seven neutrons and ten protons in ^{17}Ne. All protons being paired, spin and parity of the ground state are defined by the missing neutron to complete the $0p_{1/2}$ shell, being $J^\pi = 1/2^-$. The neutrons together with the magic number of eight protons in the 0s and 0p shells form a core of ^{15}O. The remaining two valence protons are very lightly bound by only ∼950 keV, and form pair-states in either the $0d_{5/2}$ (a) or the $1s_{1/2}$ (b) shell.

The first indication for ^{17}Ne's anomalous structure was found by studying the first-forbidden beta decay [6–8] into the first excited state in ^{17}F. It exhibited a 1.6 times larger branching ratio than expected from the mirror decay of ^{17}N into ^{17}O, which was explained by a very large spatial extent of the $1s_{1/2}$ orbit. An interaction-cross-section measurement [9] exploring the A=17 isobars revealed an rms matter radius of 2.75(07) fm for ^{17}Ne, larger

[2]The term Borromean refers to an old Italian family whose crest shows three rings, linked in such a way that when one is taken away the other two also fall apart.

than the one of its mirror nucleus ^{17}N with 2.48(05) fm, being attributed to the two valence protons occupying the $1s_{1/2}$ orbital [10]. Furthermore, the ^{15}O momentum distribution, resulting from beams of ^{17}Ne at 66 AMeV of which two protons were stripped off, was found to be narrow with an FWHM of 168(17) MeV/c. The corresponding two-proton-removal cross section turned out to be also large, with 191(48) mb. Both values were interpreted as signatures for a strong s-wave occupation and thus a good halo evidence of the valence protons [11, 12]. However, these arguments are weakened by the reasoning in theoretical publications [5, 13], that the measurements were not exclusively sensitive to the knock-out from halo states, but from core states also. Based on calculations with a three-body model of ^{17}Ne the statement is supported, however, that an s-wave-occupation ratio of about 50 % for the two valence protons should be a good signature for their halo nature. In an experimental-theoretical joint venture published in 2008 [14], the measurement of the ^{17}Ne charge radius of $r_{\mathrm{ch,exp}} = 3.042(21)$ fm, extracted from the isotope shift obtained *via* collinear laser spectroscopy and a Penning-trap mass measurement, was combined with theoretical FMD-type calculations of the ^{17}Ne matter and charge radii, leading to basically the same value for the charge radius of $r_{\mathrm{ch,theo}} = 3.04$ fm. That value allowed for a consistent deduction of an s^2-admixture in ^{17}Ne of 42 %, close to the 50 % halo-signature threshold postulated in [5]. Furthermore, the ^{17}Ne matter-density distribution derived from the FMD-type calculation presented in [14] shows a significant enhancement of the average radius of protons over the one of neutrons, yielding a 'proton-skin' thickness of 0.45 fm. In contradiction to that, quite recently in another three-body-model calculation employed to study the possible diproton correlations in ^{17}Ne, an s^2-admixture in the ^{17}Ne ground state of only about 15 % was found [15]. Furthermore, the ^{17}Ne density distribution was studied in reaction-cross-section (σ_R) measurements [10, 16]. *Via* the support from Glauber-type calculations, a similarly long tail of the ^{17}Ne density distribution as in [14] was found and finally interpreted as being consistent with a dominant s^2 configuration of the two valence protons [16]. A second conclusion from [16] was that the case of ^{17}Ne suggests a $0d_{5/2} \leftrightarrow 1s_{1/2}$ change in the shell-structure-ordering in the sd-shell region for proton-rich nuclei.

But ^{17}Ne has also raised interest in the neighbouring fields of two-proton radioactivity and nuclear astrophysics [17, 18]: Under usual stellar conditions (temperature, density), the CNO-cycle[3] has its main breakout *via* the ^{15}O(α,γ)^{19}Ne reaction. In particularly hot and dense stellar environments, ^{15}O(2p,γ)^{17}Ne has been considered as an alternative breakout or bypass process. This could be especially important for the rp-process[4] in X-ray bursts. Based on their three-body model of ^{17}Ne, Grigorenko et al. have suggested [18] that direct diproton-capture reactions on ^{15}O should be taken into account — additionally to the 'standard' two-step (^{15}O+p)+p processes *via* resonant states in ^{16}F already considered in [17]. By doing so, their calculations lead to a total ^{15}O(2p,γ)^{17}Ne stellar reaction rate enhanced by up to five orders of magnitude. Accordingly, the question here is whether a correspondingly high diproton-capture cross section on ^{15}O can be measured and confirmed experimentally. An enhanced cross-section for direct 2p-capture on ^{15}O would, on the other

[3] The CNO cycle is the carbon-nitrogen-oxygen stellar nuclear-burning cycle that produces energy from the indirect transformation of ^{4}H to ^{4}He, and as a side effect breeds heavier elements out of carbon, and *ergo* represents a major contribution to the stellar nucleosynthesis processes.

[4] The astrophysical rapid-proton-capture (rp) process is a stellar-nucleosynthesis process that takes place in explosive scenarios like X-ray bursts, leading to the genesis of very proton-rich nuclei.

hand, also represent a signature for a significant probability for a two-proton radioactivity of ^{17}Ne. This relatively rare decay mode has been investigated in [19] but has not yet been observed, unlike for the recent case of ^{19}Mg (=^{17}Ne+2p) [20].

The experimental approach — pursued by the R^{3}B collaboration during the "S318" experimental campaign at the R^{3}B/LAND setup at GSI[5] in 2007 — to study these interesting aspects of ^{17}Ne was multifold. Secondary ^{17}Ne beams at about 500 AMeV were guided onto Pb, C, and CH_2 targets in order to study the following reactions:

- Continuum excitation of ^{17}Ne *via* Coulomb dissociation. The energy-differential Coulomb cross section may be transformed into the corresponding photo-dissociation cross section *via* the virtual-photon theory. By further applying the detailed balance theorem, the cross section of the inverse reaction relevant for nuclear astrophysics can be calculated, *i.e.*, of radiative diproton capture on ^{15}O. Therefore, the study of Coulomb excitation to the ^{15}O+p+p continuum also yields necessary insight about the nuclear structure of ^{17}Ne, such as its single-particle ground-state configuration in terms of s^2- and d^2-content, and the spatial correlations between the two protons.

- One-proton-removal reactions from ^{17}Ne. The cross section of the process and the momentum distribution of the residual final-state ^{16}F fragment, in combination with a suitable reaction model, may be taken to extract spectroscopic information about the removed protons, such as their angular momentum state. The ^{17}Ne s^2/d^2 configuration mixture can be determined in this way.

- Quasi-free (p,2p) scattering reactions from ^{17}Ne. The same observables are accessible using such reactions as in the case of knockout on carbon. By having employed new detection components at the R^{3}B/LAND setup, additionally the two recoil protons are detected, allowing for an exclusive identification of the reaction channel. The momenta of the two recoil protons bear the same information about the de-populated state in ^{17}Ne, so that a redundant measurement is possible. Furthermore, the spectroscopy not only of near-surface nucleons, but also of central and deeply bound ones promises to be feasible.

The first item mentioned, Coulomb dissociation of ^{17}Ne using a lead target, will not be subject of this work. Instead, the present work focusses on the direct nuclear-reaction types mentioned in the second and third item: Peripheral one-proton removal on a carbon target, and quasi-free scattering on a polyethylene target. The thesis at hand is organised in the following manner: After these introductory remarks, chapter 2.2 gives a brief overview of theoretical concepts for the description of halo nuclei, and for experimental techniques suited to study them. Following up in chapter 3 is a presentation of the experimental setup used for the present studies. Calibration, reconstruction and analysis procedures for the obtained data are then outlined in chapter 4 and chapter 5. The results and findings are shown and discussed in chapter 6, before coming to a conclusion and an outlook in the final chapter 7.

[5] GSI Helmholtzzentrum für Schwerionenforschung GmbH, Darmstadt, Germany.

2

Light Exotic Nuclei

It is a difficult task to describe nuclei, the cores of atoms. There is no closed theoretical description yet that would in a satisfying way be able to reproduce all the properties of all bound nuclei known today[1]. Properties of nuclei are quantities such as binding energies, energy levels of excited states, total spin and parity of such states, magnetic moments, but also sizes, interaction cross sections and general reaction properties.
Since the discovery of the existence of nuclei by the famous experiment of α-scattering on a gold-foil by Rutherford and his co-workers, various models for atomic nuclei have been designed, which work differently well for the description of specific properties of nuclei, or in different mass regions of nuclei. The liquid-drop model, for example, is relatively well suited to describe the radii of heavy nuclei. The most commonly employed model, however, is the so-called shell model and modern variations of it. The shell model, which was initially developed by Goeppert-Mayer and Jensen [1, 2], started to describe nuclei as being composed of protons and neutrons, treated as quantum-mechanical fermions that obey the Pauli's exclusion principle and occupy individual orbits characterised by a main quantum number, an orbital-angular-momentum number and a spin number leading to a total angular momentum — in close analogy to the organisation of the electron-shells of an atom — being confined by a common central potential created by the respective nucleon-nucleon two-body interactions.
Exotic nuclei, which are situated at the limits of nuclear existence, the driplines, provide an ideal testing ground for the understanding of nuclear structure.

2.1 Halo Nuclei

The research field of halo nuclei was 'born' in the time between 1985 to 1987, and although being 'grown-up' nowadays to an age of more than 20 years, it still is exciting and actively driven, drawing the attention of experimentalists and theorists. In 1985, Tanihata and his co-workers [21] measured interaction cross sections of various stable and neutron-rich He and Li isotopes, finding extraordinarily large values, *e.g.*, for ^{11}Li. Although in earlier years starting from the 1960s a few experimental indications for light and neutron-rich nuclides such as ^{11}Be had pointed towards new physics at the dripline(s) [22], it took until those systematic investigations of Tanihata and the subsequent explanations and interpretations of Hansen and Jonson in 1987 [23] to formulate the concept of 'halo' nuclei. Halo nuclei are systems of a compact and inert core which is surrounded by one or two loosely bound valence nucleons being present at a large average distance from the core; that leads to a large rms matter radius of the total nucleus and correspondingly to large interaction cross sections, such as those measured by Tanihata.
From the specific case of ^{11}Li, which as we call it today is a Borromean (see chapter 1 for an explanation) two-neutron-halo nucleus, Hansen and Jonson concluded that the pairing

[1] Not even to speak of countless unbound nuclear systems beyond the driplines.

of the two valence neutrons causes an additional source of binding in the presence of the ^{9}Li core, although by themselves they do not form bound states. Figure 2.1 presents the size and structure of the unstable ^{11}Li in comparison to two well-studied stable nuclei, ^{208}Pb and ^{48}Ca. The matter radius of ^{11}Li's core, ^{9}Li, is 2.3 fm, and the rms distance between

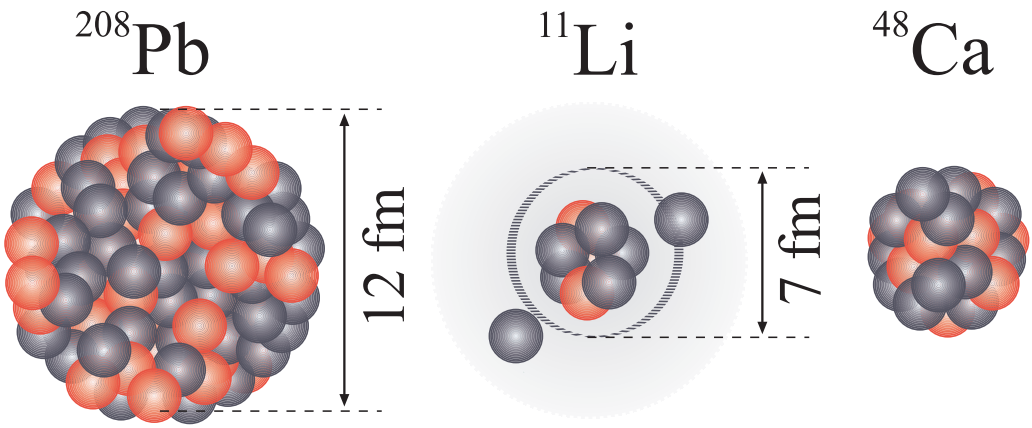

Figure 2.1: Comparison of nuclear sizes and structuring at the examples of the stable nuclei ^{208}Pb and ^{48}Ca, and the unstable two-neutron-halo nucleus ^{11}Li. The radial extent of the two halo nucleons of ^{11}Li reaches as far as the size of ^{208}Pb of 12 fm. ^{11}Li's rms matter radius of 3.5 fm is the same as the one of ^{48}Ca. The figure has been adopted from [22].

the core and the valence di-neutron is 9 fm, which is comparable to the rms radius of the much heavier ^{208}Pb. ^{11}Li's total rms matter radius amounts to 3.5 fm (see also [24]), which is the same as the one of the doubly-magic intermediate-mass nucleus ^{48}Ca.
As a result of intensive theoretical work and numerous experimental studies (most of them reaction studies using swift beams of exotic isotopes, see chapter 2.2), as of today a good handful of three-body-halo nuclei are known (^{6}He, ^{8}He, ^{11}Li, ^{12}Be, ^{14}Be, ^{15}B, ^{17}B, ^{19}B, ^{20}C, ^{22}C, ^{17}Ne)[2], as well as also a considerable number of two-body-halo nuclei (^{8}B, ^{11}Be, ^{15}C, ^{19}C, ^{23}O); recall figure 1.1 in the previous chapter for an overview of the light region of the nuclear chart.
In the following two paragraphs, the basic concepts for the description of halo nuclei, conditions and limiting factors for their existence as well, will be outlined. The given information therein (and up to this point) has been obtained from the in-depth reviews by Jonson [22], Al-Khalili [24], and Riisager [25]. For greater detail on the topic of nuclear halos, the reader is referred to those, as well as to the review by Jensen [26].

Two-body Halos A nuclear two-body halo (consisting of a core plus a 'satellite'-nucleon) may form, as a rule of thumb, if the valence nucleon is bound 'weakly enough' to the core, *i.e.*, if its separation energy S_n is low enough. That has been observed to happen preferably when approaching the (neutron) driplines of light nuclei, where due to the large isospin asymmetry the binding energy of nuclear systems in general decreases, and on the other hand due to the small number of nucleons in a nucleus the significance of clustering

[2]The nuclei ^{12}Be, ^{15}B, and ^{20}C are not Borromean. ^{8}He and ^{14}Be also show significant indications of four-neutron-halo properties. ^{17}Ne, defining the topic of this thesis, is a Borromean system, but was not yet found to show a very pronounced two-proton halo.

is enhanced. In a sense, halo formation is a "threshold effect" [24], as depending on the separation energy the valence nucleon's wave function may tunnel further or less far outside the classical radial limits of the confining potential, and thus may show a larger or smaller (spatial) decoupling from the core.
As an approximation, the in principle complex many-body nuclear wave function of a two-body halo, Φ_A, may be written as a product of the core's ($\phi_{core}(\xi)$) and the valence's ($\psi(\vec{r})$) wave function:

$$\Phi_A \approx \phi_{core}(\xi)\psi(\vec{r}). \tag{2.1}$$

Far from the origin of the potential the wave function has a Yukawa shape:

$$\psi(r) = N\frac{e^{-\kappa r}}{\kappa r}. \tag{2.2}$$

Therefore, κ, the asymptotic parameter for the decay of the wave function outside the well, depends only on the separation energy of the nucleon S_n and the reduced mass of the core-nucleon system μ:

$$\kappa = \frac{\sqrt{2\mu S_n}}{\hbar}. \tag{2.3}$$

For halo nuclei the mean of the squared radius, $\langle r^2 \rangle$, is dominated by the tail of the wave function outside the potential range. It scales inversely proportional with the nucleon's separation energy, S_n:

$$\langle r^2 \rangle = \frac{\hbar^2}{4\mu S_n}. \tag{2.4}$$

It has to be noted, however, that this radial divergence with the separation energy is only true for the lowest valence-nucleon-orbital-momentum states of $l = 0, 1$. This is owed to the fact that — similar to classical celestial mechanics — the radial part of binding potential has a component that depends on the orbital angular momentum. For the corresponding quantum-mechanical central nuclear potential that orbital component scales with $l(l+1)$, *i.e.*, it grows quadratically with the orbital angular quantum number of the respective valence nucleon. For the ground-state of the famous one-neutron halo nucleus of ^{11}Be, for example, the major contribution ($\approx$60 %) to the halo-neutron wave function was determined to be from the $1s_{1/2}$ orbital [27].

Three-body Halos The description of two-nucleon halos is naturally more complex, but it follows similar trends. Usually, such three-body systems are formulated using so-called Jacobi coordinates, $(\vec{x}, \vec{y})$, as for example formulated in [28]. Here, $\vec{x}$ stands for the relative-position vector between the two nucleons, and $\vec{y}$ is the relative vector between core and the centre of gravity of the two nucleons, so that the total nuclear wave function, Φ_A, can be approximated as:

$$\Phi_A \approx \phi_{core}(\xi)\psi(\vec{x}, \vec{y}). \tag{2.5}$$

The relative wave function ψ is a solution of a three-body Schrödinger equation. This 6D-equation can be reduced to a radial equation using hyperspherical coordinates (ρ, α,

ϑ_x, φ_x, ϑ_y, φ_y), where $\rho = x^2 + y^2$ is the hyperradius, and $\alpha = \tan^{-1} x/y$ the hyperangle. Outside the range of the potential, the radial equation has the form

$$\left(-\frac{d^2}{d\rho^2} + \frac{(K+3/2)(K+5/2)}{\rho^2} - \frac{2mE}{\hbar^2}\right)\chi(\rho) \quad = \quad 0. \tag{2.6}$$

Here, K denotes the hypermomentum, the three-body equivalent of the orbital-angular-momentum number. It is constructed as $K = l_x + l_y + 2n$, $n = (0, 1, 2, ...)$ being the main quantum number, and $l_{x,y}$ the angular momentum numbers for the x and y two-body systems. As already apparent in equation 2.6, the corresponding generalised centrifugal barrier in three-body halos depends on the hypermomentum K as $V_c \sim (K + 3/2)(K + 5/2)/\rho^2$. That means, in contrast to two-body systems, that the centrifugal barrier in three-body systems is always greater than zero, even for the lowest hyperangular momentum waves at $K = 0$ that have an 'effective l' of $3/2$. That additional confinement in three-body systems, however, is compensated by the in total higher degree of freedom so that these systems still turn out to be comparatively large [25]. In effect, the external part of the radial wave function is described by a generalised Yukawa shape,

$$\chi(\rho) \quad \sim \quad \frac{e^{-\kappa\rho}}{\rho^{5/2}}. \tag{2.7}$$

Here, the asymptotic parameter $\kappa = \sqrt{2mS_{2n}}/\hbar$ is linked to the two-nucleon (two-neutron) separation energy S_{2n} and the nucleon mass m.

Proton Halos It seems trivial that one should not expect them to form as easily as neutron halos. Due to the additionally confining Coulomb potential well, valence protons cannot tunnel that far into classically forbidden regions at large radii. Or from another perspective, if they were located at large radii corresponding to those of neutron-halo nuclei, they would not be bound anymore due to the Coulomb repulsion opposite to the attractive nuclear force. Clear cases of one-proton-halo nuclei are known to be the ground state of ^{8}B, and the first excited state of ^{17}F. The best candidate nucleus to show a two-proton halo, ^{17}Ne, has been discussed in chapter 1.

The following sections will give an overview of types of nuclear reactions that are suited to study the structure of exotic and in particular halo nuclei. It focuses on the ones that have been employed for the presented experimental work, knockout reactions and quasi-free scattering in inverse kinematics.

2.2 Direct Nuclear Reactions for Nuclear Spectroscopy

The commonly used shell model regards nuclei as being composed of independent fermions: Neutrons and protons are filling up ordered shells — characterised by harmonic-oscillator-based main, orbital-, and spin-angular-momentum quantum numbers. Therefore, they occupy different quantum states each, a concept already briefly sketched in chapter 1. The according scheme of energy levels established for stable nuclei is shown in figure 2.2. In the shell-model approach, nuclei are 'constructed' by subsequently filling nucleons (neutrons or

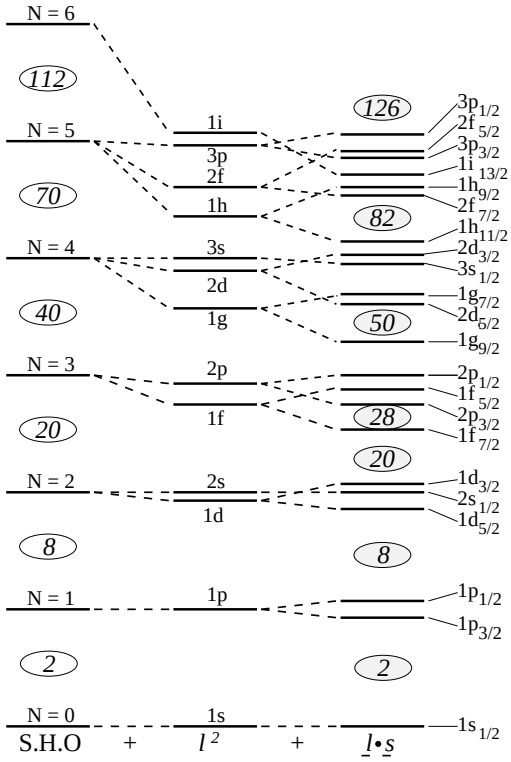

Figure 2.2: Structure of energy levels in a quantum-mechanical shell model. Starting from the levels in a spherical harmonic oscillator (left column), the inclusion of orbital angular momentum leads to a level splitting (middle), and a further 'fine'-splitting results from the addition of spin-orbit coupling (right). The ovals indicate the 'magic' numbers of neutrons or protons needed to fill up levels which are energetically at a large distance to the next one, *i.e.*, represent a particularly stable configuration. The scheme has been established based on the experimental evidence for stable nuclei. The figure has been taken from [29].

protons) into the level scheme shown in figure 2.2, in energy-ascending order. The energy level of the last filled nucleon then represents the Fermi energy, below which all levels are filled, and above which all are empty at zero temperature. There are several aspects of interest in studying the validity and the limits of this picture.

Single-particle Structure and "Quenching" One topic of great contemporary interest is, *e.g.*, the single-particle occupancy or "quenching factors" observable in stable and unstable nuclei. (This topic is covered up to a greater extent in [29] and [30]). *Via* various types of reaction experiments, the probability to observe a nucleon in a certain shell-model quantum state may be probed. This is usually done by constructing the ratio, R_S, of the experimentally determined single-particle cross section, σ_{exp}, to the one being obtained using a corresponding shell-model based, σ_{theo}. It has turned out, that for most stable nuclei such quenching factors, or occupancies, reach values up to $\sim$70 %, only. This is to say, that theoretical calculations over-predict the observable one-nucleon removal cross sections, or in other words, that the nucleons being probed by a reaction are described by (superpositions

of) pure shell-model states only up to a limited amount. A second dimension of this feature is being provided by the observation, that the degree of this reduction of (observable) occupancy seems to be dependent on the difference in proton and neutron separation energy in the nuclei being probed. As an example (see figure 2.3 of [29]), the occupancy for neutrons in neutron-rich nuclei (*e.g.* ^{15}C) is hardly reduced (R_S close to 100 %), whereas the occupancy for neutrons in proton-rich nuclei (*e.g.* ^{32}Ar) is strongly reduced (R_S only about 25 %). No finally conclusive explanations for these phenomena have been established yet, although so-called nucleon-nucleon (in particular, neutron-proton) short-range correlations are at the focus of discussion. It is evident, though, that reactions to probe single-particle levels in exotic nuclei with to their large span of isospin asymmetry will play a major role for this topic.

Shell Structure at the Driplines When approaching the nuclear driplines, the binding energies become smaller and the matter distributions become less compact, so that the spin-orbit coupling becomes less and less significant. The energy gaps between shells may change up to such an extent that the established magic numbers (2,8,20,...) disappear and new ones form, such as observed, for example, for the dripline nucleus ^{24}O [3], which exhibits a magic number of 16 neutrons representing a comparatively large gap between the filled-up $1s_{1/2}$ and the empty $0d_{3/2}$ shells ($2s_{1/2}$ and $1d_{3/2}$ in the notation of figure 2.2). Changes in shell gaps may go as far as that even the 'original' ordering of the levels is affected. This phenomenon, for example, has been expected to occur for ^{17}Ne [16], the nucleus studied within this thesis.

In order to perform research on topics such as the two just sketched above by the use of "direct nuclear reactions", they need to allow for an experimental sensitivity on the nuclear level that is (de-)populated during them. In simpler words, one must be able to distinguish reactions involving one or the other single-particle state, say *via* its binding energy and/or its orbital-angular-momentum value that (somehow) need to (clearly) reflect in the experimental observables.
To make a long story short, there are three types of direct nuclear reactions which offer that sort of sensitivity and which have been used to good success in the past:

- Transfer reactions
- One-nucleon removal reactions (inelastic scattering and knockout)
- Quasi-free scattering reactions

There will be no talk about *transfer reactions* here (one may find a short overview and some references in the review of Hansen and Tostevin [30]). Instead, the following two sub-chapters will concentrate on the methods employed for the present experimental work: *one-nucleon removal*, and *quasi-free scattering*. For both types, the present topic of proton-removal from the exotic nucleus ^{17}Ne in inverse kinematics will be employed for showcase illustrations.

2.2.1 One-Nucleon-Removal Reactions on Light Nuclear Targets

For more than ten years, one-nucleon-removal reactions (in particular: knockout reactions) have been used to a great success to study single-particle properties of exotic nuclei [30], and particularly of halo nuclei [22]. Various experimental facilities worldwide (initiated at MSU, but nowadays also used at GSI, RIKEN, GANIL, and others) are using reactions of radioactive beams impinging on light (typically beryllium or carbon) targets, typically at relativistic energies of $\geq$100 AMeV. As will be later outlined to greater detail, in combination with a model of the reaction mechanism, such as the Glauber model, on the one hand single-particle occupancies can be determined *via* the measurement of the corresponding nucleon-removal cross sections, and on the other hand their orbital-angular-momentum state can be extracted from the measured fragment-momentum distribution as well.
The term *one-nucleon removal* implies two contributing reaction types — which can only be distinguished if an exclusive measurement of all final-state particles is possible — namely *inelastic scattering* and actual *one-nucleon knockout*.

Inelastic/Diffractive Scattering Figure 2.3 visualises the process of an inelastic excitation *via* the present example of ^{17}Ne. The transit of the carbon nucleus at non-overlapping

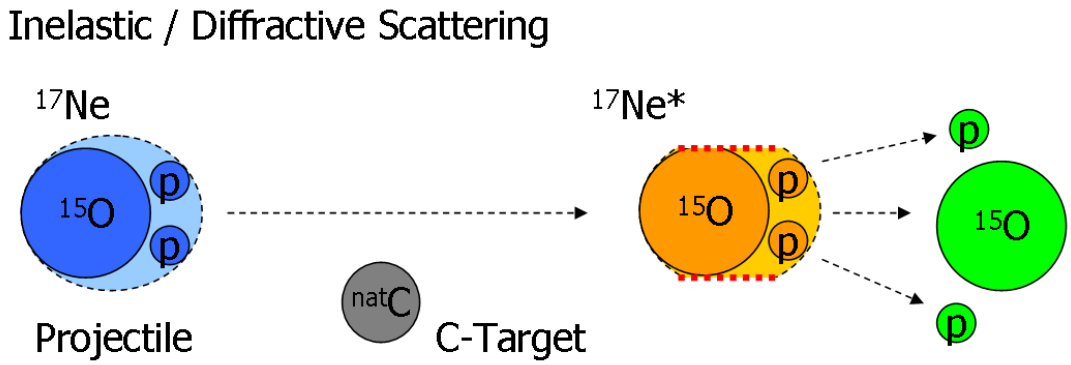

Figure 2.3: Scheme of an inelastic-excitation reaction of a ^{17}Ne projectile on a carbon target in inverse kinematics. The presence of the carbon target leads to a disturbance in the ^{17}Ne wave function — visualised by the red dashed line — which may be understood similarly to optical Fraunhofer scattering. In consequence, the excitation leads to a dissociation of ^{17}Ne into a ^{15}O fragment and two protons, all focussed in forward direction due to the high beam velocity.

distance induces a distortion in the ^{17}Ne projectile wave function, which represents an excitation that in turn leads to the dissociation into ^{15}O+p+p (as ^{16}F is proton-unbound), all projectile-like, *i.e.*, forward-focused. This type of inelastic excitation can be described in a way similar as 'black-disc' or 'Fraunhofer' diffraction known from optics [31, 32]. If efficiency and acceptance of the experimental setup permit, all (three) final-state particles are detected, which allows for a unique identification of this channel[3].

[3]In fact, the channel of electromagnetic (Coulomb) dissociation would have a similar experimental signature. One of the reasons to use a light (low-Z) target such as carbon is to be able to neglect the contribution

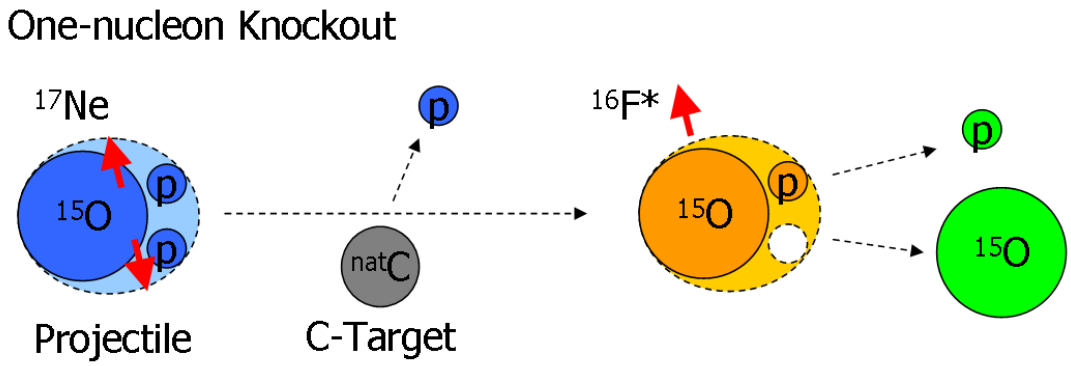

Figure 2.4: Scheme of a one-proton knockout reaction of a ^{17}Ne projectile on a carbon target in inverse kinematics. In peripheral transit, the overlap between the wave functions of the carbon target and a proton of the ^{17}Ne projectile induces a large momentum transfer to that proton. It is 'knocked out', whereas the residual ^{16}F fragment, dissociating into ^{15}O+p, remains as a spectator. Due to momentum conservation, the intrinsic momentum of the knocked-out proton is reflected one-to-one in the recoil of the ^{16}F fragment (both indicated by red arrows).

One-nucleon Knockout Figure 2.4 presents a knockout-reaction scheme at the example of one-proton knockout from ^{17}Ne. At sufficiently (but not too) small impact parameters, the target's and the wave function of a nucleon in the mass-A projectile overlap, leading to a large momentum transfer to the nucleon, knocking it out, while the remaining $A-1$ fragment remains as an unaffected spectator. Seen in the rest frame of the projectile, the residual fragment carries the knocked-out nucleon's momentum as a recoil in opposite direction, visualised by red arrows in figure 2.4:

$$\vec{p}_{\text{nucleon}} \quad = \quad -\vec{p}_{\text{fragment}}. \tag{2.8}$$

The momentum distribution of the recoiling fragments in such reactions reflects the orbital quantum state (mixture) of the knockout nucleon in its shape and width. Halo nuclei, as they host nucleons roaming within a relatively large space, show very narrow momentum distributions of the (core) fragments after halo-nucleon knockout, as a consequence of the Heisenberg uncertainty principle. In the present experiment, the ^{16}F fragment momentum distribution is measured *via* the ^{15}O+p final-state channel (see chapter 6.4.3).
The ground-state configuration of many famous exotic/halo nuclei has been determined in measurements of the fragment momentum distributions in knockout reactions, as for example ^{11}Be [27, 33], ^{8}B [34], or ^{19}C. The theoretical framework used to interpret the experimental data obtained in such reaction experiments will be sketched in the following paragraph.

Theoretical Description One-nucleon-removal reactions in inverse kinematics are often handled by the Glauber approach [35] which is based on two founding pillars [29], in order to justify that the $A-1$ fragment may be treated as a spectator:

by Coulomb excitation.

- The sudden approximation, and
- the eikonal approximation.

The sudden (or adiabatic) approximation consists of the assumption that the reaction happens 'quickly' enough, so that the nucleons inside the (projectile) nucleus do not move during their interaction time with the target. The eikonal approximation means that the projectile moves on a straight line. This is typically formulated as two conditions:

1. The wavelength, λ, of the projectile should be a lot shorter than the target potential range, α. That means that $\alpha/\lambda \gg 1$.
2. The energy of the scattered particle, E', should be much higher than the potential depth, V_0, *i.e.*, $E' \gg V_0$.

It seems well justified, that those approximations are valid within the described experimental scenario of one-nucleon-removal reactions in inverse kinematics at high beam energies of $\beta \geq 0.5$.
Based on these requirements, a theoretical framework may be constructed, allowing for both, the calculation of cross sections corresponding to the removal of nucleons from a given single-particle quantum state, as well as of the (parallel or transversal) momentum distributions of the corresponding residual fragments. Single-particle cross sections have contributions from knockout ($\sigma_{\mathrm{knockout}}$), diffraction ($\sigma_{\mathrm{diffraction}}$), and Coulomb dissociation ($\sigma_{\mathrm{Coulomb}}$). The latter one is usually neglected for light targets like carbon or beryllium [30]:

$$\sigma_{\mathrm{single-particle}} = \sigma_{\mathrm{knockout}} + \sigma_{\mathrm{diffraction}}. \tag{2.9}$$

The contribution by knockout reactions to the single-particle cross section is written as an integral over all impact parameters, $\vec{b}$ [30]:

$$\sigma_{\mathrm{knockout}} = \frac{1}{2j+1} \int d\vec{b} \sum_m \langle \psi_{j,m} \mid (1-|\mathcal{S}_n|^2)|\mathcal{S}_c|^2 \mid \psi_{j,m} \rangle. \tag{2.10}$$

Here, the $\psi_{j,m}$ describe the two-body-eigenstate wave functions of the relative nucleon-fragment motion. $\mathcal{S}_n$ and $\mathcal{S}_c$ are the elastic-scattering S-matrices, also called profile functions. The given product represents the transition operator that guarantees target-nucleon but not target-core overlap. In other words, only a limited range of very surface-concentrated impact parameters, that lead to nucleon-knockout but core-survival, are selected.
The contribution by diffractive/inelastic breakup is formulated in [30] as:

$$\sigma_{\mathrm{diffr.}} = \frac{1}{2j+1} \int d\vec{b} \sum_{m,m'} \left[\langle \psi_{j,m'} \mid |1-\mathcal{S}_c\mathcal{S}_n|^2 \mid \psi_{j,m} \rangle \delta_{mm'} - |\langle \psi_{j,m'} \mid (1-\mathcal{S}_c\mathcal{S}_n) \mid \psi_{j,m} \rangle|^2 \right]. \tag{2.11}$$

Various computer codes for these types of calculations exist; the ones of Aumann [36] and Bertulani [37, 38] have been used for the interpretation of some of the presented data in chapter 6.4. The following and last section of this chapter will introduce the reactions of quasi-free scattering.

2.2.2 Quasi-Free-Scattering Reactions on Protons

Quasi-free scattering (QFS) is a term used to describe scattering processes of a basic and simple projectile — usually an electron or a proton — on a well-defined substructure (or: cluster) inside a nucleus. This could be a single nucleon, but also a deuteron, triton, or in principle any other sub-nucleus. Fundamental though is, that the rest of the involved nucleus is not involved in the scattering process, *i.e.*, is not transferred any momentum, and ideally also not involved in any initial or final state interaction. The rest of the nucleus is acting as a spectator, and the actual scattering of the projectile on the cluster in the nucleus happens as if that one was free, *ergo* the term quasi-free[4].
Such reactions have been used for the second half of the 20th century in direct kinematics, in order to study the single-particle and cluster-structure of stable nuclei, by employing electron- or proton-beams in order to induce (e,e'p) or (p,2p) reactions. Theoretical pioneers of QFS at that time, Jacob and Maris [39,40], have shaped a classic 'definition' that is worth repeating:

> ... Qualitatively speaking, by quasi-free scattering a process is meant in which a high energy (100-1000 MeV) particle knocks a nucleon out of a nucleus and no further violent interaction occurs between the nucleus and the incident or the two outgoing particles ...

For the sake and purpose of the present thesis, it will limit and specialise the discussion to the case of (p,2p) scattering in inverse kinematics. Following the example of a ^{17}Ne beam, an overview of the involved particles is offered in figure 2.5.

The kinematical relations for the laboratory frame, derived from energy-momentum conservation, are summarised here:

$$\vec{q} = \vec{p}_A - \vec{p}_{A-1} = \vec{p}_1 + \vec{p}_2, \tag{2.12}$$

$$E_A + m_0c^2 = E_{A-1} + E_1 + E_2. \tag{2.13}$$

The intrinsic momentum of the knocked-out proton, $\vec{q}$, is redundantly equal to the difference of the momenta of projectile and fragment, $\vec{p}_A - \vec{p}_{A-1}$[5], as well as in the sum of the momenta of the two recoil protons, $\vec{p}_1 + \vec{p}_2$.

Furthermore, it is evident in the non-relativistic formulation of equation 2.14, that one can precisely tag the specific proton-knockout channel:

$$S_p = E^* - Q = E^* + T_A - (T_1 + T_2 + T_{A-1}). \tag{2.14}$$

Here, S_p denotes the proton's separation energy, which is as usual defined as the difference of the residual fragment's (^{16}F) excitation energy, E^*, and the reaction's Q-value. That one, in turn, can be expressed in terms of the participants' kinetic energies. All those quantities may be measured exclusively. It becomes apparent, that for the study of beams

[4] Of course, the scattering process will necessarily be influenced by the binding energy of the cluster in the nucleus, leading to different kinematics than in truly free conditions.

[5] This is true both for the longitudinal and transverse component. By construction, the transverse momentum of the projectile is zero, so that $\vec{q}^{\perp} = -\vec{p}^{\perp}_{A-1}$.

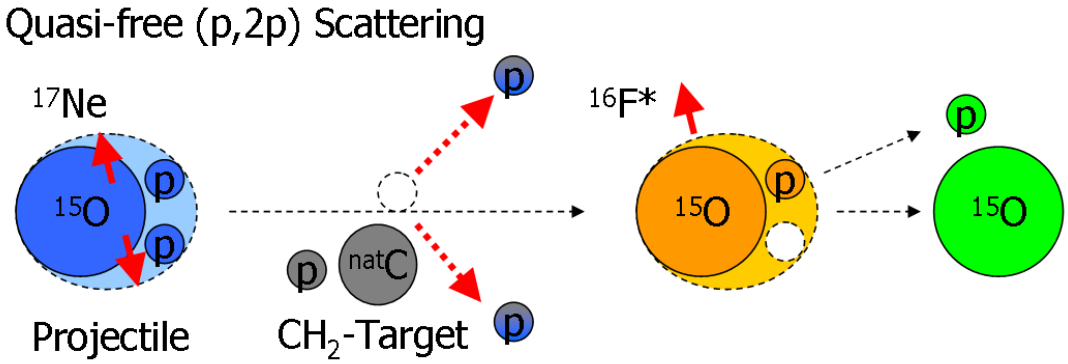

(a) Overview.

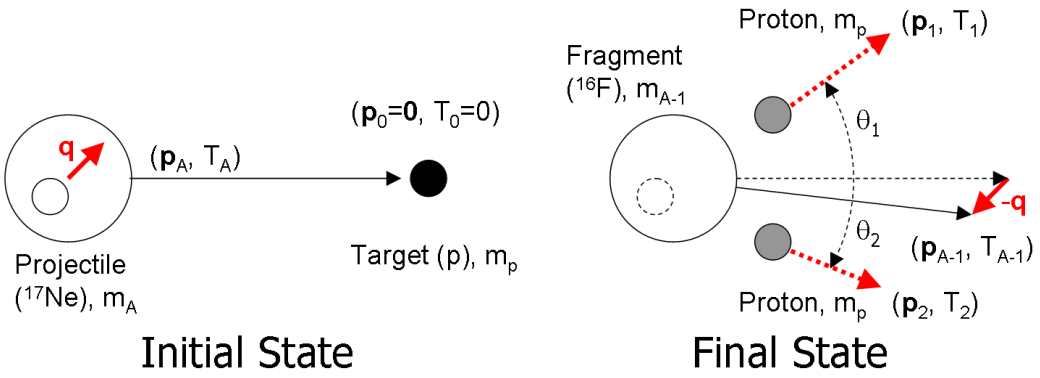

(b) Terminology.

Figure 2.5: Schematic overview (a) and used terminology (b) for quasi-free (p,2p) scattering reactions of ^{17}Ne on a proton-rich CH_2 target in inverse kinematics, as seen in the lab. A proton of the projectile (^{17}Ne, index A) scatters on a target proton (index 0), so that both of them (indices 1, 2) recoil to large laboratory angles. Identical to the knockout case (figure 2.4), the intrinsic momentum of the removed proton ($\vec{q}$, full red arrows) is translated into an opposite recoil of the fragment (^{16}F, $A-1$). Additionally, that proton momentum also is reflected in the two recoil protons (dashed red arrows), which thus allows for a redundant measurement.

of exotic nuclei using reactions in inverse kinematics, QFS has the potential to be even more selective than one-nucleon-removal reactions due to the observation of more final-state products. Additionally, it is realistic to expect that *e.g.* (p,2p) reactions will not only be surface-localised like knockout reactions. As has been the case in numerous normal-kinematics experiments, QFS promises to be able to 'easily' probe deeply bound nucleons in the inner regions of exotic nuclei, which have to be studied using a secondary-beam experiments in inverse kinematics.

The now following chapter 3 will outline the experimental facilities and setup used for the presented work.

3

Experimental Setup

In August 2007, the S318 experiment was performed at the R^{3}B/LAND setup located in Cave C, at GSI. Exotic beams of ^{17}Ne at an energy of approximately 500 AMeV and an average ion rate of $10^4\,s^{-1}$ were employed. The goal of this experiment was the kinematically complete measurement of various types of breakup reactions of ^{17}Ne with various targets, in inverse kinematics:

- Pb(^{17}Ne,^{15}O+2p+X); electromagnetic dissociation on a ^{nat}Pb target,
- C(^{17}Ne,^{15}O+p+X); nuclear one-proton removal on a ^{nat}C target,
- p(^{17}Ne,^{15}O+p+2p); quasi-free scattering on a proton in a CH_2 target.

The work presented here focuses on the latter two reactions. Accordingly, this chapter will give an overview of the employed experimental facilities with a focus on the detection components that are important for those reaction channels. After very briefly introducing the GSI accelerator infrastructure together with the crucial FRagment Separator (FRS) needed to produce and transport beams of short-lived isotopes, the employed R^{3}B/LAND reaction setup in Cave C will be presented in more detail.

3.1 The GSI Heavy-Ion Laboratory

GSI is a heavy-ion-beam facility located north of Darmstadt, Germany, that can produce all sorts of stable-isotope ion beams (primary beams), from ^{1}H to ^{238}U, with maximum beam energies up to 4.5 GeV for hydrogen, 2 GeV for neon, or 1 GeV for uranium. GSI (shown schematically in figure 3.1) consists of two main accelerator components. The UNIversal Linear ACcelerator (UNILAC, see [41]) with a maximum beam energy of 11.4 AMeV can be parallelly fed by either of three different ion injectors, and can be used for low-energy experiments in stand-alone operation (for details, see [41]). Alternatively, it can be used as an injector for the Schwer-Ionen-Synchrotron (Heavy-Ion-Synchrotron, SIS) which can reach the final beam energies mentioned above. (See, *e.g.*, [42] for more documentation). The high-energy primary beams produced by the SIS may be used directly for various forms of experimental research and also for the medical purpose of cancer treatment *via* the irradiation of certain types of tumours. Furthermore, as has been the case for the present work, they can be used to produce secondary beams of radioactive isotopes, using the Fragment Separator.

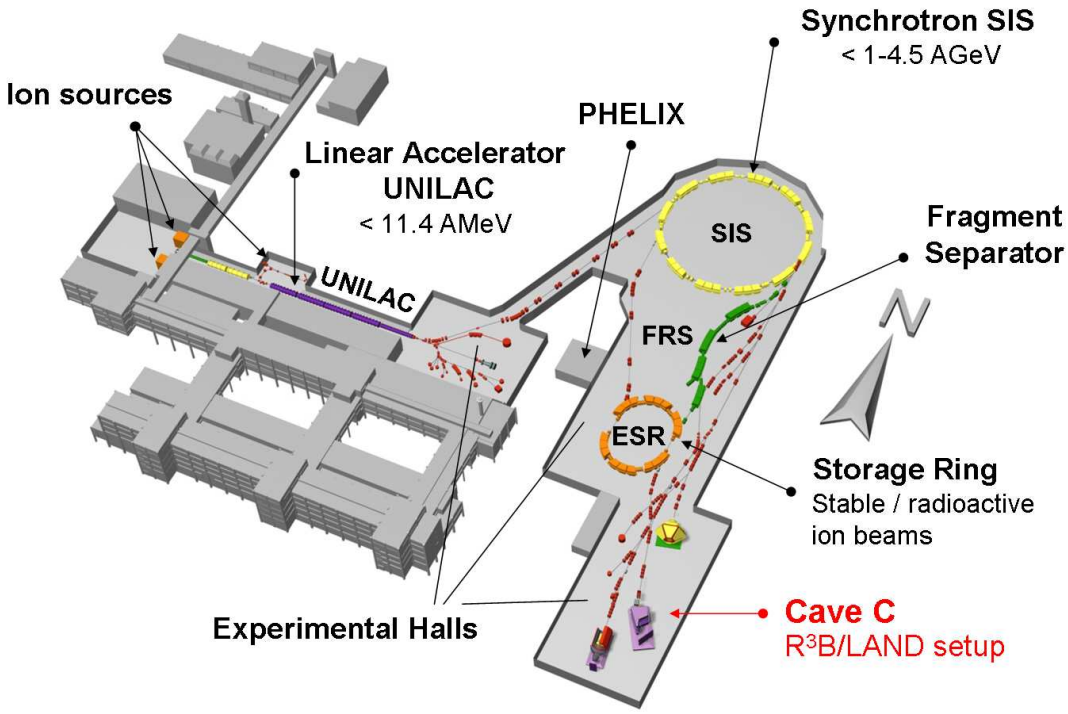

Figure 3.1: Sketch of facilities presently at GSI. Heavy-ion beams (of any stable isotope) are created using ion sources coupled to the linear accelerator UNILAC, which is used for various low-energy experiments with up to around 11 AMeV beams. Alternatively, the UNILAC serves as an injector for the heavy-ion synchrotron SIS, which in turn delivers high-energy beams of up to 1–4.5 AMeV with multiple experimental applications. As an example, the high-power laser system PHELIX may be used in experiments combining heavy-ion beams and laser pulses for probing solid-state and plasma matter and their transitions, both at low- and high-energy setups. With the fragment separator FRS, radioactive ion beams are produced by the separation of fragmentation-reaction products from SIS beams impinging on a thick light production target, typically beryllium or carbon. With the Experimental Storage Ring ESR, beams of stable and unstable isotopes with intensities down to single ions can be stored and cooled for, *e.g.*, high-precision decay studies. In the case of the present experiment, radioactive ^{17}Ne beams were produced using the FRS *via* the fragmentation of primary ^{20}Ne beams on a thick beryllium target, and transported downstream to the R^{3}B/LAND setup in Cave C for studying their breakup reactions at beam energies of around 500 AMeV.

3.1.1 The Fragment Separator FRS

The FRS [43] is a magnetic separator and spectrometer for ion beams. Being in principle suitable for all sorts of beams, it is usually used for the production of exotic ion beams resulting from in-flight-fragmentation reactions. Such exotic beams can be selected and studied either within the FRS (for example, see [3]), usually with a reaction and detection setup at one of its focal planes, or they can be delivered to further experimental setups, as in the present case, to Cave C. The term in-flight fragmentation stands for the following

procedure.
The high-energy primary beams extracted from the SIS are magnetically guided onto a thick but light (low-Z material) target, usually beryllium or carbon. Depending on the velocity and the species of the primary beam, a wide range of isotopes is produced as the result of violent nuclear fragmentation reactions. Those fragments have lower energies, which is, however, still in the same order of magnitude as the primary beam. Out of such a mixed beam one selects the fragments of interest by means of magnetic separation. Figure 3.2 shows the placement of the FRS relative to the rest of the high-energy branch of GSI (top figure, a)), and its main components and focal planes (bottom figure, b)).

(a) Placement of SIS and FRS with surrounding components and the experimental areas Cave B and C, as seen from above. The primary fragmentation target TA is situated at the extraction area of SIS (figure based on [44]). S2 and S8 indicate beam diagnosis stations at selected focal planes along the FRS-to-Cave C beam line providing a time-of-flight measurement relevant for the beam identification at Cave C.

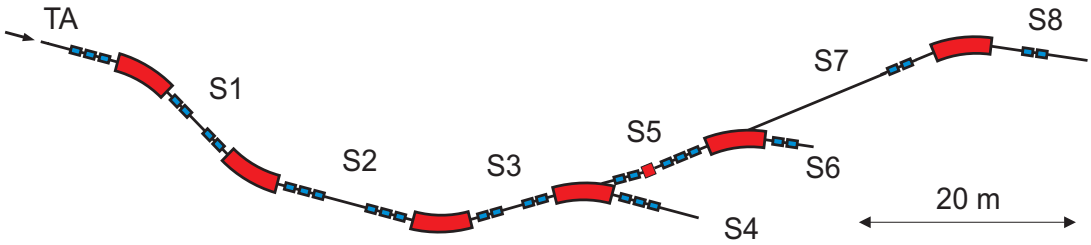

(b) Closer view of the FRS beam line with the primary target area TA and its various focal planes, S1 to S8. Bending dipole magnets are indicated by large shapes, focusing quadrupoles by smaller ones (figure based on [44]).

Figure 3.2: (a) GSI accelerator structures: From the UNILAC injection line *via* SIS, the FRS, to the experiment in Cave C. (b) Detailed view of the FRS.

Adjusting the field strength B of a dipole magnet (of given curvature radius ρ), the FRS can be tuned to transmit only ions within a certain range of their A/Z times $\beta\gamma$:

$$B\rho = \frac{p}{q} \sim \frac{A}{Z}\beta\gamma. \tag{3.1}$$

where ρ is the bending radius of the circular trajectory of an ion in the B-field, p its (relativistic) momentum and q its electrical charge. β is the ion's speed in units of the

speed of light (c), γ the corresponding relativistic factor, and A and Z the ion's mass and charge number, respectively. For a broader and more comprehensive overview of in-flight-fragmentation techniques the reader is referred to, *e.g.*, [45].
For the presented experiment, primary ^{20}Ne beams of about $10^{10}\,\mathrm{s}^{-1}$ at $E = 630\,\mathrm{AMeV}$ were provided by the UNILAC and SIS, and guided onto the primary beryllium production target at TA (see figure 3.2). The FRS beamline was tuned to preferably select and convey secondary beams of ^{17}Ne (at $A/Z = 1.7$), which arrived at the LAND/R^{3}B setup in Cave C with an energy of 500 AMeV and an ion rate of about $10^4\,\mathrm{s}^{-1}$. In the following, the key features of that setup will be outlined.

3.2 The R^{3}B/LAND setup in Cave C

The R^{3}B/LAND setup in Cave C is a nuclear-reaction setup for radioactive as well as stable nuclei at relativistic energies, usually in inverse kinematics. It is designed for the study of nuclear excitation functions using the invariant-mass-reconstruction technique (see chapter 5.3), which is based on the event-by-event and exclusive measurement of all initial and final state particles, *i.e.*, in complete kinematics.
Designed in the early 1990s in the Cave B experimental area at GSI as the ALADIN-LAND setup — triggered by the construction of the corresponding LAND[1] detector [46] used in combination with the ALADIN[2] magnet (see description in [47]) — it has continuously been upgraded ever since and was used for many experiments with short-lived nuclei, as summarised in [48].
In 2004, this very modular setup was moved to its current location in Cave C; since then, significant upgrades to the detection systems have been made: On the one hand, to measure the excitation of proton-rich (unstable) nuclei; on the other hand, to be able to study quasi-free (p,px) knockout reactions in inverse kinematics, *via* the detection of the light recoil particles[3] at large angles. For example, an upgrade for the Crystal Ball was performed within the framework of this thesis. The setup's status, its components and layout as present for the S318 experiment in August 2007 are sketched in figure 3.3 and described in the following parts of this chapter.

3.2.1 In Front of the Target

The purpose of the detectors in front of the target is the determination of the initial state of a nuclear reaction for each single nucleus, *i.e.*, event-by-event. This means the identification (ID) of each isotope (A, Z), and its four-momentum vector $P_\mu = (E/c, \vec{p})$.
Referring to figure 3.3, the ^{17}Ne beam[4] is entering from the left. At the FRS focal planes S2 and S8 (see figure 3.2) beam diagnostics stations are installed, hosting a paddle-like plastic-scintillator detector each, for simplicity called S2 and S8, with dimensions of

[1] Large Area Neutron Detector.
[2] A LArge DIpole magNet.
[3] Within this thesis: the two protons from (p,2p) reactions.
[4] Although the FRS was set to accept ^{17}Ne primarily, various isotopes of neighbouring $(A/Z)\beta\gamma$ values remained as contaminants due to the 2 % momentum acceptance of the FRS.

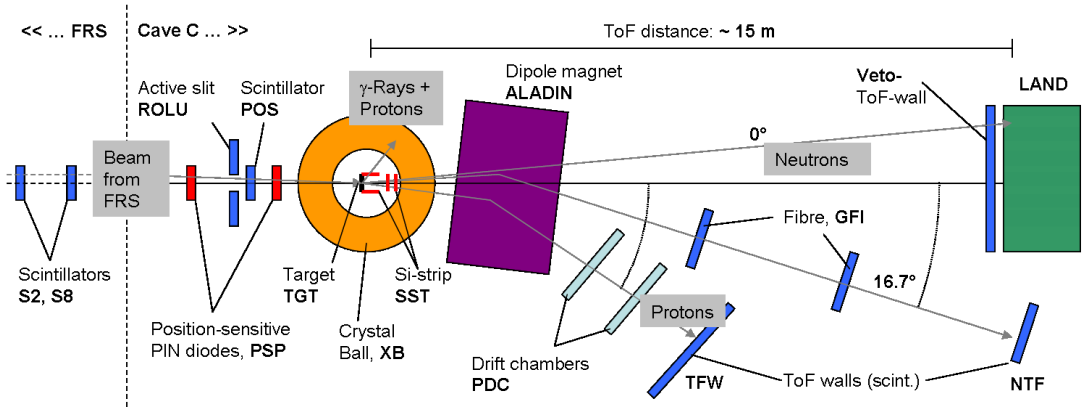

Figure 3.3: Schematic view of the experimental setup in Cave C. The beam enters from the left, is identified and tracked using S2/S8, POS and PSP detectors, before impinging on the target TGT. Gamma rays and recoil protons are detected with a Si-strip detector box (SSTs) and the Crystal Ball (XB). Charged final-state spectator-like fragments are tracked and charge-identified using in-beam SSTs, and bent away from the original beam axis by the magnetic field of the ALADIN magnet. Heavy fragments are tracked using the GFI detectors before reaching the NTF ToF-Wall. Protons, which are bent stronger, are tracked using the PDCs and finally measured with the TFW. Evaporation neutrons can be measured with the 0° LAND neutron detector, but in the case of the proton-rich ^{17}Ne were neglected, and LAND was not in operation.

$21.9\times8.0\times0.1\,\mathrm{cm}^3$ and $20.0\times8.0\times0.1\,\mathrm{cm}^3$, respectively. They measure the beam velocity *via* its time-of-flight[5] (S2 to S8, S8 to CaveC), up until the POS[6] detector, which is located about 2 m before the reaction target (TGT in figure 3.3). POS is a $5\times5\times0.02\,\mathrm{cm}^3$ plastic scintillator that serves as the main trigger and time reference for the setup (see also chapter 3.2.4). S2, S8 and POS's basic working principle (as the one of any scintillator paddle) is sketched and described in figure 1.2 and 1.3 in [49] and the embedding chapter 1.3 therein. POS is preceded closely by a four-piece active-slit scintillator called ROLU[7] that vetos the outer parts of the extended beam, as they might not hit the target; the ROLU window was set to $2.5\times2.5\,\mathrm{cm}^2$ for most of the experiment. Placed about 30 cm before and 90 cm behind POS are the two $4.5\times4.5\times0.03\,\mathrm{cm}^3$-sized PSP1 and PSP2[8]. Figure 3.4 sketches POS (without ROLU) preceded by the first PSP. They measure the beam position *via* a four-corner anode readout on one face, and the beam's energy loss ΔE *via* an integral cathode on their other face. The energy loss is taken for the Z-identification (see chapter 4.2), and the positions are used for tracking (see also chapter 5.2 and 5.2.1.1) the beam onto the reaction target.

[5]Also the position of the beam on the detectors can be determined, providing a more precise determination of the trajectory and thus both of the ToF and the $B\rho$.
[6]POsition-sensitive Scintillator.
[7]In German: Rechts-Oben-Links-Unten (right-up-left-down).
[8]Position-sensitive Si-PIN diodes.

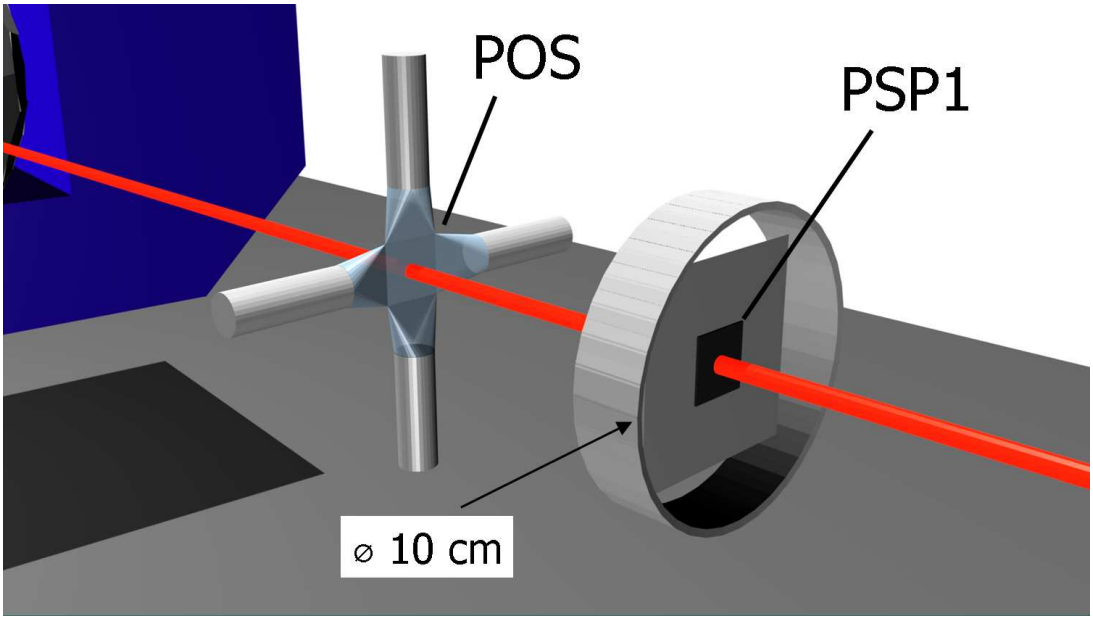

Figure 3.4: 3D sketch of the beam (red, solid line) coming from the right, passing PSP1 (central black square of 2.5×2.5 cm^2) and POS. ROLU is not shown, nor are the Pixel detectors. PSP2 and also the target within the XB are out of view. The blue bulky block on the left indicates the ALADIN magnet. Figure courtesy to [50].

3.2.2 Behind the Target

Behind the reaction target, spectator-like heavy fragments and protons are charge-identified and tracked using two in-beam double-sided Silicon STrip detectors (SSTs) (see chapter 3.2.3.1), placed shortly (9 cm and 13 cm) after the target within the vacuum chamber that surrounds it. The ALADIN magnet separates the outgoing charged particles into a fragment arm centered around 16.7 ° ($A/Z(^{17}\text{Ne}) = 1.7$, $A/Z(^{15}\text{O}) = 1.875$), and a proton arm centered around 31.0 ° ($A/Z(^{1}\text{H}) = 1.008$).

Fragment Arm Heavier fragments (like ^{15}O with $A/Z = 1.875$) are bent about 17 °, and are passing two consecutive GFI[9] scintillating-fibre Detectors. Behind them, their velocity and atomic charge is measured with the NTF[10] ToF-wall made from two crossing (x,y) planes of double-end-readout plastic-scintillator paddles. Figure 3.5 shows artistic pictures of those detectors. The GFIs were placed roughly 3 and 5 m behind the centre of the ALADIN magnet. A GFI consists of 475 vertical 1 mm wide and 50 cm long scintillating fibres that span an active area of about ∼50×50 cm^2. Inside its support frame, each of the fibres is guided to a quadratic mask that is glued onto a photo cathode belonging to a position-sensitive PMT[11]. *Via* such a PMT, the in total 34 (16+18) anode wires forming an (x,y) mesh are read out using QDCs[12]. When a charged particle penetrates the active area

[9] In German: Großer Faser Detektor.
[10] New ToF-Wall.
[11] Photo-Multiplier Tube.
[12] Charge (Q)-to-Digital-Converters.

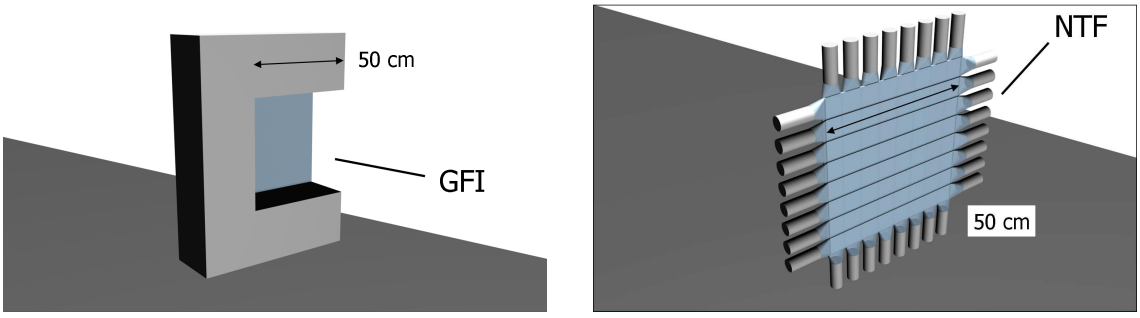

(a) 3D sketch of a GFI scintillating-fibre detector. (b) 3D sketch of the NTF scintillator ToF-wall.

Figure 3.5: Detectors in the fragment arm. (a) GFI: The outer yoke-shaped support frame holds an active area of about $50\times50\,\mathrm{cm}^2$ of in total 475 1 mm wide scintillating fibres. (b) The NTF consists of 8 vertical and 8 horizontal plastic-scintillator paddles of $6\times48\times0.5\,\mathrm{cm}^3$ dimension each, which are read out by PMTs on both ends. Figures courtesy to [50].

of a GFI, the amplitude distribution in the responding anode wires is used to reconstruct the original electron-emitting spot on the cathode, which in turn *via* the mask is identified with one (or more) of the 475 fibres. An x-position resolution of ∼1 mm can be achieved. For in-depth information on the functionality of the GFIs, the reader is referred to [51] and [52].
The NTF was placed about 5.5 m behind ALADIN, that is shortly behind GFI2, and corresponds to a distance of about 8 m to the target. The NTF has an active area of nearly $50\times50\,\mathrm{cm}^2$, it consists of two crossing planes of eight plus eight plastic-scintillator paddles of 6 cm width and 0.5 cm depth each. The NTF can measure the position of hitting fragments (resolution ∼5 cm), their time (depending on ion species, ∼30 ps), and identify their charge Z *via* energy loss ΔE (see also chapter 4.3.1). Furthermore, the NTF provides a trigger (see chapter 3.2.4) for reactions with a final fragment. A more detailed description of the NTF can be found, *e.g.*, in [49] or [53].

Proton Arm Protons have a lower magnetic rigidity ($A/Z = 1.008$) and are bent by approximately 31 °. They pass two gas-filled PDC[13] multi-wire tracking detectors, and after that they are registered in the TFW[14] scintillator paddle time-of-flight wall. See figure 3.6 for an artistic view of the proton arm detectors. The PDCs were placed approximately 2.5 and 3.5 m behind ALADIN. Each has an active area of about $80\times100\,\mathrm{cm}^2$, and consists of two orthogonal planes of gas[15]-floated wires. The PDCs were tilted relative to each other by approximately 30 ° each, in order to be able to identify and discriminate ghost hits. As common for Drift Chambers there are field wires and sense wires, in the PDCs within each (x or y) plane they are arranged in a layer system that leads to a hexagonal structure when viewed from the side. When a proton passes a PDC, within each plane it causes ionisation avalanches towards the nearest sense wires. From the measured time-over-threshold (a quantity proportional to the measured current) on each of the two wires, the exact location

[13] Proton Drift Chamber.
[14] Time-of-Flight Wall.
[15] 80% Argon, 20% CO_2.

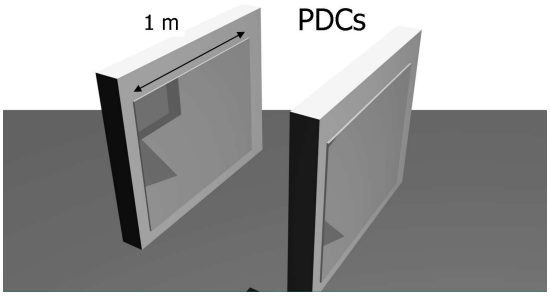

(a) 3D sketch of the PDC multi-wire detectors.

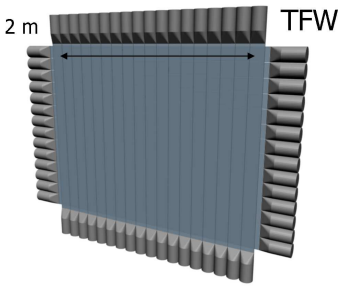

(b) 3D sketch of the TFW scintillator ToF-wall.

Figure 3.6: Detectors in the proton arm. (a) The PDC detectors are have an active area of about $80\times100\,\mathrm{cm}^2$ each. They were tilted relative to each other in order to discriminate against ghost hits. (b) The TFW consists of 18 vertical ($10.4\times154.6\times0.5\,\mathrm{cm}^3$) and 14 horizontal plastic-scintillator paddles of $10.4\times196.6\times0.5\,\mathrm{cm}^3$. Figure courtesy to [50].

of the proton track between them is reconstructed. A spatial resolution of 200 μm can be achieved for protons; a more detailed description of the PDCs is found in [54].
Similar to the fragment arm, a ToF-wall completes the proton arm; the TFW is situated about 8 m behind the ALADIN centre, that means 10.5 m behind the reaction target. Its active area of $80\times100\,\mathrm{cm}^2$ is nearly twelve times larger than that of the NTF, its 18 x plus 14 y paddles have dimensions of $10.4\times154.6\times0.5\,\mathrm{cm}^3$ and $10.4\times196.6\times0.5\,\mathrm{cm}^3$, respectively. The functioning principle is identical to that of the NTF. Its spatial resolution amounts to around 10 cm, the time resolution for protons to about 500 ps, and a charge separation of protons and beam-related background due to energy loss is also possible. Furthermore, the TFW is used to generate a trigger which tags the reactions that have spectator-like protons in the final state.

3.2.3 At and Around the Target

The most basic element of this scattering experiment is the target (TGT) that is used to induce reactions of interest. Various $3\times3\,\mathrm{cm}^2$-sized matter slabs had been mounted on a target wheel in a spherical vacuum chamber. For the various reaction types several targets were used, summarised in table 3.1. Whereas the Pb target was used to induce electromagnetic excitation, the C and CH_2 were used for causing direct nuclear breakup or knockout. Taking data without target (empty target) was necessary to determine the background from the beam reacting with the rest of the setup (detectors, foils, air).
The detection setup around the target for light particles at large laboratory angles, such as knocked-out nucleons from (quasi-free) nuclear scattering, or γ-rays from excited fragments, is shown in figure 3.7. The incoming beam line (blue arrow) with detectors already described earlier (PSP1, ROLU, POS, PSP2) leads into a spherical vacuum chamber of a diameter of 50 cm. At its centre[16], the $3\times3\,\mathrm{cm}^2$-sized targets were mounted on a turnable wheel. Four SSTs for measuring light recoils (protons, alphas) in a box-like array were placed closely

[16]The centre of the chamber co-incides with the Crystal Ball centre and is also the centre of the Cartesian co-ordinate system. The z-direction is pointing forward, along with the beam, x points left, and y up.

Target	Thickness (mm)	Density (mg×cm^{-2})	τ (10^{-3} barn^{-1})	Purpose (Reaction Type)
CH_2	2.3	106	9.14	Quasi-free scattering
C	2.0	185	18.56	Proton-removal reactions
Pb	0.18	199	0.58	Coulomb excitation
ET	-	-	-	Beam-background determination

Table 3.1: Summary of the targets used throughout the experiment with their respective thickness, areal mass density, and their τ parameter (the number of scattering centres per barn). The σ uncertainty of those parameters due to fabrication is 2 %. The ET target mentioned at the bottom refers to the empty target, *i.e.*, the measurement with beam but without target, in order to determine the background.

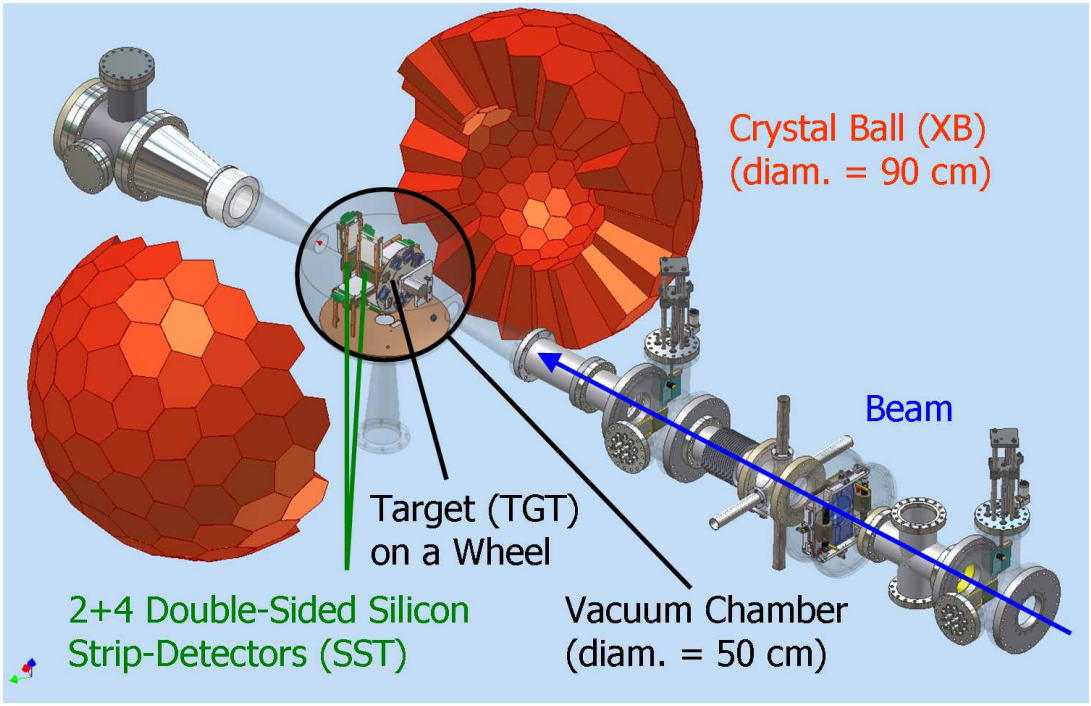

Figure 3.7: The incoming beam line (blue arrow) leads to a spherical vacuum target chamber (transparent), within which the targets (TGT) were mounted on a turnable wheel. Behind the target wheel, an array of silicon-strip detectors (SST) for beam and recoil tracking was placed. The chamber was surrounded by the Crystal Ball (XB), a 4π shell of 162 NaI crystals for γ-ray and charged-particle (proton, alpha) detection.

(±2 cm) around the beam line. Two SSTs for tracking heavy fragments and spectator-like protons were mounted ∼10 cm and ∼13 cm further downstream in the beamline. The target chamber is enclosed by the Crystal Ball (XB) detector, a 162-fold segmented 4π shell of NaI crystals for γ-ray and charged-particle (proton, alpha) detection. The following paragraphs will detail the SSTs and the XB further.

3.2.3.1 Silicon-Strip Detectors (SSTs)

The six double-sided Silicon-STrip detectors (SSTs) were of special importance within the setup. Two of them were placed in-beam, around 10 cm and 13 cm behind the target, with the purpose of tracking and charge-identifying heavy fragments down to protons. The four others were placed closer to the target around the beamline, forming an open box that tracks protons from quasi-free breakup reactions at large polar angles, hitting the surrounding Crystal Ball in coincidence. The two in-beam SSTs cover a polar angular range of $0° \leq \vartheta_y \leq 11.0°$ for fragments and protons, well sufficient for the opening angle of the beam exit tube of $\pm 5\,°$; the four box-SSTs for light recoils cover polar angles from $14.7\,°$ to $72.3\,°$, considering the XB centre, and the full azimuthal angle. The complete array is shown in figure 3.8a. The SST detectors as such are prototypes of the ones developed and used

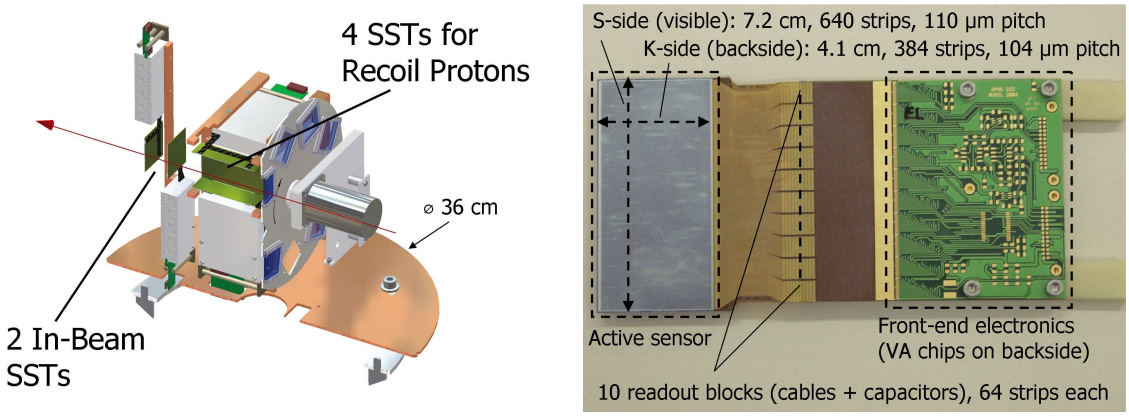

(a) The SST array with target wheel.

(b) A single SST sensor.

Figure 3.8: Views of the double-sided silicon-strip detectors. (a) View of a 3D drawing of the array of all six detectors (active sensors = dark green), mounted on a Cu-support plate (bottom, red). The target wheel with targets (transparent blue) is shown as well. The red arrow indicates the direction of the beam. (b) Photographic view of a single SST with its front-end-electronics board. The active area is rectangular with about $4{\times}7\,\mathrm{cm}^2$ in size. There are 640 vertical (long side) plus 384 horizontal (short side) strips. The in total 1024 strips are grouped in 10 (visible) plus 6 (rear side) blocks of 64 read-out lines each, which are capacitively linked to 10+6 VA-chips [55] with pre-processing on the front-end board.

.

by the AMS[17] collaboration [56], and were designed especially to possess a large dynamic range. They were tested to be able to charge-identify ions up to $Z = 22$ (Titanium) [57], combined with high spatial resolution.
The sensors' shape is rectangular, approximately $4{\times}7\,\mathrm{cm}^2$, with a thickness of $300\,\mu$m. The side where the strips are perpendicular to the long edge is called S-side, with 640 read-out strips at a pitch size of $d_S = 110\,\mu$m. Between two read-out strips, three floating strips are located that are not connected to any read-out channels; this design was chosen by the AMS experiment. The rear side is called K-side, having 384 read-out strips at a pitch size

[17] Alpha Magnetic Spectrometer.

of $d_K = 104\,\mu$m, perpendicular to the S-side. Figure 3.8b shows a photograph of the S-side of a SST sensor. As visible, the 640 S-side-strip signal lines are guided away from the active Si-area in 10 groups of 64 lines each. Similarly, on the rear K-side there are five signal blocks with 64 lines each. The strips are capacitively coupled to the front-end electronics *via* bond wires. Additionally there is an inherent capacitive coupling between neighbouring strips (see details in [57]), which leads to specific challenges in the calibration and event reconstruction (see chapter 4.4). Each 64-lined readout group is connected to a so-called VA-chip [55], which is a part of the front-end board. Inside them, to each individual line (strip) belongs an amplification, a shaping, and a track-and-hold stage. The SST readout is triggered externally and performed sequentially along a VA-chip and along the whole SST. Ions that penetrate an SST create e-h-pairs in the vicinity of their tracks, usually firing a group of neighbouring strips on both the S- and K-sides, which is called a cluster. Since more than one strip is involved, the resolution for the position of such a cluster is usually even better than the pitch of the strips; depending on the ion species one obtains about 30-100 μm.
For further reading, the basics of silicon-strip detectors in general may be found, *e.g.*, in [58]. More details on the AMS-type sensors, which were used for the presented experiment, can be found in the following theses and articles: [57], [59], [60].

3.2.3.2 The Crystal Ball 4π γ-Detector (XB)

The Crystal Ball (XB) is a 162-fold segmented spherical NaI(Tl)-shell of 90 cm diameter that was built at the end of the 1970s as a 4π γ-detector. It was designed to measure with high resolution the total and individual energies, angular distributions, multiplicities, and times of γ-ray(-cascade)s stemming from nuclear de-excitation processes [61].
In the 1990s the XB was brought to GSI and used together with the ALADIN-LAND setup in Cave B, for example for the study of the excitation of isovectorial giant-dipole and pygmy-dipole resonances in neutron-rich tin isotopes [62]. Since 2006 the Crystal Ball is installed within the R^{3}B/LAND setup in Cave C. The overall shape of the XB, as apparent in the 3D-drawings (a) and (b) in figure 3.9, and its crystal sub-units is governed by the geometry of a icosahedron and its further subdivision [61]. The individual crystals have been made from polycinic[18] NaI(Tl) and shaped as conical prisms of 20 cm length, which are canned in 600 μm aluminium shells. The crystals have either of four different basic shapes[19] but all covering the same solid angle of $4\pi/162 = 77.6$ mrad. The crystals are mechanically mounted to honey-comb-like stainless-steel support structures, visible in photos (c) and (d) in figure 3.9. The individual crystals are connected to PMTs, which transform scintillation light into electrical pulses. Those run through a frontend pre-amplification stage attached to the PMTs, before being cabled to an energy and a time readout, as sketched in figure 3.13. The XB's general properties and capabilities with respect to γ and also neutron detection have mainly been summarised in [64], [65], and [66], and will not be discussed further here.

[18] The material is not cut from a single mono-crystallite, but consists of many small sub-crystallites, that lead to reduced fragility whereas retaining similarly good scintillation properties [64].
[19] 12 regular pentagons (A), and 132 irregular hexagons (60 of B, 60 of C, and 30 of D).

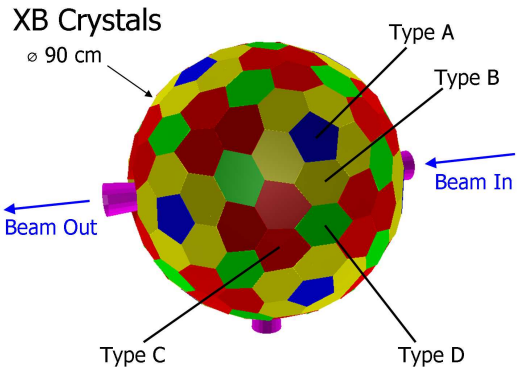

(a) Crystal Ball, crystal structure.

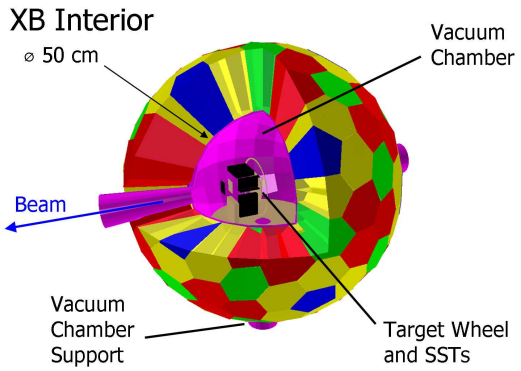

(b) Crystal Ball, with interior.

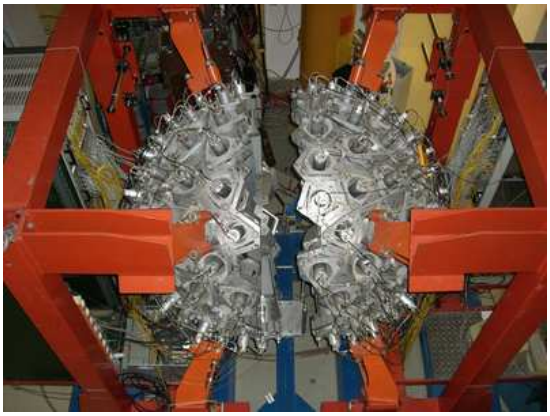

(c) Crystal Ball, partly opened.

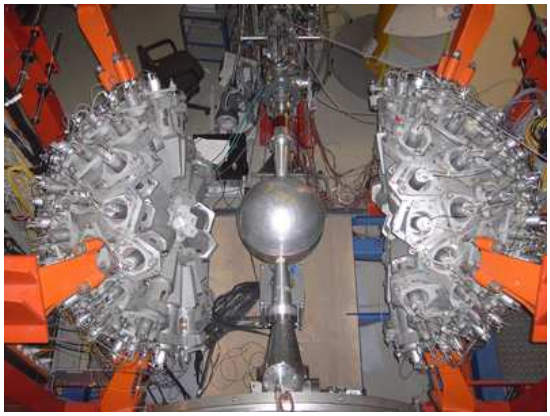

(d) Crystal Ball, fully opened.

Figure 3.9: Drawn and photographic images of the Crystal Ball. Upper panels: Visualisation of the crystals as such (a), and and with parts of the inner vacuum chamber and beam pipes (b) within the R3BRoot simulation framework [63]. Different elements are indicated by different colours: crystal types A (blue), B (yellow), C (red), and D (green), and Al-based vacuum elements (pink). Lower panels: Photos of the Crystal Ball with its full honey-comb-like support structures and front-end electronics, taken from above and against the beam line, with (d) and without (c) the central vacuum chamber installed. The two halves of the XB can be opened towards the left and right of the beam line.

3.2.3.3 High-Energy Proton Detection with the Crystal Ball

As a part of the technical developments flowing into the quasi-free-scattering programme planned at the future R^{3}B setup [67] for the future FAIR facility [68,69], an energy measurement of (p,2p) recoil protons was carried out at the Crystal Ball. Within the present work, the Crystal Ball readout system has been upgraded, and is now in operation in R^{3}B/LAND experiments. For the forward 64 crystals an additional low-gain energy readout for proton detection has been designed. The readout, as sketched in figure 3.10, consists of a capacitively coupled signal path to the PMT's last dynode (Dy8, rather than the final pickup

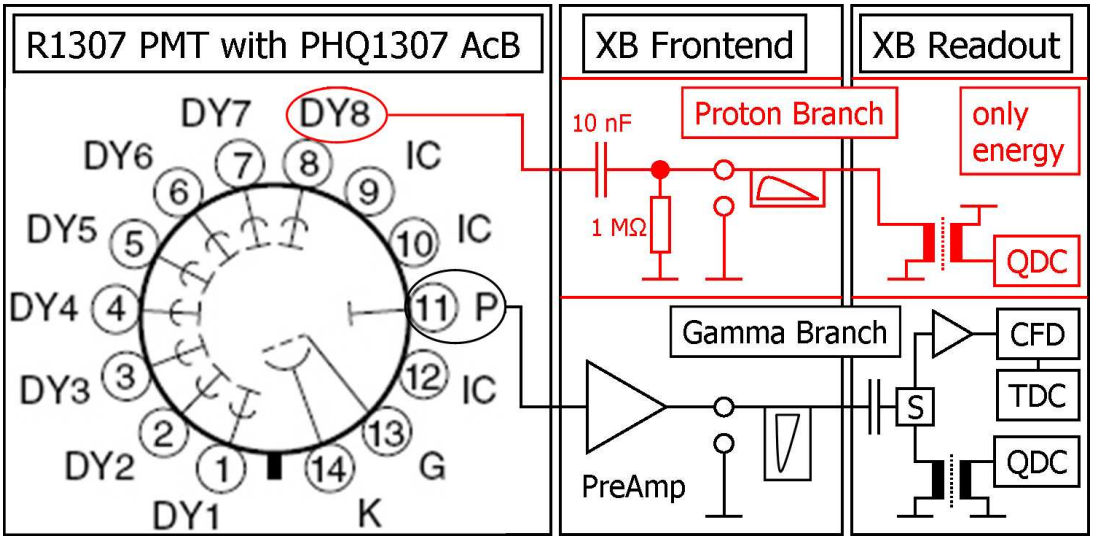

Figure 3.10: Scheme of the readout circuitry for the XB, highlighting the proton readout (red). An R1307 PMT (Hamamatsu, Inc.) is attached to a crystal and operated *via* a PHQ1307 Active Base (iseg GmbH). Their pin-out schematics are shown on the left. The standard gamma signal line is read from the pickup anode (P), the proton line is coupled to the last dynode (Dy8), omitting the last electron-multiplication stage. The gamma signal, which has negative polarity and a decay constant of about 200 ns, is pre-amplified, capacitively decoupled, and split into a standard energy-branch with QDC readout, and a time branch with CFD discrimination for triggering and TDC readout, as is shown in greater detail in figure 3.13. The much weaker proton signal, in contrast, has positive polarity, and a larger decay time of about 1 μs. The signal is fed into a QDC for energy measurement, after a polarity switch *via* an inductive coupling.

anode P), and is also not pre-amplified further. The gain of this so-called proton readout is about 15 times smaller than the corresponding gain of a PMT's standard gamma readout. The pulses have positive polarity and are broad (about 1 μs decay length) compared to the gamma readout's narrow (about 200 ns) pulses with negative polarity. While the gamma-signal path is equipped with the usual energy and time measurement and triggering using a standard splitter, CFD, TDC & QDC readout, for protons only an energy measurement is done using a QDC.

The new readout was tested in May 2007 in direct irradiation with primary proton beams at four different energies. Figure 3.11 shows the setup used for the tests in Cave C and figure 3.12 presents the obtained data in terms of proton energy loss spectra in the crystal. The results of this test point out several aspects of high-energy-proton measurement with the XB NaI crystals:

- If the proton energy is low enough so the protons are stopped in the crystal, *i.e.*, for $\Delta E = E$, the achievable full-energy-peak resolution is very good, better than 2 % even for high energies between 180-240 MeV.
- If the proton energy is high enough so that the beam punches through the crystal,

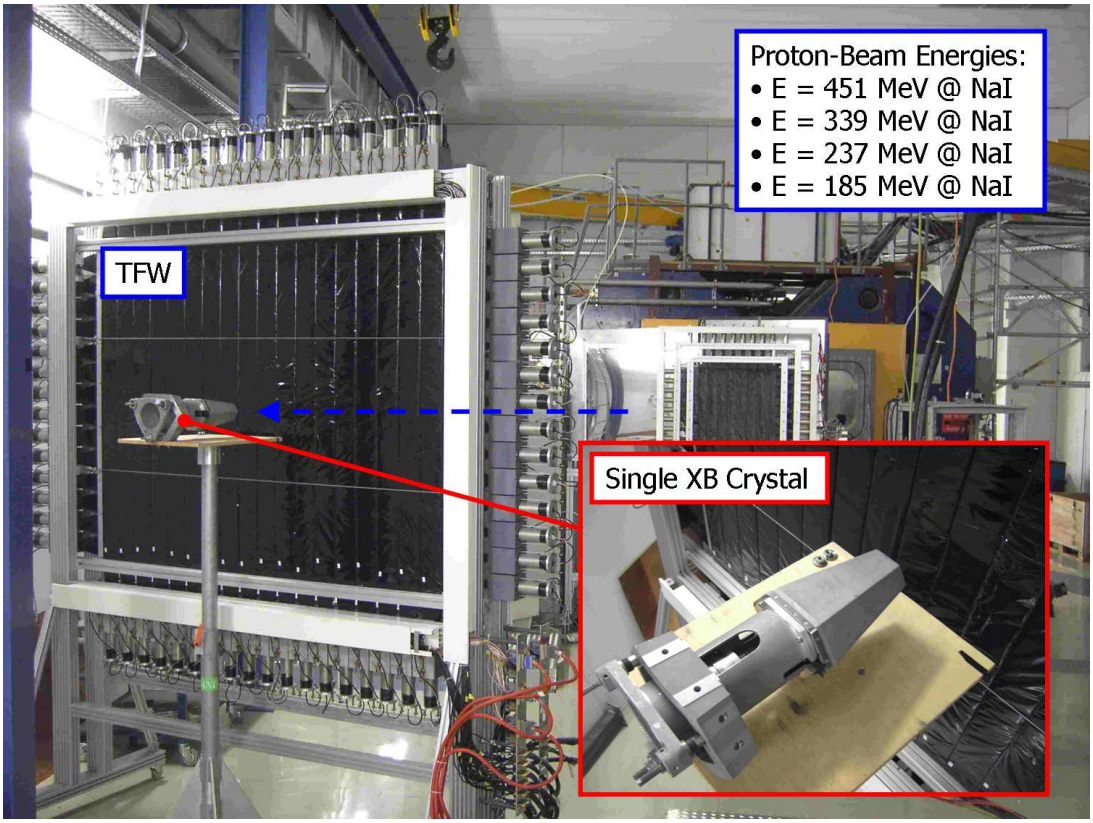

Figure 3.11: Setup for testing the response of an XB crystal (behind the TFW) to relativistic proton beams at energies of 451, 339, 237, and 185 MeV. The heavy-ion-stopping code ATIMA [70] predicts for a NaI crystal of 20 cm to fully stop protons with an incident energy of up to 275 MeV, *i.e.*, the beams of the two lower-energy settings.

only a fraction of its energy is deposited, $\Delta E < E$, and the relative resolution worsens to about 5 %.

- In addition to the achievable energy resolution of the events due to purely electromagnetic processes, the background from nuclear reactions is not negligible. Even for fully stopped protons, about 50 % of the observed events belong to the continuous energy background below the full-energy-deposition peak.
- The determination of the energy of penetrating protons is (even) more complicated. The electronic-energy-loss peak drifts again towards lower energies, leading to an ambiguity in the energy measurement with stopped and punch-through protons. Additional high-energy background from nuclear reactions appears at energies higher than the electronic-energy-loss peak.

3.2.4 Data Acquisition and Triggers

As already mentioned earlier, the data collection within the R^{3}B/LAND setup is performed in terms of events, on an event-by-event basis. What that means is the following:

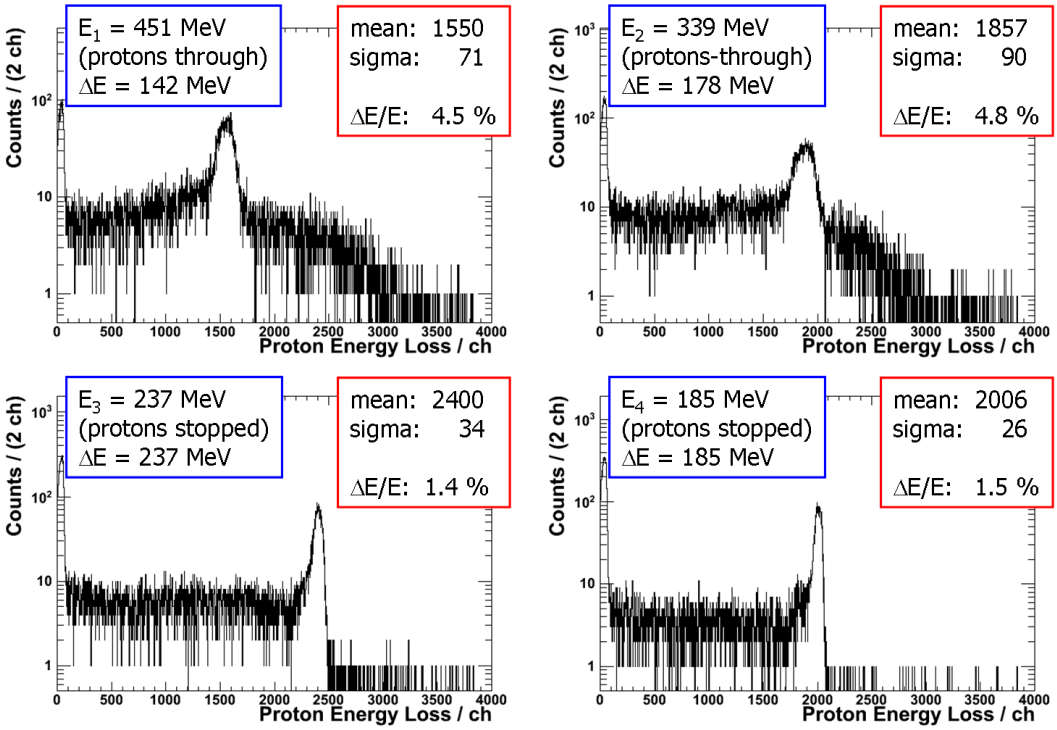

Figure 3.12: The energy-loss distributions of proton beams at four different beam energies measured with an XB crystal. The penetrating protons (top row) show a broader energy-loss distribution than the fully stopped ones (bottom row).

The signals that detectors see during an experiment are logically grouped as sets of data that belong to the incidence of a particular beam or cosmic particle and the products of the potential reactions that it might undergo. The Data AcQuisition (DAQ) program together with the trigger logic as the brain of the experimental setup has to manage the identification, selection (by means of triggers and their downscale), and storage of such events into data files. The individual detector channels within the setup (semiconductors, scintillators, etc.) usually deliver an analog electrical signal, which is pre-amplified and/or shaped, before it is split in order to obtain both energy and time information of a particle. The corresponding readout scheme and the interplay with the DAQ is schematically illustrated in figure 3.13. Consider a signal from a crystal of the XB. The energy branch of a signal is delayed (typically 500 ns) and then directly sent to a QDC for (possible) digitisation and readout. The delay is necessary to give the DAQ time to decide whether or not a signal is viable (or interesting) for readout at all.
The time branch is, after further amplification and shaping, guided to a CFD[20] that has various outputs. If the signal is large enough to pass the internal threshold, a logical signal will be created, delayed, and arrive at a TDC[21] that measures the time difference relative to a common-stop signal sent by the DAQ, if the event is to be recorded. The CFDs in that case also feed a scaler, to simply count the rate of that detector. As a third option, a CFD

[20] Constant-Fraction Discriminator.
[21] Time-to-Digital Converter.

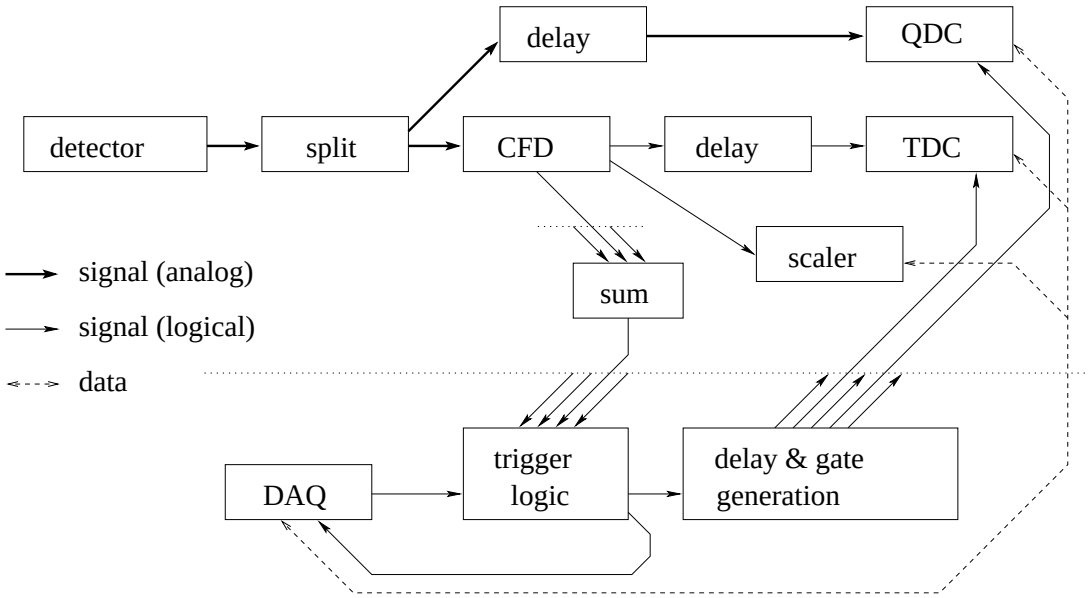

Figure 3.13: Schematics of the interaction between a detector signal and the DAQ, intermediated by triggers and the time- and energy-readout modules. Figure taken from [49].

creates logical signals used for trigger decisions. Typically, a CFD electronic module hosts eight inputs from different detector channels; for example, a CFD does host eight time-branch channels of different XB channels. A logical OR (if any crystal produced a signal above the threshold), or an analog-sum signal of the eight inputs is created continuously, and combined with further CFD modules in order to create a global OR and a global sum of the whole XB detector. Such higher-level signals, also from other detector systems, are fed into the trigger logic to create triggers (see chapter 3.2.4.1) for the DAQ.
When the DAQ is not busy and receives such a trigger, *e.g.*, an XB OR trigger that might be related to one of the crystals having registered a γ-ray from an excited fragment from a reaction, it issues a master trigger to initiate digitisation, and steers the electronics to read and store all the data available from all the detector subsystems. For example, the QDCs will be provided a time gate within which they will integrate signals from detectors (which will arrive in time since they have been delayed long enough). *Via* various processors, the data of all active detector channels is collected, combined into packets called events, and written to LMD-format files[22]. For further reading on the details of the functionality of the R^{3}B/LAND DAQ, the reader is suggested to have a look into the recent theses of Le Bleis [71] and Johansson [49, 72].

3.2.4.1 Triggers

As exemplified in the previous section, triggers are logical signals stemming and created from one or usually multiple individual detectors meeting some predefined requirements; for example, a trigger might occur if at least five subchannels of detector X register a pulse of

[22]LMD = List Mode Data.

Produced Trigger			Required Signal(s)					
Tbit	Tpat ($= 2^{Tbit-1}$)	Name	POS!ROLU	NTF mul	XB OR	XB Sum	TFW mul	Spill on
1	1	Good Beam	x					x
2	2	Fragment	x	x				x
3	4	XB OR	x	x	x			x
4	8	XB Sum	x			x		x
5	16	Proton	x	x			x	x

Table 3.2: The list of beam-related triggers. Names of the triggers (and their Tbit and Tpat) on the left, required coincident detector signals on the right.

at least 100 mV amplitude at the same time. Obviously, the nuclear-physics experimentalist chooses (or constructs) triggers to be able to tag (or filter) the potential reaction channels of interest, usually as a combination of certain detectors registering something in coincidence. With the LAND/R^{3}B setup, triggers corresponding to a certain reaction channel are identified by a certain trigger bit (Tbit) and a corresponding trigger pattern (Tpat), as shown in the summary of the following table 3.2. For example, the Good Beam trigger stands for an event with a potentially good and usable incoming ion; as the right-hand side of table 3.2 shows, it requires the Spill-on logical signal from the accelerator, plus a signal from POS, in anti-coincidence with ROLU. Fragment stands for events in which additionally the NTF has a heavy-fragment hit; such events either stem from unreacted beam, or from not too violent reactions, letting some part of the projectile survive. As specific reaction triggers, XB OR is sensitive to γ-rays registered in the XB, XB Sum is the most interesting trigger for quasi-free-scattering reactions, as it requires a high-energy deposit in the XB, and Proton stands for a hit in the TFW ToF-wall that indicates a hit from a forward proton.
The following chapter will show selected cases of the calibration of the experiment.

4

Calibration and Reconstruction

The present chapter provides an overview of the various elements of calibration and reconstruction necessary on the way from raw binary data produced by the Data AcQuisition (DAQ) during the experiment operation to meaningful physics observables such as energies and momenta.
Firstly, the employed analysis framework of land02 will briefly be presented. This is followed by a section on the practical aspects of calibration, with a focus on those detectors that are fundamental for identifying and selecting the desired reaction channels.

4.1 Overview of the land02 Calibration and Analysis Software

Since about five years the LAND experimental group at GSI uses a programme suite called land02 which in an integrated way serves as an unpacking, calibration and reconstruction tool for the GSI-typical experimental-data list-mode (.lmd) files. A majority of the calibration and reconstruction work for the analysis of the present experimental data has been performed within the framework of these land02 programmes.
The basic idea of what land02 does with experimental data is presented in figure 4.1. As a rule of thumb, data is generally reconstructed *via* several steps or levels from RAW (*e.g.*, ADC channels) to HIT (time relative to the target in ns, position within a detector in cm, energy loss in MeV of a hitting particle) level, and possibly beyond. Each level of reconstruction requires specific calibration parameters provided by calibration routines and suited data. The reconstruction algorithms (and the necessary calibration routines) are detector-specific, but many are similar and all are integrated and categorised within the land02 framework. The corresponding data levels, as already partially sketched in figure 4.1, are shown in the following:

RAW: Data provided in units of channels (commonly 12bit, 0-4095), for typical ADC-, QDC-, or TDC-based readouts.

TCAL: Individual energy channels are corrected for their default-current offsets (pedestals) in QDCs; TDC times are transformed from channel units to ns.

SYNC: Energy channels of a detector are gain-matched and (if already possible) transformed into units of MeV. Time channels of a detector are put to a common offset.

DHIT: Detector hits are reconstructed (positions, times, energy losses) using detector-internal coordinates.

HIT: Hits on detectors are reconstructed in terms of physical units: cm, ns, MeV.

TRACK: Particle tracks are combined from the hits in various detectors into trajectories, ultimately described by their ID and momenta at the reaction target.

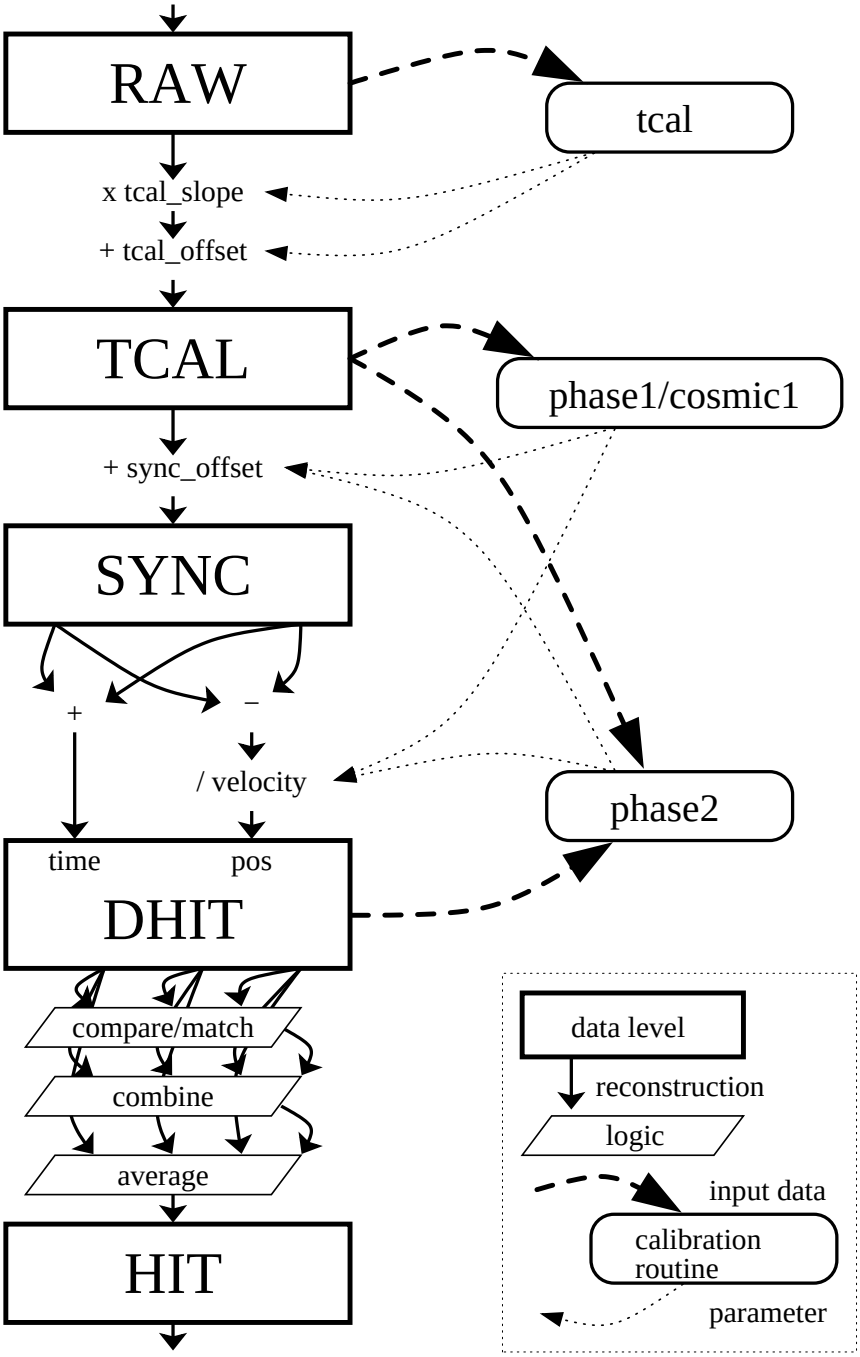

Figure 4.1: Scheme of the data reconstruction flow with land02. Starting with RAW in the top, boxes with sharp corners in the left column represent the data levels that can be reached, as soon as the needed calibration parameters are provided. The boxes with round corners on the right represent calibration routines/programmes that are used to produce the calibration parameters. This figure is taken from [49], and it show-cases the reconstruction of ToF-wall data, such as the NTF (figure 3.5b) or the TFW (figure 3.6b).

Each step of reconstruction requires the corresponding set of calibration parameters, *e.g.*, the gain factor that transforms QDC channels to MeV. Also needed is a programme that determines those calibration parameters from a class of well-determined events. These could be, *e.g.*, photons from a radioactive sample (*e.g.*, 1.275 MeV γ-rays from a ^{22}Na-source) for calibrating a γ-detector (see chapter 3.2.3.2), or ion-beams with known charge (read: atomic number Z) that suffer a well-defined energy loss in any scintillator paddle of a ToF-wall, thus enabling to match the gains of each paddle versus each other.
For the present analysis, the land02 framework (Johansson [49,72], Paschalis [29], Plag [73], Aksyutina [74], and Mahata [52]) has been developed (chapter 4.4) and used for calibration and reconstruction of the data up to the DHIT or HIT level for the majority of the detectors, and, in the case of the detection systems in front of the target (see chapter 3.2.1 and 4.2) up to TRACK level.

4.2 Identification of the Incoming Beam

The detectors described in chapter 3.2.1 serve to identify incoming-beam particles. As soon as their time and gain calibrations are performed, their data determines the ions' times, positions and energy loss in physical units[1].
Within land02 the procedure of determining an incoming projectile's Z_{proj} from its velocity β_{proj} (*via* the ToF from S8 to POS) and the energy loss ΔE_{proj} (in PSP1 and PSP2) is performed[2] using a simplification of the well-known Bethe-Bloch formula (see [58]):

$$Z_{proj} \quad \sim \quad \beta_{proj} \times \sqrt{\Delta E_{proj}} \tag{4.1}$$

All correction terms are discarded there, and only the leading-order term in β_{proj} is taken into account. Furthermore, the differential energy loss dE/dx is assumed to be constant along the penetration thickness Δx through the PSP detectors — an acceptable approximation considering the high beam energy. Figure 4.2 shows the A/Z vs. Z identification plot produced with land02. Although the FRS had been tuned for an ^{17}Ne-only setting, various neighbouring isotopes at lower intensity were by-travelling as seen in figure 4.2. Nevertheless, ^{17}Ne is dominating, and the majority of events falls into the dashed-line polygon that is selected for further analysis. Events being visible as long tails along Z can be attributed to pile-up or missing position information in the PSPs that results in bad energy reconstruction.

4.3 Identification of Outgoing Particles

In addition to the incoming-channel particles, also the outgoing-channel particles need to be identified, in order to reconstruct and select the respective reaction channels of interest.

[1] Although abbreviated here, position and energy-loss calibrations of the PSPs are not trivial. Position information is needed to correct the energy loss, and vice-versa, usually resulting in an iterative calibration procedure; furthermore calibrations are usually run-time dependent (see [29] for the details).

[2] The projectile's charge state is equal to its atomic number Z_{proj} due to full ionisation at about 75 %c when passing any material.

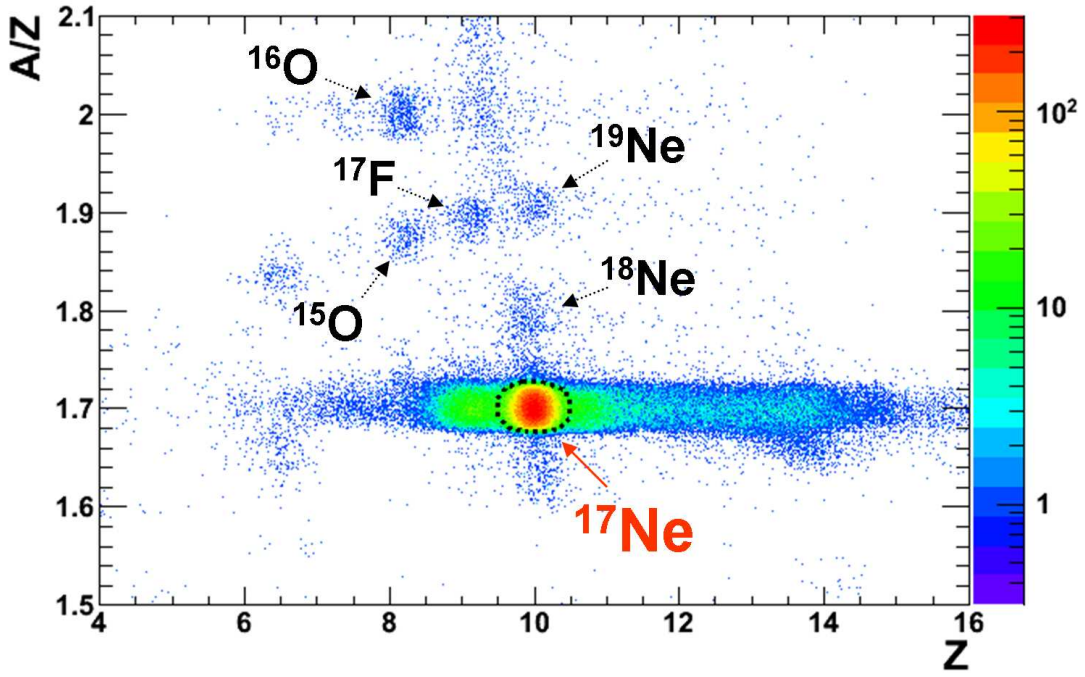

Figure 4.2: Example plot for the identification (ID) of the incoming beam, with no specific trigger (Tpat) selected. The events falling into the dashed-line polygon (^{17}Ne) are selected for the analysis. Long tails along Z are visible; as Z is determined from the energy-loss measurement with the PSPs, they can obviously be attributed to pile-up. Further accompanying ion species, such as ^{16}O, ^{17}F, and others, are exemplarily highlighted.

4.3.1 Heavy Fragments

After all calibrations, the NTF energy loss and position information on HIT level can be used to identify and select different atomic charges, *e.g.*, neon, oxygen, or others. Figure 4.3 shows how reacted (^{17}Ne $\rightarrow$ $^{\leq 15}$O) and unreacted (^{17}Ne $\rightarrow$ ^{17}Ne) events[3] are selected. The average of the x distribution of neon is located at larger x values, corresponding to being bent more strongly than oxygen, as its magnetic rigidity is smaller. However, the overall distribution of oxygen is broader, which can be attributed to the fact that it stems from inelastic reactions that introduce a larger velocity spread.

4.4 Calibration of the SST detectors

The SST detectors are used for both, ΔE and position measurements. They observe protons and heavier fragments of the final state being emitted in forward direction. This section

[3]Although no mass identification has been done yet at this stage, it is fair to claim that any neon detected in the NTF will be ^{17}Ne, since one-neutron removal would lead to the unbound ^{16}Ne, and any neutron-pickup at these beam energies is rather improbable. But, oxygen isotopes different (lighter) than ^{15}O can be expected.

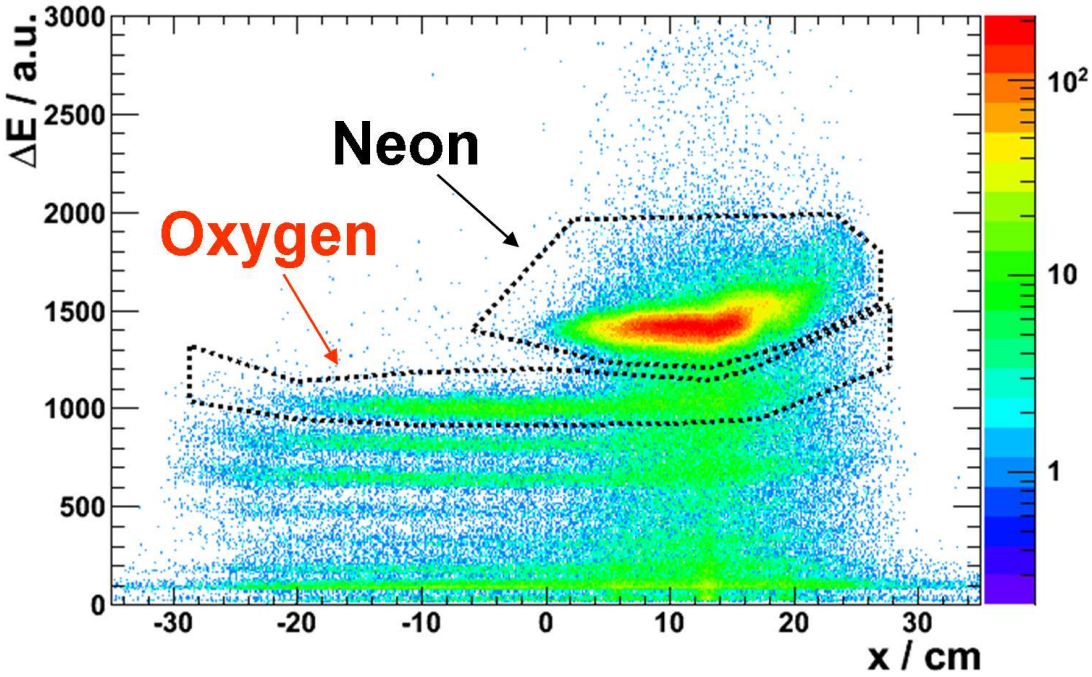

Figure 4.3: Fragment-charge ID using the NTF ToF-wall. Shown is data taken with the CH_2 target; incoming ^{17}Ne, an NTF multiplicity of 1, and no specific trigger are selected. The NTF-intrinsic x axis points to the right (positive values). The "neon"-labelled locus reflects the unreacted beam (practically only ^{17}Ne, since lighter neon isotopes are unbound, and neutron capture is unlikely), which is rather narrow and bent more strongly (to larger x values). Oxygen isotopes (^{15}O, ^{14}O, and ^{13}O) stem from ^{17}Ne breakup in the target (or any other material in front of the NTF). They show a broader distribution, but are in average less strongly bent, due to their higher rigidity. The events enclosed by dashed lines around neon and oxygen are selected for further analysis. Other atomic charges (nitrogen, carbon, ...) are visible, but not taken into account here.

is supposed to give an overview of their working principle, what type of data they deliver, and highlight the essential steps of calibration, especially for the purpose of an energy loss measurement.

4.4.1 Charge and Position of Ion Hits

The SSTs are double-sided silicon-strip detectors with their longer edge called S-side and their shorter edge called K-side, as described in chapter 3.2.3.1. When a charged particle (*e.g.*, a heavy ion or a proton) passes the detector, on either readout side a number $N_{S,K}$ of neighbouring strips is 'firing'. Such a group is called cluster and is shown in figure 4.4 as an example of a penetrating ^{17}Ne ion. Considering either S- or K-side, the respective total charge Q (also called cluster sum or cluster area) is calculated as the sum of the charges q_i

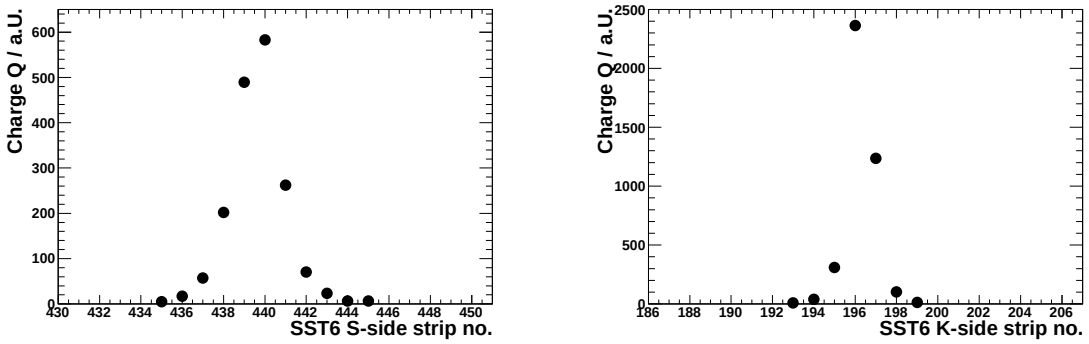

(a) S-side cluster.

(b) K-side cluster.

Figure 4.4: Example of a ^{17}Ne ion registered in SST6; x-axes indicate strip numbers and y-axes signal height. On both the S-side (a) and the K-side (b) multiple strips are responding. From the centres-of-gravity the S- and K-position of the ion hit is determined, whereas each sides integral signal (cluster sum) can be related to the particle's energy loss. Typically for neon, such clusters involve 8-10 strips on the S-side, in contrast to only 5-6 strips on the K-side with a much more pronounced central strip.

seen by the strips (numbered n_i) belonging to the cluster:

$$Q \quad = \quad \sum_{i}^{N} q_i. \tag{4.2}$$

The hit position is then calculated as the charge-weighted centre of gravity (CoG) of the corresponding (S- or K-side) cluster:

$$CoG \quad = \quad \frac{\sum_i^N n_i \times q_i}{\sum_i^N q_i} = \frac{\sum_i^N n_i \times q_i}{Q}. \tag{4.3}$$

Now, the observed CoG indicates the hit position in units of the strip number. In order to distill a cluster's position $X_{S,K}$ on the S- and K-sides, respectively, the CoG has to be multiplied by the strip pitch ($d_{S,K}$), *i.e.*, the distance between the centres of two strips, which in turn is equivalent to the net active width that can be attributed to each single strip:

$$X_{\mathrm{S,K}} \quad = \quad CoG \times d_{\mathrm{S,K}}. \tag{4.4}$$

The position of a cluster can be translated to the hit position of the ion in the lab system, and the cluster charge is associated to the energy loss and thus used to identify and separate atomic charge. However, for the cluster sum (*i.e.*, charge, or energy loss) determination, things are a bit complicated, and several calibration and correction steps are necessary in order to obtain a homogeneous and position-independent response.

4.4.2 Inter-Strip Dependence and η-Correction

The capacitive coupling of the strips with each other along their readout lines leads to a inter-strip dependence of the registered total charge (cluster sum)[4], also called η-dependence or η-effect. The η-parameter ($\eta \in [0, 1[$) is defined as the decimal part of a cluster's CoG, and is a measure for whether an ion hits the detector centrally on a strip, or rather in between two strips:

$$\eta \quad = \quad CoG - \lfloor CoG \rfloor. \tag{4.5}$$

An η of 0 is associated with a central strip hit, η of 0.5 signifies a hit exactly between two strips (η of 1.0 would be centrally hitting the next read-out strip). Because of different geometrical layouts (strip length and pitch, etc.), the η-effect is different for the S- and the K-side, and it also depends on the penetrating ion species. Figure 4.5 visualises the η-dependence (and its compensation) of the total cluster charge of ^{17}Ne ions registered at the K-side of the second in-beam silicon-detector, SST6. For convenience, the peaks of the corresponding cluster-sum distribution have been adjusted to the common value of 5000 a.u. of energy loss, for the 3S, 3K, 6S, and 6K sides. The η-examples in this chapter all refer to K-sides, because for the S-sides with the neon-related profile is flat.

4.4.3 Gain Correction

In addition to the η-effect, which is a global feature common to all strips of a SST readout side, the strips' individual response (or gain) is different due to two reasons: Firstly, they are grouped into numbers of 64 with their data processed by a common frontend VA-chip, secondly each integrated amplifier on a VA-chip can simply have a different gain. Therefore, after the η-correction, a gain-correction routine is applied to each strip. This is achieved by plotting the ^{17}Ne cluster sum (total-charge, energy-loss) distribution for each strip[5], fitting the distribution by a Gaussian, and determining a correction factor needed to match up to the reference value of 5000 a.u..

4.4.4 Dead Strips and More

Certain irregular and singular effects also play a role for the SST charge measurement, and they have to be treated individually.

Dead Strips Dead strips are strips that are not read out properly, or not at all. That might be due to a disconnected bonding wire, for example. Practically, when involved in a cluster, those strips are not delivering any charge signals themselves; for some of them that charge is completely lost (short circuit, ...), for others their registered charge flows into the signal of neighbouring strips instead. Without going into too much detail, in the latter case it is possible to reconstruct the original cluster-charge distribution by means of more

[4] De facto, a similar effect also plays a role for the position determination, but it has been neglected here.
[5] That means all clusters are plotted whose CoG is within ± 0.5 strip pitches around that strip.

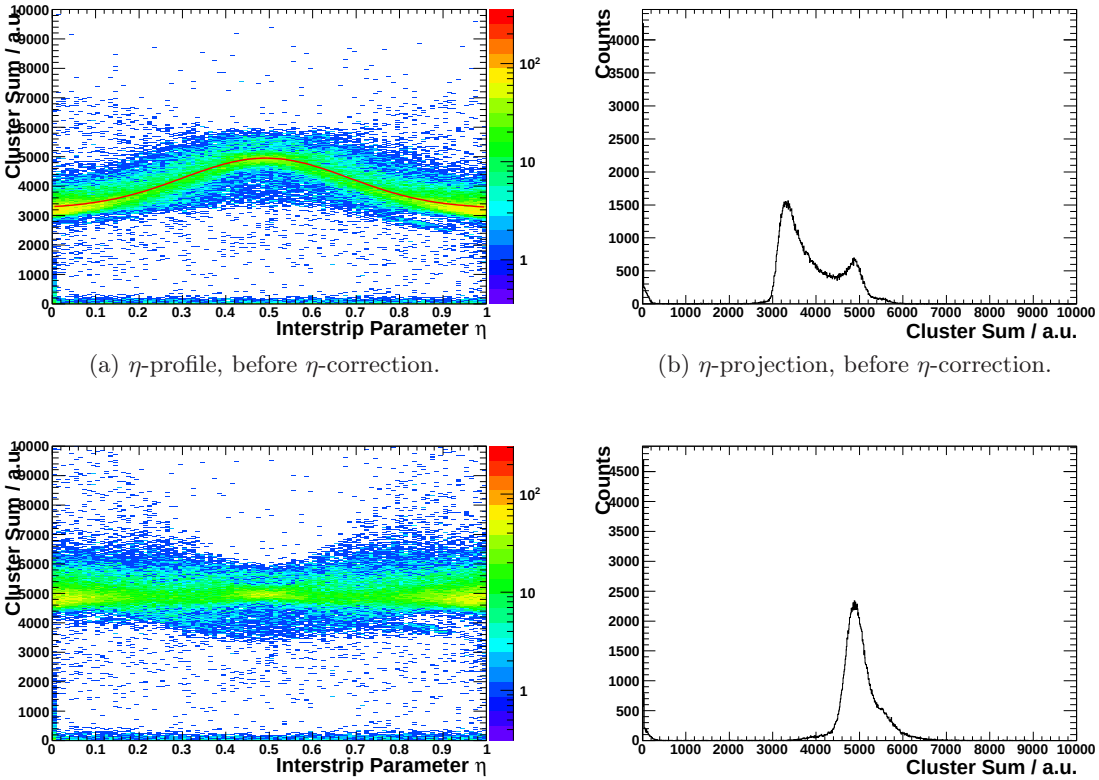

(a) η-profile, before η-correction.

(b) η-projection, before η-correction.

(c) η-profile, after η-correction.

(d) η-projection, after η-correction.

Figure 4.5: Inter-strip dependence of the cluster charge for ^{17}Ne at the K-side of SST6 and its compensation. (a-b) Initial situation. The left plot displays the cluster charge as function of the inter-strip (η)-parameter, with η=0 corresponding to a central hit of the left strip, η=0.5 to a hit in-between two strips, and η=1.0 to a central hit of the right strip. The distribution is maximum for inter-strip hits, and is fitted by a fourth-order polynomial (red solid line). The right plot shows the projection of the distribution onto the charge axis; the two peaks obviously indicate bad resolution. (c-d) After correction. A flat charge-vs-η distribution (left side) is obtained, resulting in a better charge resolution.

or less straight-forward algorithms. In the case of completely dead strips, recovery is more complicated, sometimes impossible, with the effect of a ∼100-200 μm wide acceptance hole in the detector. Figure 4.6 depicts data from a series of strips and dead strips of SST3-K with consecutive levels of correction and recovery.

Coupled Strips There are examples of strips that are coupled to each other (in a different than normal way), possibly by a faulty capacitance between them. As a result, the typical η pattern takes a different period along them, *i.e.*, with fewer nodes. By identifying that period change the correction for those strips can be adjusted easily, see the highlighted strips in the top panel of figure 4.7.

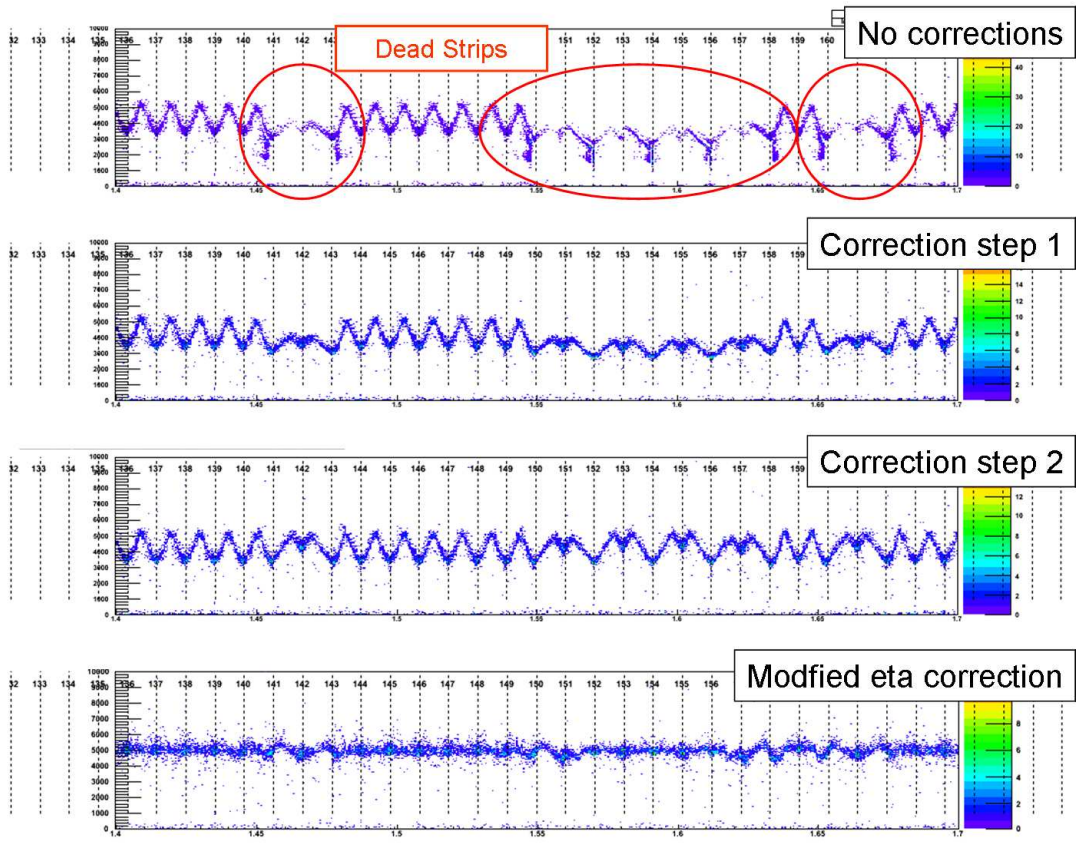

Figure 4.6: ^{17}Ne cluster sum distribution over a series of good and dead strips in SST3-K. Strips are numbered, centres of strips are indicated by dashed lines. Top panel: raw data, strong drops and gaps are apparent. Panel 2 to 4: various recovery steps that involve, *e.g.*, identify both sides next to a dead strip as belonging to a cluster, scaling up of the distribution, and performing a modified η-correction.

VA-chips borders It happens that strips in the vicinity of borders between VA-chips show a slightly distorted (or better: shifted) response. Presumably due to slightly different electrical potentials between neighbouring readout groups, something like a phase shift of the η-profile occurs. Such a stretch followed by a compression of the profile is handled by modifying the η-phase in that region. Figure 4.7 shows an example of the effect and its compensation, using data of ^{17}Ne at 500 AMeV. In principle, the detector response, and specifically the η-correction, is different for different atomic charges and velocities. For practical reasons the calibrations are applied not only for neon, but also for oxygen and potential protons.

4.4.5 SSTs for Fragment-Charge Identification

Having performed all the calibrations and recovery procedures as elucidated above, the corrected total-charge cluster-sum data is used for the charge identification (ID) of the

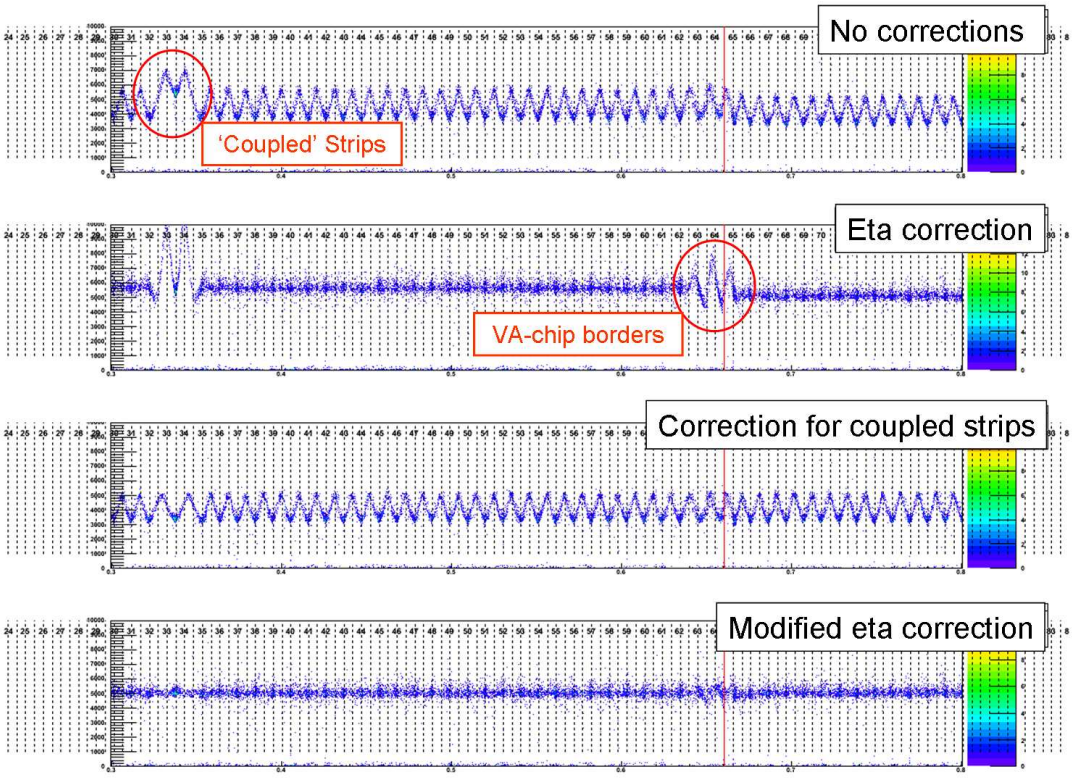

Figure 4.7: Several calibration steps for the K-side response of SST6 to neon, energy in arbitrary units on the y-axis, position in cm on the x-axis. Strips and their dimensions are indicated by their strip numbers and black dashed lines; borders between VA-chips are indicated by red solid lines. The upper panel shows the position-dependent energy response before the eta-correction; the red solid circle indicates two coupled strips. In the second panel the η-mismatch at the VA-chip borders is highlighted in the same manner. The two lower panels show first the compensation of those effects and the result of the modified η-correction.

fragments that leave the target. Figure 4.8 shows events that have been identified as oxygen in the NTF. With the energy loss signals of the SSTs a lot of those events (∼60-70 %) are identified as neon (leaving the target) and are ruled out as background stemming from breakup further along the beam line.

4.5 Calibration of the Crystal Ball

As outlined earlier, as an important measure to identify and select protons from (p,2p) reactions, the Crystal Ball (XB) has been equipped with an additional readout (see chapter 3.2.3.3). Simultaneously, of course, the XB is used as a γ-ray spectrometer and calorimeter. First, the calibrations for the standard γ-ray readout are shown. Later in this section, a presentation of an energy calibration of the proton readout will follow; that gain-matching procedure is based on the previous calibration of the γ-ray readout.

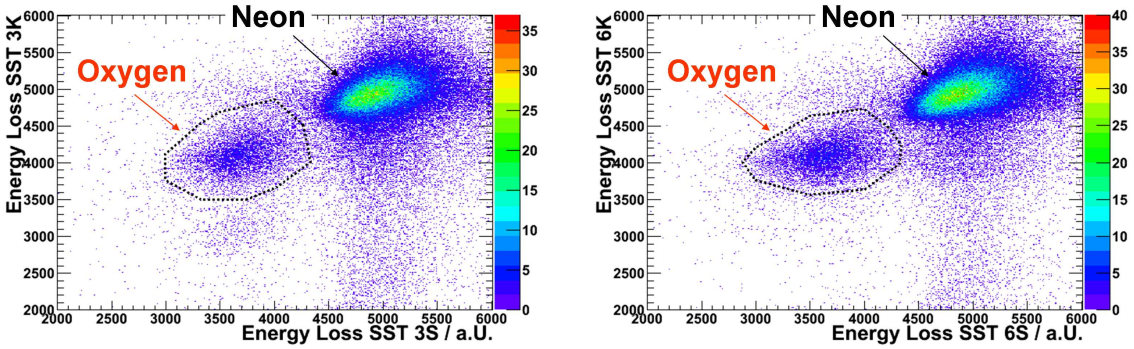

(a) SST 3K vs. 3S.

(b) SST 6K vs. 6S.

Figure 4.8: SST energy-loss (cluster-sum) distributions in coincidence with oxygen in the NTF. All axes show energy loss in arbitrary units. (a) SST3: K-side vs. S-Side: neon and oxygen hits are seen as separated loci. (b) SST6: correspondingly. Although having selected oxygen with the NTF, both SSTs still register a majority of neon events (60-70 %). Those events can be attributed to ^{17}Ne breaking up into oxygen behind (and not within) the target. Contributing material are the SSTs and all the material in the beamline that follows: the vacuum window, the helium in ALADIN, the GFIs, and the air between the fragment-arm detectors. The events enclosed by the black dotted polygons are selected for further analysis and tracking.

4.5.1 Crystal Ball γ-Readout

4.5.1.1 Energy

The energy calibration was performed with standard γ-detector calibration sources: ^{22}Na (photons of 511 keV and 1275 keV, activity of 85.5 kBq), and ^{88}Y (photons of 898 keV and 1836 keV, activity of 10.9 kBq). The respective source was placed at the centre of the XB, in the middle of the (air-vented) vacuum chamber at the target position. The whole XB was kept running at experiment conditions, and the DAQ took data with the offspill XB OR trigger. A semi-automatic calibration routine for RAW level data has been written that fits each peak with the superposition of a Gaussian peak plus a linear background in the vicinity of the peak ($\pm 3\sigma$). Figure 4.9 shows the fits to the raw ^{22}Na and ^{88}Y spectra, for crystal #162. Using the positions of those four photo peaks, a linear-regression fit was performed in order to determine the calibration parameters of the linear energy-versus-channel relation.

$$E(\mathrm{ch}) = \mathrm{gain} \times (\mathrm{ch} - \mathrm{offset}), \tag{4.6}$$

$$E(\mathrm{ch}) = p_1 \times (\mathrm{ch} - p_0). \tag{4.7}$$

The gain of the whole electronic chain (from detector to QDC) is identified as the (keV/ch) slope of the fitted straight line[6], the determined offset is equivalent to the pedestal of the

[6] This relation is indeed linear for the presented readout with the XB. Offside this experiment we recorded data with a PuC source (photons at 6.13 MeV from the ^{13}C+$\alpha \rightarrow {}^{16}$O* reaction) which confirmed the assumption of linearity up to this energy range.

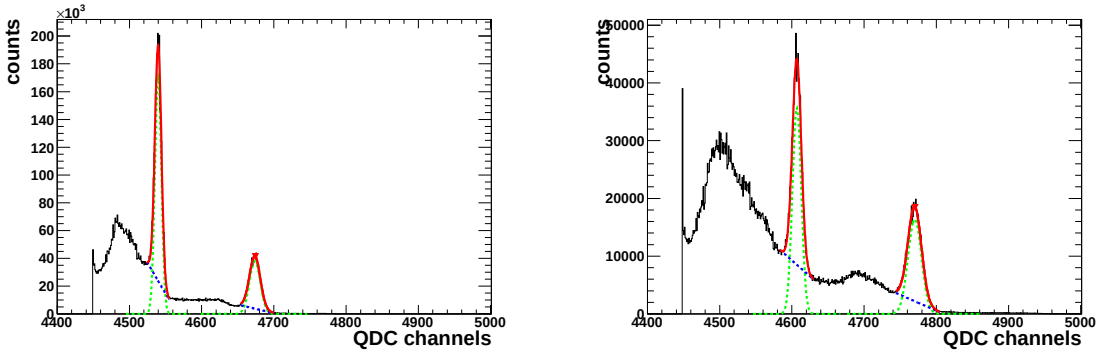

(a) Fitted ^{22}Na spectrum for crystal 162.

(b) Fitted ^{88}Y spectrum for crystal 162.

Figure 4.9: Example of the γ-ray energy calibration of the Crystal Ball, with crystal 162. The photo peaks in the ^{22}Na (511 keV and 1275 keV) and ^{88}Y (898 keV and 1836 keV) spectra (red solid line) are locally fitted as the superposition of a Gaussian (light-green dashed line) and a linear function (blue dashed line). The sharp peaks at the left end of the spectra at channel number 4450 are the remainders of the cut-off pedestals and signify the zero-energy point of the electronic chain.

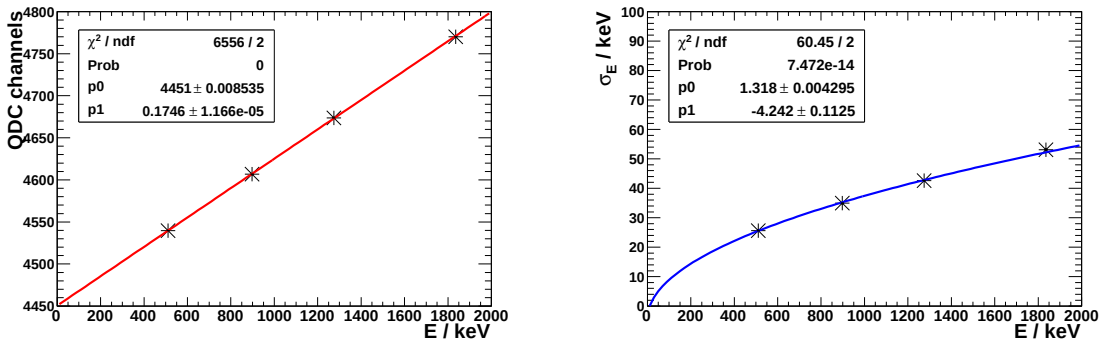

(a) QDC channel vs. γ-energy for crystal 162.

(b) Energy resolution vs. γ-energy for crystal 162.

Figure 4.10: Parametrising the gamma response of an XB channel. (a) The measured gamma-source peak positions (in QDC channels) as a function of the corresponding photon energy are fitted linearly and thus determine gain (p_1) and offset (p_0) of the $E = E(\mathrm{ch})$ relation. (b) The energy-dependent energy resolution (in terms of the σ_E width of the corresponding Gaussian) is fitted with a $\sigma_E(E) = p_0 \times \sqrt{E} + p_1$ function.

corresponding QDC channel[7], *i.e.*, the zero-energy point. An example for such a straight-line fit is shown in figure 4.10a, again for crystal #162. Furthermore, figure 4.10b shows the

[7]Actually, the offset and the pedestal are not numerically identical, and the offsets determined by the fitting procedure are systematically higher by about 10 channels. The reason for this discrepancy has not been investigated yet.

parametrisation of the crystals' energy resolution by a square-root dependence[8], $\Delta E(E) = p_0 \times \sqrt{E} + p_1$, similar to the formula in [75]. This resolution parametrisation was used for the simulation of the efficiency of the XB, which is outlined in the next section, chapter 4.5.1.2.

4.5.1.2 Efficiency

In order to be able to simulate the experimental response at a later stage of the analysis, the Crystal Ball γ-photo-peak efficiency for the 898 keV and 1836 keV lines from the β^+-decay of ^{88}Y was determined using a coincidence technique. This was done using experimental data and data from a Geant3 simulation[9], in order to be able to compare both.
The experimental data is the one described earlier for the energy calibration (chapter 4.5.1.1), *i.e.*, the source placed in the empty-target position in the centre of the XB, though only the ^{88}Y part of the data is used here. The simulation aims at mimicking the experimental conditions as well as possible. The geometry is shown in figure 4.11: The Al-canned NaI crystals of the XB as such are considered, as well as the vacuum chamber and certain parts of the interior mechanical support. Only minor components are missing in the simulation

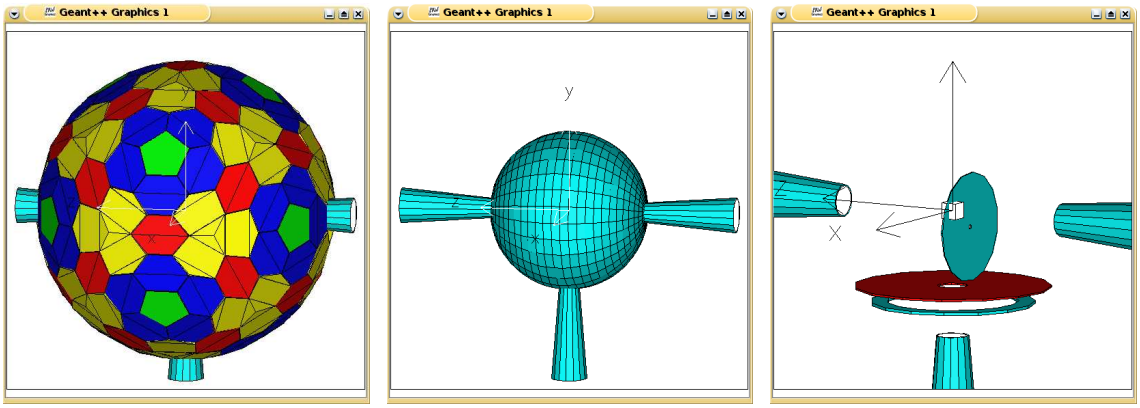

(a) Geant3: Crystal Ball. (b) Geant3: Target Chamber. (c) Geant3: Chamber Interior.

Figure 4.11: The virtual setup in the Geant3 simulation. (a) The XB; the crystals are put together from subunits. Different crystal types are indicated by different colours (A - green, B - blue, C - yellow, D - red). (b) Beam pipe parts and the target chamber shell (thickness 2.5 mm, made from aluminium (turquoise)). (c) Inside the chamber. Support ring (Al - turquoise) and plate (3 mm copper - red) for the target setup and the target wheel (Al) are included. The target wheel motor and everything related to the SSTs had not been implemented yet.

model of the setup (around the target), as presented in figure 4.11. Those are the motor and support structure for the target wheel, and all parts, structures and cables related to the SST detectors.

[8] The energy resolution of scintillators read out by PMTs is governed by photon statistics in the PMT cathode.

[9] The simulation presented here is based on the code written by R. Reifarth and co-workers.

As an output of the simulation, a data set that is directly comparable to experiment is produced. To model the crystal response more realistically, their energy resolution as obtained from the widths of measured gamma peaks (figure 4.10b) is taken into account.
The principle for the efficiency-calculation is based on the fact that the aforementioned two γ-rays from the ^{88}Y always appear in a cascade[10], *i.e.*, in coincidence. In order to compare, the following algorithm has been applied to both experimental and simulated data, event-by-event:

1. Look for a full-energy γ_1 (or γ_2) in any crystal. If more than one line of a type is found, the complete event is discarded, in order to exclude random coincidences. The total number of events with one initial γ_1 (γ_2) is counted for later normalisation.
2. Search the remaining crystals to find the coincident γ_2 (γ_1) of the cascade.
3. If a full-energy γ_2 (γ_1) is found in a crystal, a count is registered for that crystal.
4. The number of found coincident γ_2 (γ_1) photons for each crystal is divided (normalised) by the total number of initial γ_1 (γ_2) photons found.
5. Finally, the normalised number of coincident counts for each crystal is scaled by the ratio of 4π to its solid angle, *i.e.*, by 162. Thus, each crystal's intrinsic rather than total efficiency is obtained.

Such, for each crystal, the intrinsic photopeak efficiency $\epsilon_{int} = \epsilon_{total}/\epsilon_{geom}$ at the energies of 1836 keV and 898 keV is deduced. The geometric efficiency, here, is the ratio of a crystal's solid angle to the total solid angle ($\epsilon_{geom} = \frac{4\pi}{162}/4\pi = 1/162$). The results are shown in figure 4.12. In the top row the simulated and measured photopeak efficiencies are compared within the same histogram. Common to the detection of either photon energy is, that the experimental values under-reproduce the simulation. Common is also, that for certain of the lower crystal numbers (like ∼7, ∼20, ∼35, ∼55) this discrepancy is especially large. This is understandable by the fact that certain parts of the internal target chamber material had not yet been included in the simulation, especially the target-wheel motor block and its support, at the corresponding solid angles. Besides that, an agreement in the general pattern between experiment and simulation is observed, which is due to the inclusion of certain passive elements into the simulation, like the target wheel itself, and the support plate and ring.
For the 898 keV γ-rays, an approximated average of 40 % of intrinsic photo-peak efficiency has been measured, whereas around 55 % is seen in the simulation. In the case of the 1836 keV photons, about 40 % efficiency is simulated, in contrast to 25 % from experimental observation.
The bottom row of figure 4.12 highlights the simulation-experiment difference for the two photon energies. Here, the ratios of experimentally observed and simulated efficiencies are

[10] That statement is true in only 94.4 % of the cases. Here, ^{88}Y decays into the second excited state of ^{88}Sr, leading to a coincident cascade of the 898 keV (γ_1) transition from the second to first excited state followed by the first excited to ground state transition of 1836 keV (γ_2). For the remaining 5.5 % probability, the decay goes directly into the first excited state yielding yet only the latter γ_2. That means, an observed γ_1 will always imply a coincident γ_2, whereas an observed γ_2 implies a coincident γ_1 only in 94.4 % of the cases.

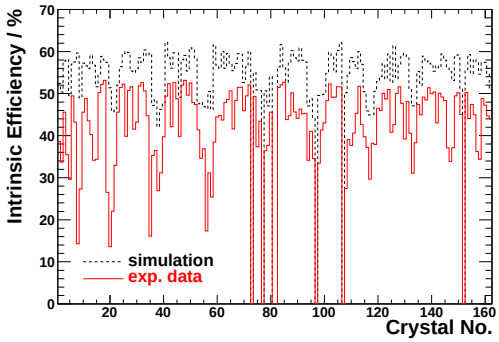

(a) 898 keV photo-peak efficiency.

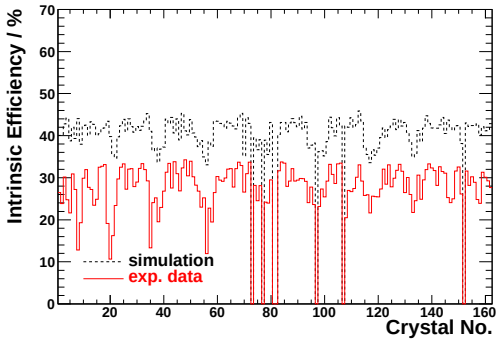

(b) 1836 keV photo-peak efficiency.

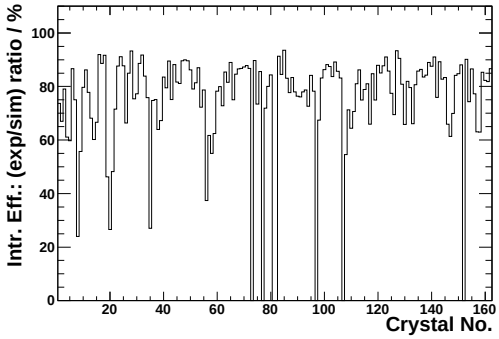

(c) 898 keV: exp/sim ratio.

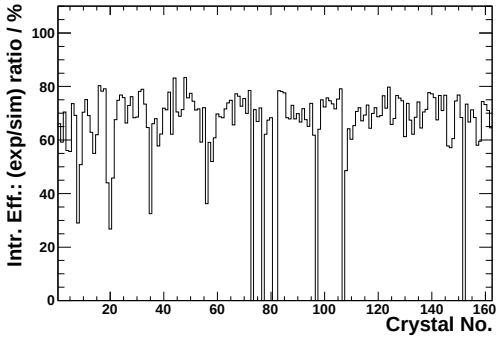

(d) 1836 keV: exp/sim ratio.

Figure 4.12: Photo-peak efficiency of the Crystal Ball for γ-rays. On the abscissa of each plot is the crystal number. Top row: Plotted on the ordinate is the photopeak efficiency of detecting one of the two ^{88}Y-decay photons in a specific crystal, in coincidence with the other photon in any other crystal. Simulated data (black, dashed line) is compared to experiment (red, full line), for the 898 keV (a) and the 1836 keV (b) γ-ray, respectively. Bottom row: The ratio of the experimental to the simulated efficiency is shown, for 898 keV (c), and 1836 keV (d).

compared between 898 keV (left) and 1836 keV (right). They are different: around 80 % to around 70 %, respectively. The simulation overshoots experimental reality, and worse, this effect seems to be energy-dependent. What could be the reasons for these discrepancies? A couple of possible sources are listed here:

- Not all the existing dead geometry had been (correctly) integrated into the simulation yet. Doing so could decrease the too high expectations.
- The simulation does not reproduce correctly the shape of the spectra (width, peak-to-Compton), so simply more simulated than experimental events fall into the photopeak region.
- Experimentally, higher energies had a lower chance of being registered fully, due to a jittering and/or too short QDC gate.

To summarise this section, the efficiency calibration for the XB for the presented experiment is not entirely finished within this thesis, and a few open questions remain; in particular the ratio of efficiencies discussed above. However, this simulation has just been a first step. Meanwhile, the presented geometry package has been integrated into a much larger and detailed simulation calculation called R3BRoot, based on FAIRRoot [63]. The name indicates that this framework will be the basis for simulations of the entire R^{3}B/LAND, and also the future R^{3}B setup at FAIR.

4.5.1.3 Time

The timing from the gamma detector can be helpful to clean up the XB data by requiring that any measured energy has been recorded within a reasonable time frame relative to an incoming beam ion triggering the POS start detector. Any sort of delayed (or advanced) photons or neutrons from a possibly activated target or from nuclear reactions in it due to interaction with the beam, or even random coincidences with cosmic particles (muons) can be rejected using the XB time information.
Employing the gamma2 programme of land02, the relative time offsets of all crystal channels versus each other have been determined, using coincident-cascade data from the ^{88}Y γ-source. As a result, the XB detector has been internally synchronised, and it needs just an additional global time offset to connect it to the rest of the setup.

4.5.2 Crystal Ball Proton Readout

As described earlier in chapter 3.2.3.3, the additional proton readout of the Crystal Ball applies to 64 crystals with the main purpose of measuring the energy of protons from (p,2p) reactions. An ideal calibration of this readout would require proton beams with various energies between 10 MeV and 500 MeV. Instead, a different approach war pursued, based on γ-rays from calibration sources and cosmic muons.

The proton readout is bypassing the last dynode of the PMT and the pre-amplifier, and therefore its amplification (or gain G in terms of QDC channels per unit energy) is lower than the one of the gamma readout[11], but still linearly for each crystal channel, indexed by the label i:

$$G_p(i) \quad = \quad G_\gamma(i) \times m_{p\gamma}(i). \tag{4.8}$$

Here, $G_\gamma(i)$ stands for the gain factor (in keV/ch) of the gamma readout (chapter 4.5.1.1), $G_p(i)$ for the gain factor of the proton readout to be determined, and $m_{p\gamma}(i)$ means the (assumed) proportionality factor between the readouts. As it is not trivial to produce photons of well-defined and high energies ($\sim$10–500 MeV), the two readouts were calibrated using 'cosmic muons'[12] instead. Those muons, when reaching the Earth's surface, have a relatively broad angular and energy distribution, peaking around vertical angles and $\sim 1-2$ GeV. Depending on their direction, there is a continuous energy-loss spectrum ($\sim$5 MeV/cm) in the XB crystals (see, *e.g.*, [76, 77]). In the following figure 4.13 such

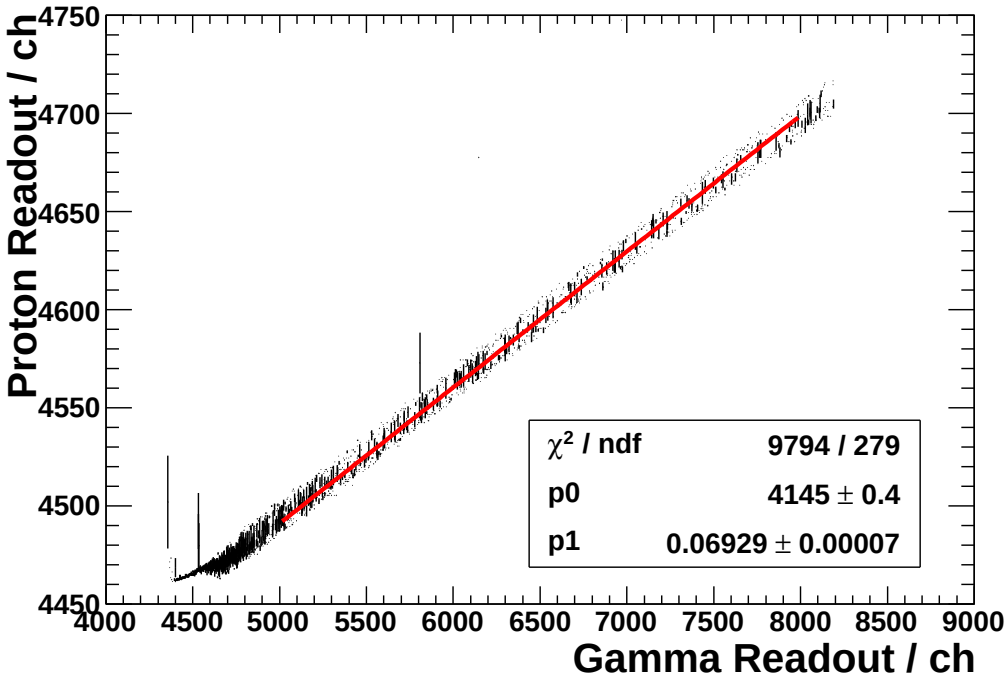

Figure 4.13: Cosmic muons seen parallelly in both XB energy readouts, here crystal # 61 as an example. The y axis hosts the raw QDC channels of the proton readout, the x axis those of the gamma readout. A linear fit to the data (red, solid line) reveals a slope of 0.069, which is equivalent to a 1/14.5 lower gain of the proton readout for this crystal.

cosmic events are shown as seen by one readout versus the other. The events of muons traversing the XB and leaving some fraction of their energy to a good approximation lie on a straight line. These profiles are fitted and their slope is identified as being the relative gain factor between the two readouts, $m_{p\gamma}(i)$. Typical values for this proportionality factor are $\sim$1/15, *i.e.*, the gain of the new readout is about 15 times smaller.
In principle, the procedure described until here is sufficient as an energy calibration of the new readout. However, the uncertainty might be very large, as the only reliable part of the calibration has been performed within the very narrow range of 0-2 MeV (*via* γ-sources with the other readout), and from there an extrapolation to $\sim$100 times higher energies is done.

An additional approach was pursued, based on ideas of R. Reifarth and H. Johansson, again using cosmic muons. The idea is to select muons that traverse the Crystal Ball centrally. Only two opposing crystals are hit, and a muon travels approximately along the full 20 cm of length of a crystal, having a relatively well-defined energy loss that can also be compared to a simulation[13]. Using the gamma2 programme of land02, events were selected which fulfill the condition that two approximately opposing crystals were hit and their neighbours did

[11] This leads to the desired higher energy range, as protons up to $\sim$ 500 MeV are supposed to be measured.
[12] That is, muons in showers produced by high-energy cosmic particles hitting the Earth's atmosphere.
[13] That refers to the Geant3 simulation already presented earlier.

not register anything. Those events are displayed in figure 4.14a, which plots on the x axis the crystal number, and on the y axis the measured muons' energy loss, as calibrated with the method described above. The intensity in z direction is indicated by a heat map. It is apparent that the energy calibration (or better: the gain matching) for the proton readout so far can be improved. In a projection to the energy axis for each crystal, this translates into a intensity-vs-energy distribution which shows a Gaussian-like peak, corresponding to the average energy loss of a minimum-ionising muon traversing a crystal more or less along its long axis. This distribution is fitted, and the value matched to the value of ∼92 MeV that results from the simulation. Accordingly, an additional factor, $m'_p(i)$, for the energy matching is defined and applied, extending[14] equation 4.8:

$$G_p(i) \quad = \quad G_\gamma(i) \times m_{p\gamma}(i) \times m'_p(i). \tag{4.9}$$

Finally, figure 4.14b shows the result of that extra matching. For convenience, this gain

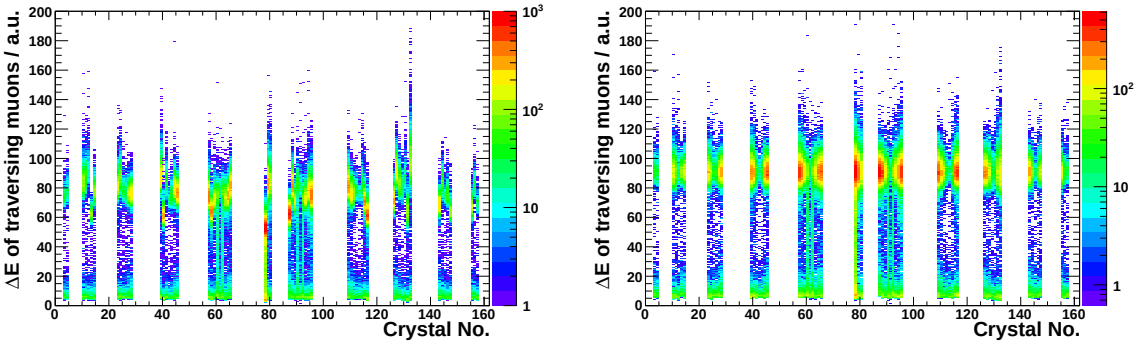

(a) Before: gain-matching using arbitrary muons.

(b) After: final gain-match using selected muons.

Figure 4.14: An approach to better gain match the crystals' novel proton readout of the XB. (a) before, (b) after matching to the traversing-muon energy loss. The x axis of the plots features the crystal number, the y axis is the energy axis, initially based on MeV, but counted in arbitrary units because it is referring to proton rather than to gamma energy.

matching has been used in order to label measured proton energy loss in MeV. This hits the right order of magnitude, but is in principle not correct: First of all, the assumption of linearity for such a high energy range is not necessarily valid. Quenching effects in the light yield or the electronic response might play a role. The final step of calibration has been obtained by muon data; the light yield per unit energy loss of muons is different than the one for photons and definitely also than the one for protons (which also undergo nuclear scattering and energy loss). And secondly, the model assumed for the simulation might be too simple. It has been assumed that the energy loss for centrally traversing muons is the same for each crystal, regardless of which zenith angle it might be pointing to. Figure 4.14 shows, that the intensity of muons is strongly dependent on that angle, but also the energy spectrum is angle-dependent (see again [76,77]), which as just presented might have caused a systematic gain mis-match. In principle, for a reliable simulation also the surrounding

[14] Of course, the two matching steps could be merged in future by omitting the intermediate proton vs gamma signal fit.

heavy material that would shield cosmic muons should be taken into account, like the concrete ceiling, the steel ALADIN magnet, and the steel of the XB support structure.
For the moment, the shown gain matching is as good as it gets. However, as already emphasised at the end of the previous chapter 4.5.1.2, with a full and realistic simulation framework such as the emerging R3BRoot, and together with a realistic event generator, it seems promising that muons can be used for a good and reliable gain matching of the whole XB detector.

4.6 Hit Reconstruction with the Crystal Ball

In the case of quasi-free-scattering reactions, for example, high-energy protons and γ-rays from excited states may be coinciding, and registered in the Crystal Ball simultaneously. This section describes the algorithm that was chosen in order to disentangle the XB data in terms of so-called γ and proton clusters, that is, groups of neighbouring crystals which are identified as belonging to the same incident photon or proton.

4.6.1 Addback Algorithm for Proton and Gamma Clusters

For each event of SYNC level data, a Crystal Ball multiplicity XBmul is defined that indicates how many crystals have registered something, *i.e.*, a non-zero entry for either time (Xbt), gamma-energy (Xbe), and/or proton energy (Xbpe)[15]. The algorithm runs over that multiplicity and defines proton-cluster and gamma-cluster hits in the following manner:

1. All crystals with either Xbpe or Xbe greater than zero are put into a list and sorted by their gamma energy, largest first. If Xbe is in overflow, Xbpe is used for further sorting instead.

2. Perform an addback: Loop over the list of energy-sorted crystals, and decide whether the hit stems possibly from a proton or a gamma.
   - A proton hit is defined by an overflow in the gamma readout and a greater-than-zero entry in the proton readout.
   - A gamma hit is defined by a greater-than-zero but finite value in the gamma readout.
   For all remaining crystals in the list, it is checked whether they are neighbours of the currently first crystal in the list. If so, their energy is added to that first one, and they are removed from the initial list.
   As soon as a cluster is complete, it is filled into a corresponding gamma or proton list. As a result, only the numbers of crystals which are centres of clusters are retained for further analysis.

3. A Doppler correction is performed for the list of gamma clusters, as described in chapter 4.6.1.1.

[15]Reminder: The latter Xbpe exists only for the forward 64 crystals.

The result of the addback procedure is a list of proton clusters and a list of (Doppler-corrected) gamma clusters, for each event. With those lists, a corresponding proton- or gamma-cluster multiplicity is defined, which may be used to characterise certain reaction channels, like for example (p,2p) as shown later in chapter 6.1.1.
The procedure described above is not necessarily the best-possible addback procedure, but rather intuitive. Whether clusters of crystals are all contained within one ring of next neighbours around an initially hit central crystal — and whether that crystal always shows the highest energy deposit – has not been investigated here. Simulations based on R3BRoot and the QFS event-generator by L. Chulkov [78] are indicating that this is not always the case [79]. The following section outlines the procedure of Doppler correction.

4.6.1.1 Doppler Correction for Gamma Rays

One of the observables necessary for reconstructing the excitation energy of a reaction is the energy of the coincident gamma rays, in the frame of the de-exciting fragment, let's say, from ^{15}O*. After distilling the list of gamma clusters as described in chapter 4.6.1, those gamma energies need to be corrected for the relativistic Doppler shift which is associated with being emitted from the reference frame in the fragment's centre-of-mass (c.m.), at motion relative to the laboratory frame (lab) where they are detected. The well-known Doppler-shift formula is applied to each of the identified gamma clusters, relating the γ-energy ($E_{\mathrm{c.m.}}$) emitted in the frame moving with the fragment to the one (E_{lab}) measured in the resting lab frame:

$$E_{\mathrm{c.m.}} = E_{\mathrm{lab}} \times \gamma_{\mathrm{fr}} \left(1 - \beta_{\mathrm{fr}} \times \cos\left(\vartheta_{\mathrm{fr-det}}\right)\right). \tag{4.10}$$

Here, β_{fr} means the velocity (in units of c) of the de-exciting fragment, and $\vartheta_{fr-\mathrm{det}}$ is the polar angle in the lab system between the flight direction of the fragment and the central crystal of the cluster. The detection angle $\vartheta_{\mathrm{fr-det}}$ may be approximated by the mere detector angle relative to the z coordinate axis, because it is very large (5–175 °) compared to the fragment scattering angle (∼10 mrad). Furthermore, the large opening angle of the detecting crystals with about 15 ° creates a totally dominating Doppler broadening, swallowing the effect of small angle deviations[16]. Accordingly, the formula for the fragment's c.m.-frame gamma energy is simplified to:

$$E_{\mathrm{c.m.}} = E_{\mathrm{lab}} \times \gamma_{\mathrm{fr}} \left(1 - \beta_{\mathrm{fr}} \times \cos\left(\vartheta_{\mathrm{det}}\right)\right). \tag{4.11}$$

For the polar detection angle ϑ_{det} of a crystal, its average value, *i.e.*, the centroid of the corresponding crystal face pointing towards the radiation source, is used.
For the analysis presented within the upcoming chapters of this thesis, the γ-data from the Crystal Ball is not used yet. That is, no corresponding trigger has been used, nor has the γ-ray energy been used for gating on excited fragment channels (of the ^{15}O) yet. Neither for invariant-mass reconstruction, as that also would require a simulation taking into account the XB's γ-efficiency in the presence of proton hits. Such a development is still to be addressed.
Nevertheless, at this point a demonstration of the functionality of the presented γ-ray

[16] Any recoil to the fragment when emitting the γ-rays is neglected, too.

algorithm shall be offered, as a teaser. Figure 4.15 shows the photon-sum-energy spectrum measured with the XB in coincidence with ^{15}O fragments stemming from ^{17}Ne breakup on the CH_2 target, in coincidence with the XB Sum trigger (Tbit8), *i.e.*, presumably from a (p,2p) proton knockout into the XB. Tentatively, the bumps in figure 4.15 are identified as

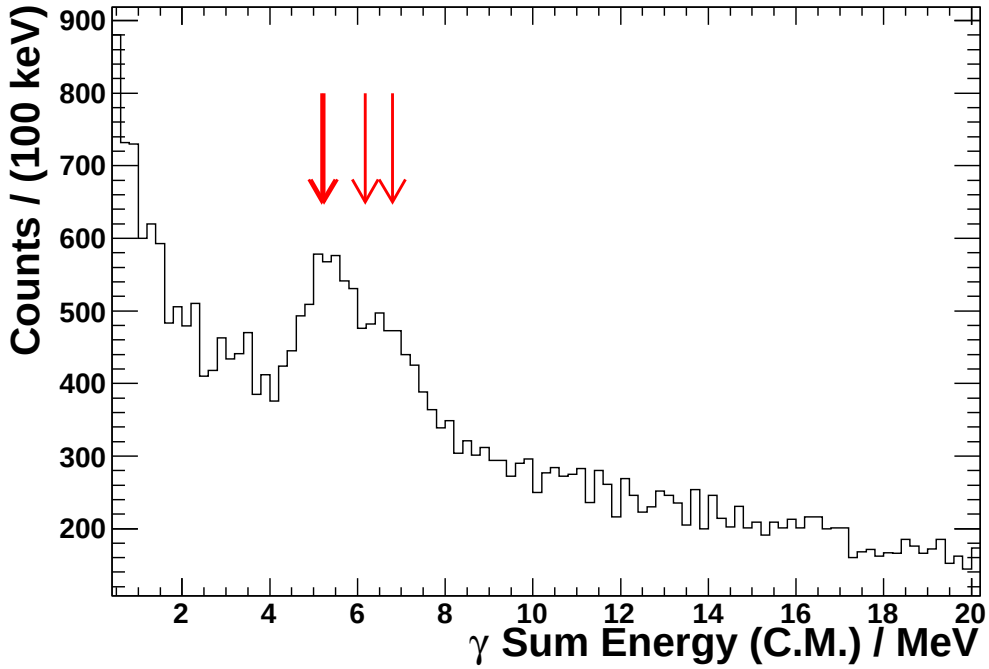

Figure 4.15: The sum-energy spectrum of γ-rays (clusters) in coincidence with ^{15}O broken up from ^{17}Ne on the CH_2 target, in coincidence with the XB Sum trigger. The arrows indicate the position of the first four excited states in ^{15}O, at 5.183 MeV, 5.2409 MeV, 6.1763 MeV, and 6.793 MeV.

the $J^\pi = \frac{1}{2}^+$ state at 5.183 MeV and/or the $J^\pi = \frac{5}{2}^+$ state at 5.2409 MeV, plus the $J^\pi = \frac{3}{2}^-$ state at 6.1763 MeV, and the $J^\pi = \frac{3}{2}^+$ at 6.793 MeV.

5

Analysis Techniques

The calibrated data needs to be processed further, in order to obtain physics results. This chapter aims to provide an overview of the most important analysis techniques necessary for the present work.

5.1 Reaction Cross Sections

Reaction cross sections are observables in nuclear-physics experiments, which — in conjunction with a corresponding theoretical model — yield information about, *e.g.*, the size of a nucleus. In the case of one-nucleon-removal reactions, from partial cross sections the so-called spectroscopic factors of the configurations of the removed nucleons within the nucleus may be deduced using, *e.g.*, a Glauber-type reaction model.
Considering the case of the Borromean character of ^{17}Ne, the cross sections for reactions of the type $^{17}\mathrm{Ne} \xrightarrow{Target} {}^{15}\mathrm{O} + X$, *i.e.*, two-proton-removal reactions, are of special interest. There are several channels contributing to the two-proton removal from ^{17}Ne; the dominant ones are listed here:

- Electromagnetic dissociation, or in more colloquial terms, Coulomb breakup: When passing a target nucleus at non-touching distance, the projectile still is object to their mutual electromagnetic interaction (repulsion), which can be considered to be communicated *via* virtual photons. This process is of great relevance for high-Z targets (Pb, Au, Bi, U); at high projectile velocity ($\sim$0.75 c) the electromagnetic interaction can lead to high excitations up to $\sim$20 MeV, certainly above the one-nucleon threshold for most nuclei. ^{17}Ne is only bound by 950 keV, and consecutively will forward-evaporate[1] its two valence protons: $^{17}\mathrm{Ne} \xrightarrow{Pb/\gamma} {}^{15}\mathrm{O} + 2p$

- Inelastic scattering, or diffractive dissociation: This channel competes with Coulomb breakup, and it cannot be easily distinguished from it. Projectile-like ^{15}O and two protons are emitted at forward angles in the laboratory:
  $^{17}\mathrm{Ne} \xrightarrow{CH_2,C,(Pb)} {}^{15}\mathrm{O} + 2p$

- One-proton knockout: One of the two valence protons (or one of the core protons) undergoes a very high momentum transfer by a direct billiard-like interaction with the target. It is scattered to large angles and can be detected in the Crystal Ball. The remaining projectile-like ^{16}F is unbound and decays immediately. An ^{15}O fragment and one proton are emitted at forward angles:
  $^{17}\mathrm{Ne} \xrightarrow{CH_2,C,(Pb)} {}^{16}\mathrm{F} \rightarrow {}^{15}\mathrm{O} + p$

[1] In the ^{17}Ne rest frame, the emission is in principle isotropic within 4π. The relativistic beam velocity translates into a forward focusing in the laboratory frame.

- Two-proton knockout: Though improbable, if the two halo protons show a strong spatial correlation, they might be knocked out simultaneously as a pair. Only the ^{15}O is leaving the target at forward angles:
  $^{17}\mathrm{Ne} \xrightarrow{CH_2,C,(Pb)} {}^{15}\mathrm{O}$

This thesis concentrates on the nuclear-breakup channels, in particular on the one-proton-removal channels (diffraction and knockout). For the determination of cross sections, data with just a condition on detecting ^{15}O in the final channel will be used. In other words, forward protons will be treated inclusively.

5.1.1 Formalism and Approximations

For the discussed inclusive reactions of the type $A \rightarrow B + X$, in our case $^{17}\mathrm{Ne} \xrightarrow{CH_2,C} {}^{15}\mathrm{O} + X$, the cross section σ can be defined as follows:

$$\sigma = \frac{1}{\tau} \times P \tag{5.1}$$

$$\tau = \frac{\rho \times d}{M} \tag{5.2}$$

In the above equations, P indicates the probability for a reaction to happen within the target (that is, any reaction that leads to ^{15}O). τ is called the target parameter, and it denominates the number of scattering centres per unit area; connected to this, ρ, d, and M abbreviate the target's mass density, its thickness, and the mass of one of the considered scattering centres, respectively. For the carbon target, simply the carbon nuclei are considered as scattering centres. For the CH_2 target, CH_2 molecules are defined as the reaction centres. The target parameter is given by design and fabrication of the target.
The reaction probability P is the experimental observable of interest. It is defined as the number of reaction events B (the number of produced ^{15}O fragments, counted directly after leaving the target) divided by the number of repetitions of the reaction attempt, *i.e.*, the number of incoming ^{17}Ne ions A_0. This number is approximated by A, the number non-reacting ions exiting the target. Both numbers are further approximated by the number of reacted (b) and non-reacted (a) ions that are counted at the end of the fragment arm using the NTF[2]:

$$P(A_0 \rightarrow B) = \frac{B}{A_0} \approx \frac{B}{A} \approx \frac{b}{a} \tag{5.3}$$

The reasoning behind this approach is the following. In the target, the incoming particles have the possibility to undergo a huge variety of reactions in the sense laid out above, meaning reactions of the type $A_0 \rightarrow A, B, C, D...$, with A and B being the unreacted and reacted channels already mentioned, and $C, D, ..$ being other breakup channels. The target is relatively thin, and the beam has a very high velocity ($\beta \sim 0.75$), so that the probability to react at all is low, in the order of 10^{-2} to 10^{-3}. This is why $A \approx A_0$ is a valid approximation.

[2]Counting with the NTF means counting events in coincidence with the fragment trigger, *i.e.*, with Tbit2.

The second approximation, $B/A \approx b/a$, is a bit more difficult to justify. Obviously, the number of unreacted ions a as registered after $\sim 10\,\mathrm{m}$ of flight path, through detectors, foils, and air, has to be different than the undetected number of ions originally emerging from the target A — simply due to loss from scattering and reactions on that way. The same argument holds true for b and B. The assumption is that those mentioned loss fractions for both, ions of type A and B, are identical, or at least similar enough. What supports that statement, is that the detection efficiencies are the same, that the acceptance is similar, and that the cross sections for further loss reactions with all the material are similar enough, for both reacted and unreacted beam particles. Certainly, the last statement seems a bit weak for the cases of ^{17}Ne and ^{15}O, since they have different sizes. However, this is the approach chosen here for practical reasons.

5.1.2 Background Subtraction

In order to determine the background to the reacted channel from reactions after the target, measurements with the ^{17}Ne beam without any target are performed. This 'missing' target for convenience is also called 'empty' target. In order to determine the reaction cross section from only the actual (CH_2 or C) target, (T), the normalised[3] empty target, (ET), contribution has to be subtracted. This is done under the assumption that the acceptance is the same with and without target.

$$\sigma_T = \frac{1}{\tau_T} \times (P_T - P_{ET})\,. \tag{5.4}$$

Such a subtraction is done on the level of reaction probability as formulated in equation 5.3. Of particular interest is the contribution of projectiles interacting with the protons in the CH_2 target, as they induce quasi-free-scattering reactions. The carbon background has to be subtracted from the CH_2 target measurement *via* a normalised carbon-target measurement:

$$\sigma_{proton} = \frac{1}{2} \times \sigma_{H_2}, \tag{5.5}$$

$$\sigma_{H_2} = \frac{1}{\tau_{CH_2}} \times (P_{CH_2} - P_{ET}) - \frac{1}{\tau_C} \times (P_C - P_{ET})\,, \tag{5.6}$$

$$\sigma_{H_2} = \frac{1}{\tau_{CH_2}} \times P_{CH_2} - \frac{1}{\tau_C} \times P_C - \left(\frac{1}{\tau_{CH_2}} - \frac{1}{\tau_C}\right) \times P_{ET} \tag{5.7}$$

The formulation of equation 5.7 points out, that by choosing the target parameters of the CH_2 and the C target identical (*i.e.*, same number of CH_2 and C per unit area), any further explicit subtraction of the ET measurement is not needed, as it is done intrinsically in the right proportions already by the carbon-target subtraction.

5.1.3 Fragment-Mass Cut

The previous chapter 4 describes the selection of oxygen fragments, not specifically the one of ^{15}O. For the purpose of determining the inclusive two-proton-removal cross section from ^{15}O, the oxygen mass is identified *via* the deflection angle of the beam after the ALADIN magnet using the two GFI fibre detectors. The events shown in figure 5.1 are ion hits in the

[3] Normalisation is done with respect to the number of non-reacted ($\approx$ incoming) particles.

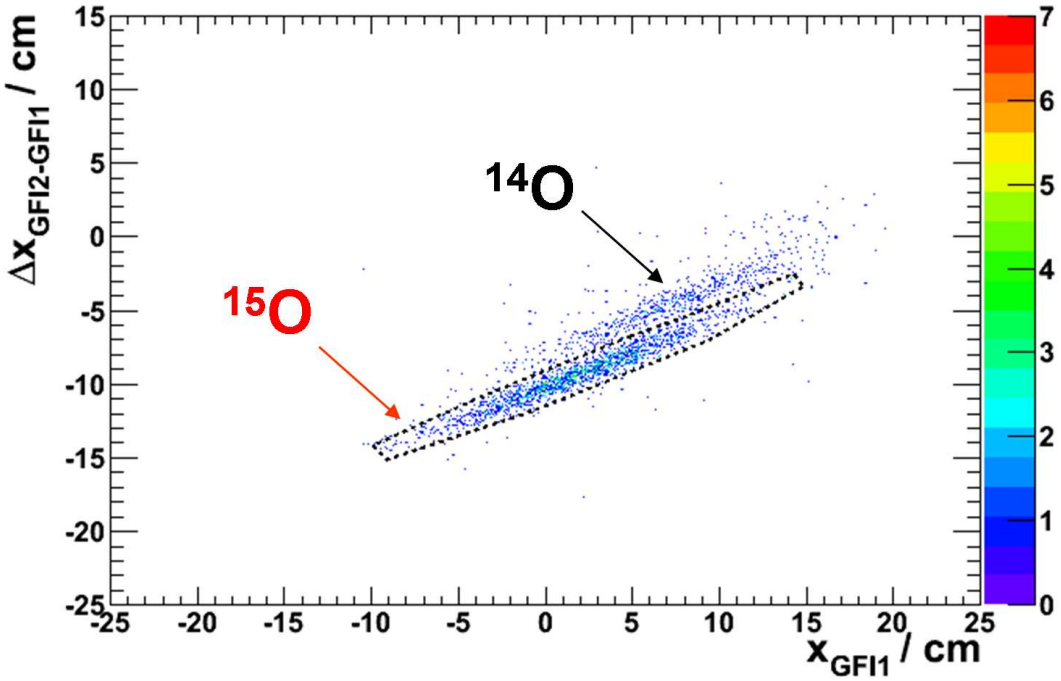

Figure 5.1: Mass identification of oxygen fragments using the GFI detectors (cross-checked with the tracker programme, chapter 5.2). Shown are events being identified as incoming ^{17}Ne and outgoing oxygen (by NTF and the SSTs). Plotted on the y axis is the (GFI2-GFI1) difference of the x coordinates of the ions' trajectory through the GFIs vs. the x coordinate of the GFI1 detector alone on the x axis. The y axis quantity is scaling with the deflection angle in the magnetic field, and is a measure for the magnetic rigidity of the beam. The events in the region enclosed by the black dashed line are identified as ^{15}O. The second, less intense locus is taken to be ^{14}O. Here, ions are bent more strongly (higher x values) in the ALADIN magnetic field. Further species, like ^{13}O, may also be present, but cannot clearly be identified here.

GFI detectors with incoming ^{17}Ne and outgoing oxygen. The selection of ^{15}O events by the graphical cut is based on the following ideas[4]. Recalling equation 3.1, the magnetic rigidity is proportional to the mass-over-charge ratio and a function of velocity. In the reactions mentioned above, the velocity of the final-state fragment stays in good approximation the same as the beam velocity. That means, that also different isotopes share the same velocity, and so their A/Z ratio will determine their magnetic rigidity. As the magnetic field is constant, different isotopes are simply bent on trajectories of different curvature[5], *i.e.*, to a different bending angle. In figure 5.1, ^{15}O form the more intense locus and, compared to ^{14}O, are located along (in average) smaller bending angles. Correspondingly, they are hitting the GFIs more to the left (lower x coordinates). For the purpose of determining cross sections, the efficiency and acceptance of the ^{15}O selection is set to unity, for simplicity.

[4]The selection procedure has been verified by a cross-check with the tracker programme.
[5]A larger A/Z leads to larger radius which means a smaller bending angle.

5.2 Tracking: Fragments and Protons

For a part of the analysis performed within the framework of this thesis, a particle-tracking programme has been used which was and is being developed by Ralf Plag for the R^{3}B/LAND collaboration [73].
Given the necessary experimental input[6], it reconstructs trajectories of heavy fragments and protons through the magnetic field of ALADIN (see chapter 3.2.2) towards the NTF and TFW ToF-walls for the purpose of determining:

- Mass, velocity and 3-momentum of the fragment,
- Velocities and 3-momenta of the protons.

The fragment mass is predominantly reflected in the radius of its trajectory through the ALADIN magnet, to be determined by the tracking programme. In contrast to the tracking approach with a reference-beam trajectory, as used for various experiments before (*e.g.*, [29, 53, 71]), R. Plag's code (the tracker) follows a backward-tracking approach based on absolute detector positions and magnetic-field values, which shall briefly be described here. Using the x (*i.e.*, dispersive-plane) hit positions in the GFIs and the y hit position in the NTF, the fragment with selected and known charge is injected backwards into the ALADIN magnet. Its field $\vec{B}(\vec{r}, I)$ had been measured [47] and parametrised into of a discrete field map, which can be interpolated spatially ($\vec{r}$) and according to the current I that was applied at a particular time in the experiment. The fragment trajectory is determined in a variational approach:

1. Starting parameters for the track are chosen: The GFI x positions are taken as fixed, the NTF y position is used for a starting value in Δy, and furthermore the fragment mass A and its speed β are assigned an initial value.
2. The trajectory through ALADIN is calculated, and the x and y offsets in the SSTs are determined.
3. Depending on the SST x offset, A is varied. Depending on the y offset, the y direction of the track, Δy, is varied.
4. Again, the track through ALADIN, and the SST offsets are calculated.
5. The tracked and the measured ToF are compared, and β is varied in order to match the tracked to the measured value. A is also varied in order to compensate and leave the beam's $B\rho$, and thus its deflection in ALADIN, constant.
6. Repeat steps 2 to 4, if the SST offsets are still larger than desired.

Similarly, the tracker is capable of back-tracking the protons measured by the proton-arm detectors (chapter 3.2.2) and in particular by the high-resolution PDCs. In contrast to the procedure of fragment tracking, the proton's velocity β and its y direction are being varied

[6] That is, absolute detector positions, magnetic field strength, and the atomic number Z of the fragments supposed to be tracked, for example.

in order to match the trajectory with the target interaction point (X0,Y0), which has been calculated by the previously determined fragment's trajectory.
Figure 5.2 (a) visualises the successful tracking of an oxygen ion and a forward proton after the reaction of an incoming ^{17}Ne with the CH_2 target, and (b) presents the oxygen-mass distribution obtained for such reactions.

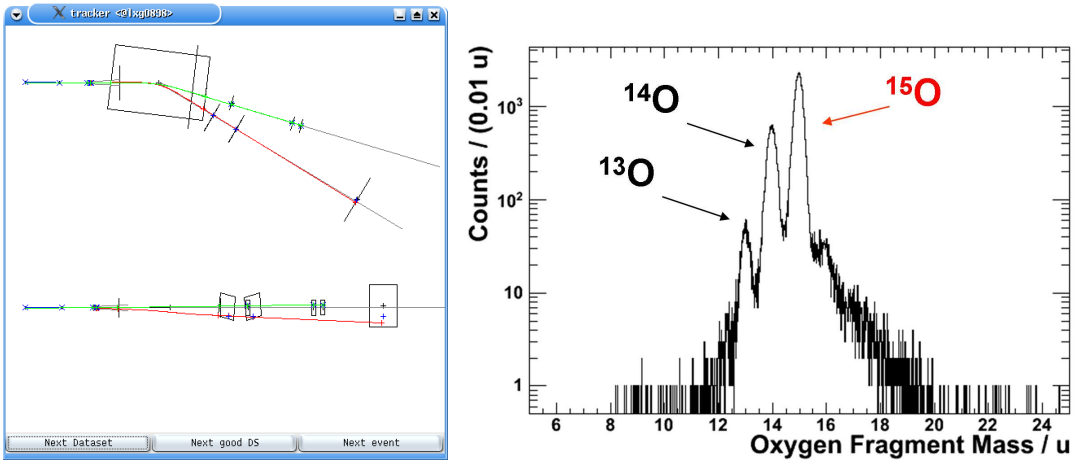

(a) Tracker GUI.

(b) Example oxygen-mass distribution.

Figure 5.2: (a) Visualisation of the reconstructed tracks of a ^{17}Ne → oxygen (green) + p (red) with the tracker. Upper part: view from top, onto the dispersive x-z plane; lower part: view from the side, onto the y-z plane. The beam enters from the left, the blue crosses indicate measured hits in the detectors. Those are the PSPs, target, the SSTs before ALADIN, the GFIs and the NTF for the fragment, and the PDCs and the TFW for the proton. (b) Mass distribution of tracked oxygen fragments from reactions of ^{17}Ne with the CH_2 target. The major isotopic contribution stems from ^{15}O, but also ^{14}O and ^{13}O are clearly identified.

5.2.1 Angle Measurement at the Target

Scattering angles are a key observable related to the transverse-momentum distribution of the reaction residues (fragment, protons), which in turn may carry information about the quantum state of the incoming-beam projectile to study. Figure 5.3 sketches the detectors and beam-line components relevant for scattering-angle measurements at the R^{3}B/LAND setup. A scattering reaction is shown, in projection to a transverse (x-z or y-z) plane. It involves an incoming-beam particle at ϑ_{in} (measured by PSP1 and PSP2, relative to the nominal beam axis), and a final-state fragment at ϑ_{out} (measured by SST3 and SST6); possible residual protons are neglected here. The scattering plane hosting the total scattering angle, ϑ_{scat}^{total}, may be arbitrarily oriented relative to the laboratory, and it is more convenient to study its projections, $\vartheta_{scat}^{x,y}$, onto the laboratory x-z and y-z planes:

$$\vartheta_{scat}^{total} = \sqrt{{\vartheta_{scat}^{x}}^2 + {\vartheta_{scat}^{y}}^2}, \tag{5.8}$$

$$\vartheta_{scat}^{x,y} = \vartheta_{out}^{x,y} - \vartheta_{in}^{x,y}. \tag{5.9}$$

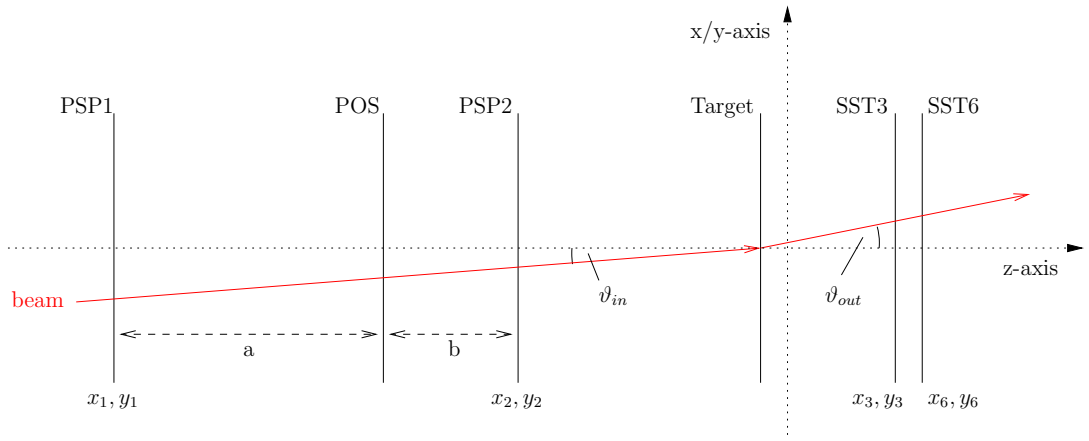

Figure 5.3: Sketch of a scattering process in the target. All components are shown in projection to the transverse plane. The position-sensitive pin diodes, PSP1 and PSP2, located at z_1 and z_2, respectively, measure the transverse beam coordinates (x_1, y_1) and (x_2, y_2). Between them, the start-trigger detector POS is placed at a distance $a : b$ between PSP1 and PSP2. After the target (which was located a bit upstream of the coordinate centre), the double-sided silicon-strip detectors, SST3 and SST6 at z_3 and z_6, measure the transverse coordinates of the outgoing fragment, (x_3, y_3) and (x_6, y_6).

The angles $\vartheta_{out}^{x,y}$ and $\vartheta_{in}^{x,y}$ are measured and calculated using the hit positions of the involved detectors.
The following parts of this section firstly are dedicated to the alignment of the detector positions relative to each other, and secondly, to discuss and identify the various sources of angular-resolution contributions in the setup.

5.2.1.1 Detector Alignment

Considering straight-line trajectories, the positions and angles of a particle can be calculated by extrapolation from anywhere else just by the measurement of hit positions in two detectors and their known positions in the setup. Referring to figure 5.3, *e.g.*, the intersection point of an ion with detector SST3 can be calculated by forward extrapolation from PSP1 and PSP2, and the obtained x- and y-coordinates $(x'_3,\ y'_3)$, compared with the measurement of SST3 $(x_3,\ y_3)$ itself:

$$x'_3 = \frac{x_2(z_3 - z_1) - x_1(z_3 - z_1)}{z_2 - z_1}, y'_3 = \frac{y_2(z_3 - z_1) - y_1(z_3 - z_1)}{z_2 - z_1}. \tag{5.10}$$

Doing this with a large sample of events, by obtaining a statistically representative distribution, the centre-of-gravity of the extrapolated−measured distribution can be identified as the detector offset $\Delta x_3 = x'_3 - x_3$. This is an additive parameter, which is used for the calculation of hit positions with that detector, *e.g.*, the x position of SST3:

$$x_3^{aligned} = x_3 + \Delta x_3. \tag{5.11}$$

Continuing this approach, the relative position of each detector with respect to the others is found within the tracking programme, and the global offset of all detectors is chosen as small as possible; *i.e.*, as close as possible to the nominal position. If, *e.g.*, the detectors SST3 and SST6 were found to require an additional relative offset along some axis, then half of that offset in opposing directions would be applied for either of them. Choosing a minimal global offset is not only practical, but it also simply presumes that the detectors have been placed according to the drawings. As a visualisation of the idea, figure 5.4 shows hit distributions of ^{17}Ne ions in SST3 and SST6 with the empty target, after alignment of the whole set of PSPs and SSTs. The columns of figure 5.4 show SST3x, SST3y, SST6x,

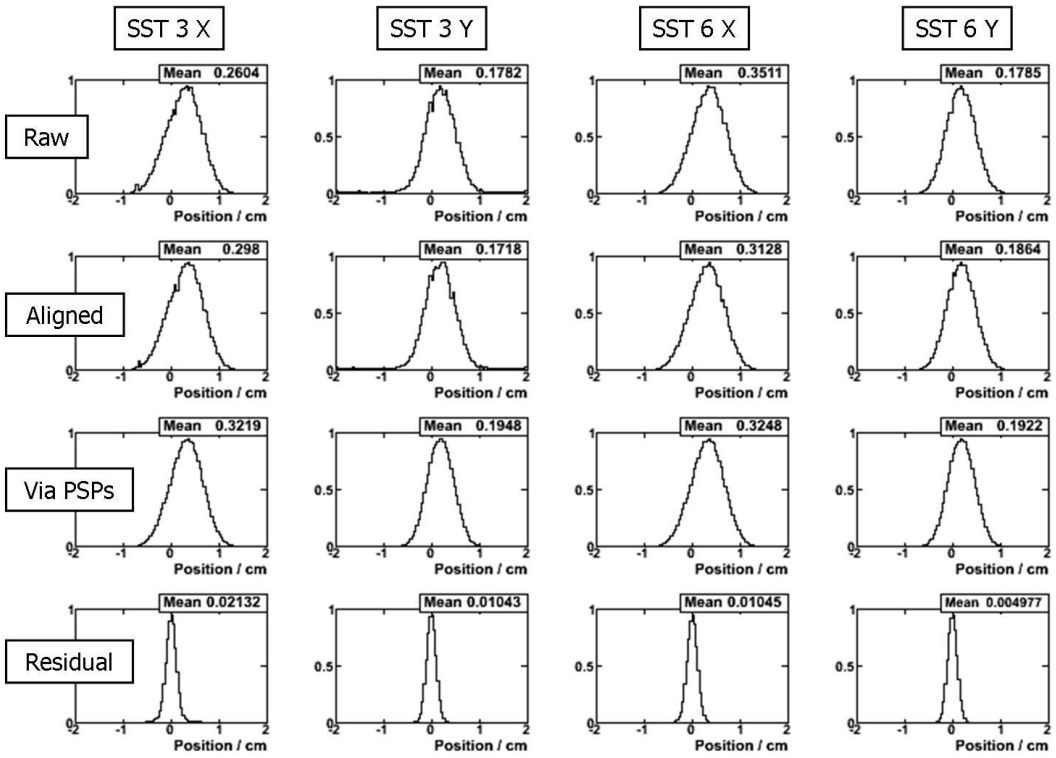

Figure 5.4: Hit distributions with aligned PSP and SST detectors for ^{17}Ne on the empty target; normalised intensity (y axes) vs position in cm (x axes). Columns show normalised SST3x, SST3y, SST6x, and SST6y distributions, respectively. The first row features default hit positions, the second one the aligned ones. The third row shows the extrapolations from the (aligned) PSPs, and the fourth one hosts the difference distributions between extrapolation and aligned measurement. The difference distributions peak at zero, nicely within the resolution, *ergo* the alignment has worked.

and SST6y, respectively. The first row contains the default hit distributions, the second row shows the aligned ones. The third row showss the hit distributions from the extrapolation of the also aligned PSPs, and the fourth one finally depicts the difference between the extrapolated and the aligned values. Clearly, they all peak at zero, within the width of the distribution, which reflects the resolution of the measurement.

5.2.1.2 Angular Resolution and Straggling

When observing breakup reactions, the question has to be addressed to which extent the studied quantities, such as scattering angles or transverse momenta, are influenced by the limited angular resolution of the measurement. To answer that question, elastic scattering $^{17}\mathrm{Ne} \rightarrow {}^{17}\mathrm{Ne}'$ reactions are to be studied; their scattering-angle distribution will peak around zero, and its Gaussian width parameter σ will reflect the statistical uncertainties caused by the detector resolution, and by the angular straggling due to multiple Coulomb scattering. Referring to figure 5.3, in the following discussion equations are written only for the x projections of the scattering process.
In order to compute the multiple-scattering component to the uncertainty in the angle determination, let's assume the following: For small angles, $\tan\vartheta = \vartheta$, and without straggling the ingredients to equation 5.9 can be written as

$$\vartheta_{in} \equiv \vartheta_{in,0} = \frac{x_2 - x_1}{z_2 - z_1}, \tag{5.12}$$

$$\vartheta_{out} \equiv \vartheta_{out,0} = \frac{x_6 - x_3}{z_6 - z_3}. \tag{5.13}$$

The $\vartheta_{in/out}$ denote the 'real' angles of the particle due to the elastic-scattering process, whereas the $\vartheta_{in,0/out,0}$ are the values calculated from the transverse beam coordinates x_i, measured at z positions z_i (figure 5.3). However, additional straggling occurs in all detectors and objects the beam traverses:

$$\vartheta_{in} = \vartheta_{in,0} - \frac{a}{a+b}\vartheta_{str}^{POS} - \vartheta_{str}^{PSP2}, \tag{5.14}$$

$$\vartheta_{out} = \vartheta_{out,0} - \vartheta_{str}^{Target} - \vartheta_{str}^{SST3}. \tag{5.15}$$

The true incident-beam angle ϑ_{in} is measured as $\vartheta_{in,0}$, but blurred by a fraction of the straggling in POS, $\frac{a}{a+b}\vartheta_{str}^{POS}$, and by the straggling in PSP2, ϑ_{str}^{PSP2}.
The true angle of the outgoing beam, ϑ_{out}, is modified by the straggling in the target, ϑ_{str}^{Target}, and in the upstream double-sided silicon-strip detector, ϑ_{str}^{SST3}, before it can be measured as $\vartheta_{out,0}$.
Correspondingly, the scattering angle can be expressed as

$$\vartheta_{scat} = \vartheta_{out} - \vartheta_{in} \tag{5.16}$$

$$= \vartheta_{out,0} - \vartheta_{in,0} - \vartheta_{str}^{Target} - \vartheta_{str}^{SST3} + \frac{a}{a+b}\vartheta_{str}^{POS} + \vartheta_{str}^{PSP2} \tag{5.17}$$

$$= \frac{x_6 - x_3}{z_6 - z_3} - \frac{x_2 - x_1}{z_2 - z_1} - \vartheta_{str}^{Target} - \vartheta_{str}^{SST3} + \frac{a}{a+b}\vartheta_{str}^{POS} + \vartheta_{str}^{PSP2}. \tag{5.18}$$

The quadratic width of that distribution turns out to be:

$$\sigma_{scat}^2 = \sigma_{out,0}^2 + \sigma_{in,0}^2 + \sigma_{str,Target}^2 + \sigma_{str,SST3}^2 + \frac{a^2}{(a+b)^2}\sigma_{str,POS}^2 + \sigma_{str,PSP2}^2, \tag{5.19}$$

with

$$\sigma_{in,0}^2 = 2 \times \frac{\sigma_{res,PSP}^2}{(z_2 - z_1)^2}, \tag{5.20}$$

$$\sigma_{out,0}^2 = 2 \times \frac{\sigma_{res,SST}^2}{(z_6 - z_3)^2}. \tag{5.21}$$

Here, $\sigma_{res,PSP}$, means the position resolution of either PSP1 or PSP2, $\sigma_{res,SST}$ correspondingly the one of SST3 or SST6.[7]
The derived results in terms of resolution, and the straggling contribution from target and detectors will be used for the following results in chapter 6. Before that, the invariant-mass formalism is presented.

5.3 The Invariant-Mass Technique

In order to study the excitation-energy spectrum of short-lived or even unbound nuclei, the experimental approach pursued with the R^{3}B/LAND setup is to excite these nuclei above the particle threshold, and measure the relative energy of the residual particles including potential γ-rays from excited states *via* the invariant-mass approach, which shall be presented here.
The invariant mass $\mathcal{M}$ is related to the square root of the norm of the total 4-momentum vector P^μ of a system of particles; it is, as the name suggests, a Lorentz scalar, *i.e.*, invariant with respect to Lorentz transformations between various frames of reference (like the projectile rest frame (RST) and the laboratory frame (LAB)).

$$\mathcal{M}^2 \cdot c^2 = \eta_{\mu\nu} P^\mu P^\nu = P^\mu P_\mu = \left(\frac{E}{c}\right)^2 - (p_x^2 + p_y^2 + p_z^2), \tag{5.22}$$

$$P^\mu = \left(\frac{E}{c}, \vec{p}\right), \tag{5.23}$$

$$\eta_{\mu\nu} = \mathrm{diag}(1, -1, -1, -1), \tag{5.24}$$

c is the speed of light, E the system's total energy, $\vec{p}$ its total classical 3-momentum vector, and $\eta_{\mu\nu}$ the metric tensor of Minkowski space-time.

An initial-state (index I) projectile-like nucleus, that due to a reaction with the target has been excited by an amount of energy E^*, is considered being at rest in the RST frame ($\vec{p}_I \equiv 0$, neglecting target recoil and excitation). Its invariant mass $\mathcal{M}_I$ can be written as:

$$\mathcal{M}_I = \frac{1}{c}\sqrt{\frac{E_I^2}{c^2}} = \frac{1}{c^2}\sqrt{(m_I c^2 + E^*)^2} = m_I \sqrt{\left(1 + \frac{E^*}{m_I c^2}\right)^2}. \tag{5.25}$$

As typically the excitation energy is very small compared to the projectile rest mass, $E^* \ll m_I c^2$, quadratic terms in E^* can be neglected, and additionally a Taylor expansion of the square root ($\sqrt{1+x} = 1 + \frac{1}{2}x$, if $|x| \ll 1$) can be employed, yielding:

$$\mathcal{M}_I = m_I + \frac{E^*}{c^2}. \tag{5.26}$$

Typical excitations exceed the particle threshold of the projectile, which in light exotic nuclei usually is smaller than $\sim$2 MeV. The excited projectile will evaporate particles (protons, neutrons, other light clusters) until the remaining energy falls below the particle threshold

[7] It should be noted that the resolution of the SSTs should be expected to be different in x and y, as the corresponding strip pitches, 110 μm along x and 104 μm along y, are different.

in the daughter nucleus. The remaining energy leads to emission of γ-rays until the ground state is reached. If possible, all those N final-state residues are measured in the LAB system, allowing for the reconstruction of the invariant mass $\mathcal{M}_F$ of the initial-state excited projectile *via* its final-state decay products (counted by index j):

$$\mathcal{M}_F = \frac{1}{c}\sqrt{\left(\sum_j^N \frac{E_j}{c}\right)^2 - \left(\sum_j^N \vec{p}_j\right)^2} \tag{5.27}$$

For massive particles we can express energy and 3-momenta in terms of velocities and angles, using the relations $E_j = \gamma_j m_j c^2$ and $p_j = \gamma_j \beta_j m_j c$ (γ_j being the relativistic factor and β_j the velocity fraction to the speed of light of residue j), their energies and 3-momenta can be written in the following way, in terms of velocities (from ToF measurements) and angles (from position measurements):

$$\frac{1}{c^2}\left(\sum_j^N E_j\right)^2 = \sum_j^N (\gamma_j m_j c)^2 + \sum_{j\neq k} \gamma_j \gamma_k m_j m_k c^2 \tag{5.28}$$

$$\left(\sum_j^N \vec{p}_j\right)^2 = \sum_j^N (\gamma_j \beta_j m_j c)^2 + \sum_{j\neq k} \gamma_j \gamma_k \beta_j \beta_k m_j m_k c^2 \cos\vartheta_{jk}^{LAB} \tag{5.29}$$

Here, the m_j are the rest masses of the respective particles, ϑ_{jk}^{LAB} denote the LAB angles between particles j and k.
In the case of (massless) final-state γ-quanta, the formulations in equation 5.28 and equation 5.29 have to be adapted. γ-rays are simply described as having energies E_g (and totalling $E_\gamma^{LAB} = \sum_n E_g$) and momenta $\vec{p}_g = E_g/c\vec{e}_g$ ($\vec{e}_g$ being 3-vectors of unity length indicating their direction as seen in the LAB). The γ-rays are treated like a subset of the N final-state particles, with a partial index g, *i.e.*, $g \in \{1, ..., j, ..., N\}$.
Plugging equation 5.28 and 5.29 into equation 5.27 and using the relation $\gamma^2 = (1-\beta^2)^{-1}$ provides a handy formulation of the final state invariant mass:

$$\mathcal{M}_F = \frac{1}{c}\sqrt{\sum_{j\neq g}^N m_j^2 c^2 + \sum_{j\neq k\neq g\neq j}^N \gamma_j \gamma_k m_j m_k c^2 (1 - \beta_j \beta_k \cos\vartheta_{jk}^{LAB})} + \frac{E_\gamma^{RST}}{c^2} \tag{5.30}$$

with

$$E_\gamma^{RST} = \sum_g E_g \gamma_I (1 - \beta_I \cos\vartheta_{gI}^{LAB}) \tag{5.31}$$

E_γ^{RST} is the sum of the energies of the γ-quanta as emitted in the RST frame, γ_I and β_I relate to the velocity of the excited projectile/fragment, and ϑ_{gI}^{LAB} is the angle between an emitted photon and the fragment's direction, as seen in the LAB. This is equivalent to a Doppler correction and summation of each γ's LAB energy relative to the centre of mass of the excited fragment. Among the arguments of the square-root, all quadratic terms of the gamma energies E_g cancel, and a Taylor expansion of their linear terms can be made as they are comparatively small.

Because the invariant mass is conserved, $\mathcal{M}_F = \mathcal{M}_I$, it is possible to express the excitation energy in the following way, using equation 5.26 and implicitly equation 5.30:

$$\begin{aligned} E^* &= \mathcal{M}_F c^2 - m_I c^2 \\ &= c\sqrt{\sum_{j\neq g}^{N} m_j^2 c^2 + \sum_{j\neq k\neq g\neq j}^{N} \gamma_j \gamma_k m_j m_k c^2 (1 - \beta_j \beta_k \cos\vartheta_{jk}^{LAB})} - m_I c^2 + E_\gamma^{RST}. \end{aligned} \tag{5.32}$$

Similarly, the relative energy of the final state breakup particles is obtained by omitting the γ-rays' energy, so that:

$$E_{rel} = c\sqrt{\sum_{j\neq g}^{N} m_j^2 c^2 + \sum_{j\neq k\neq g\neq j}^{N} \gamma_j \gamma_k m_j m_k c^2 (1 - \beta_j \beta_k \cos\vartheta_{jk}^{LAB})} - m_I c^2. \tag{5.33}$$

I.e., in order to reconstruct the initial and final state momentum 4-vectors, the experimental setup needs to be able to provide the following information:

- Identification, in terms of atomic number Z and mass number A, of final state charged particles. Determination of neutron and proton multiplicities.
- The velocity v and scattering angles for determining kinetic energy and 3-momenta of the initial and final-state particles.
- The energy of γ-quanta possibly being emitted during the de-excitation of a final state fragment.

The previous chapters have shown that this is possible for the discussed reaction channels using the presented setup.

6

Results and Discussion

This chapter presents the results obtained by the analysis of the experimental data. In the first part the experimental indications of quasi-free scattering in inverse kinematics are summarised. The relative-energy spectrum of ^{16}F emerging from the tracking of forward protons in coincidence with ^{15}O fragments is presented in subsection two. Part three is dedicated to the inclusive two-proton-removal cross sections with different targets, leading from ^{17}Ne to ^{15}O, *i.e.*, ^{17}Ne$\rightarrow$ ^{15}O+X. Part four shows the transverse-momentum distributions of the ^{15}O fragments after nuclear one-proton-removal reactions, that are, inelastic breakup and knockout reactions.

6.1 Quasi-Free (p,2p) Scattering in Inverse Kinematics

Quasi-free scattering (QFS) reactions are expected to be identifiable by the angular signatures of the two large-angle recoil protons, which are dominated by the kinematics of free proton-proton scattering. Modifications to that will reflect the nucleus-internal properties of the knocked-out proton, *i.e.*, its quantum state, expressed by quantities such as binding energy and (angular) momentum[1]. In figure 6.1, the expectations for (p,2p) protons based on the kinematics of free p-p scattering are illustrated. The two protons exhibit a back-to-back orientation in azimuthal direction because of momentum conservation, and at energies of $\sim 500\,$AMeV they share a common opening angle of about $84\,^\circ$ (instead of $90\,^\circ$ in the limit $\beta \rightarrow 0$) within a polar range of $0\,^\circ < \vartheta < 90\,^\circ$.
For the remainder of this chapter, the observation of quasi-free events shall be outlined, focussing on proton multiplicity, proton angular correlations seen by XB and SSTs, and the proton energy measured by the XB. The C target measurements are used for identifying and subtracting the carbon background in the CH_2 target, and for comparison of the reaction mechanisms. A QFS kinematics simulation (code by L. Chulkov [78, 80]) has been employed in order to validate the experimental findings[2]. For simplicity, the proton arm detectors shall be treated inclusively here, *i.e.*, the presented results will be without any requirement on possible forward protons.

[1] Rescattering processes with other nucleons, of the knocking proton entering the nucleus, and the proton pair emerging from it, are not discussed here. For realistic modelling of the knockout process, however, they need to be considered, although at the present beam energies of ∼500 AMeV they are expected to be relatively small as the nucleon-nucleon cross-section is at minimum there.

[2] The simulation is a purely kinematical one, with the additional input being the Q-value of +1484 keV for one-proton removal from ^{17}Ne, i.e, a corresponding one-proton separation energy of $S_p = 1484\,$keV. In a Goldhaber-like model [81], S_p relates to an intrinsic momentum width of the proton to be knocked out in the (p,2p) process of $\sigma_{Goldhaber} = 51.2\,$MeV/c. That proton-momentum width in turn leads to a smearing-out of the protons' observable kinematics.

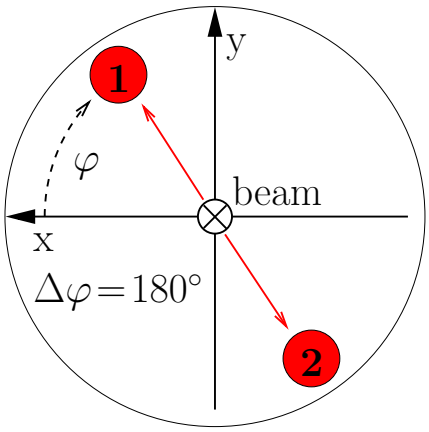

(a) Azimuthal correlation of (p,2p) protons. x and y are transverse to the beam.

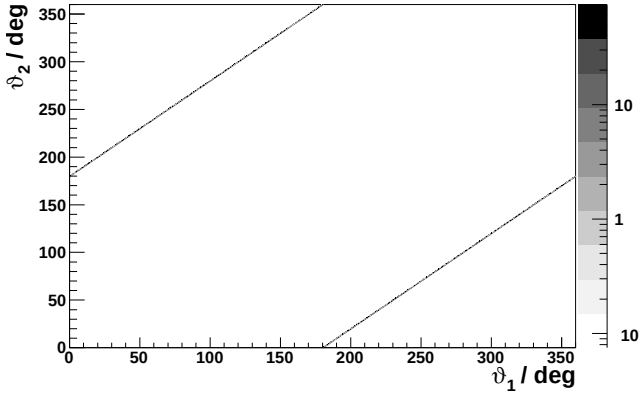

(b) 2p azimuthal angles, *via* simulation, H target, nearly 0 binding energy, nearly free p-p scattering.

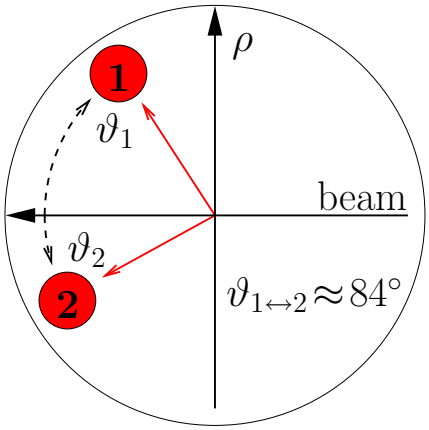

(c) Polar correlation of (p,2p) protons. ρ and the beam span the scattering plane.

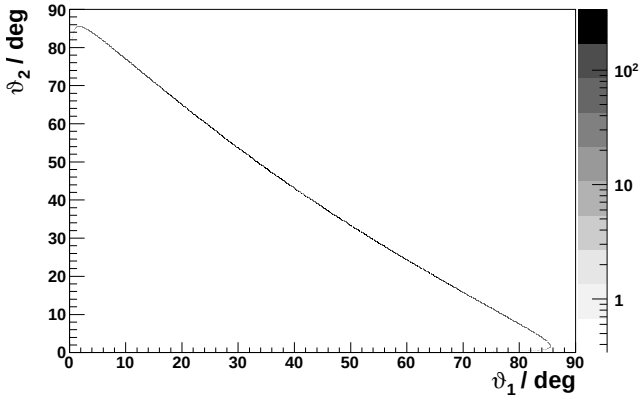

(d) 2p polar angles, *via* simulation, H target, nearly 0 binding energy, nearly free p-p scattering.

Figure 6.1: Schematic view and simulation of (p,2p) kinematics, as seen in free p-p scattering at ∼500 AMeV. (a-b) Azimuthally, the protons are back-to-back, as a consequence of momentum conservation. (c-d) In the polar plane the protons share a common opening angle of about 84 °.

6.1.1 Recoil-Proton Multiplicity

The procedure of identifying proton hits in terms of clusters of crystals in the XB has been described in chapter 4.6.1. Figure 6.2 presents the observed multiplicity distributions for CH_2, C, ET, and H targets, in coincidence with the XB sum trigger and ^{15}O fragments in the final channel. Events with proton multiplicity two are more abundant with CH_2 than with C. The events seen with the ET target might be mostly attributed to reactions in the two in-beam SSTs. The histogram in figure 6.2b featuring the H target has been obtained from normalised subtraction of the C and ET target histograms from the CH_2 histogram (figure 6.2a). Throughout this chapter, when the H target is referred to, the result of the subtraction of C and ET background from the CH_2 target, as laid out in

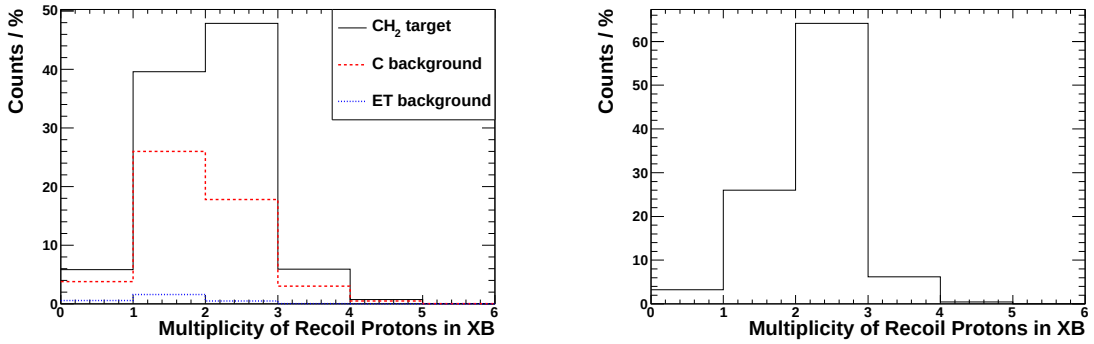

(a) Proton multiplicity: CH_2, C, and ET targets.

(b) Proton multiplicity, reconstructed H target.

Figure 6.2: Proton-cluster multiplicity in the XB in coincidence with tracked ^{15}O fragments and the XB sum trigger. The first, very left, bin stands for multiplicity = 0, the second one for 1, and so on. (a) The CH_2 target (black solid line) and background contributions are shown. The C content (red, dashed) and the ET background (blue, dotted) are subtracted to yield the mere H contribution shown in (b). In contrast to the C target with a maximum at proton multiplicity one, the majority of the H target events (∼64 %) have multiplicity two, *i.e.*, are probably (p,2p) events.

chapter 5.1.2, is meant. Arithmetically, it represents the contribution by solemnly proton-induced ^{17}Ne→^{15}O breakup reactions. In the majority of the cases (∼64 %), two emerging protons are observed. Those events are identified as from (p,2p) reactions and selected for further analysis.

6.1.2 Angular Correlations Between Recoil-Proton Pairs

Events with a proton-cluster (short: proton) multiplicity of two in the XB have been selected. As it is not possible to determine which of the two protons was the one knocked-out and which was the one in the target, their order, *i.e.*, the choice which is the 'first' and which the 'second' proton has been randomised. The laboratory angles of a proton hit (azimuthal φ, and polar ϑ) can be determined from the known geometrical orientation of the crystals that are the cluster centres. A crystal covers a relatively large solid angle within which the exact hit location is uncertain. Instead of simply attributing to a proton hit the crystal centre of gravity, which would lead to discrete angular distributions, an algorithm to randomise within each crystal's solid angle has been created, and been used for the XB-labelled plots in this chapter. Details on the randomisation algorithm can be found in appendix A.
Simultaneously, those protons are found and identified in the SST detectors. Within an energy loss range of 0 to 600 units, any hit on any of the SST detectors is checked for being within the solid-angle range of the proton-cluster central crystals. The protons' angles are then calculated from the hit position in the SSTs, at a much higher precision. In the following, the azimuthal, polar, and opening angle of two-proton events will be presented for the different targets. The better angular resolution of the SSTs will be contrasted to

the XB's, and the experimental results will be compared to the QFS simulation [78, 80]. Differences in the two-proton kinematical signatures arising from H- and from C-induced reactions will addressed.

6.1.2.1 2-Proton Events: Azimuthal Correlation

Figure 6.3 presents the azimuthal two-proton distributions, measured with the XB, the SSTs, and as result of the simulation; C and H targets are compared. Relatively similar between the C (a,c) and the H (b,d) target, the events form more (C) or less (H) broad bands around the lines of $\Delta\varphi = 180\,^{\circ}$, which correspond to back-to-back orientation of the two protons. Whereas for the H target those are interpreted as the expected (p,2p) kinematical correlation (see figure 6.1b), for the C target they may be attributed to unspecific peripheral reactions between ^{17}Ne beam and C target nuclei, which simply lead to two protons at large angles with back-to-back orientation.
Comparing the angular measurement by either XB or SSTs, it is visible that the correlation bands with the SSTs are more narrow, which should be attributed to their better resolution. Naturally, the number of proton pairs observed coincidently in the XB and the SSTs is lower than the one observed in the XB only. As a combination of limited acceptance and efficiency of the SSTs, the total detection probability is found to be approximately 70 % after background subtraction, *i.e.*, in the reconstructed H target.
Finally, the reconstructed H target data (d) is compared to simulation (e) and found to be in very good agreement. In contrast to the free p-p scattering simulation shown before (figure 6.1b), these (and all following) references to simulation refer to a 500 AMeV ^{17}Ne projectile with realistic two-proton separation energy S_{2p} of 950 keV, leading to an intrinsic proton-momentum width of $\sigma_{Goldhaber} = 51.2\,\mathrm{MeV/c}$. The observation that the simulated distribution is still more narrow is understandable by the fact that no experimental sources of broadening are taken into account. Those are in particular the influence of the target thickness, leading to an indeterminableness of the reaction vertex along the z axis, but also the angular straggling caused by the target.

6.1.2.2 2-Proton Events: Polar Correlation and Opening Angle

Figure 6.4 presents the polar two-proton distributions, measured with the XB (top), the SSTs (middle), and as result of the kinematics calculation describing ^{17}Ne(p,2p) processes (bottom). C (left) and reconstructed H (right) targets are shown. More prominent than for the azimuthal case in figure 6.3, the first two rows of figure 6.4 show a better angular resolution and smaller angular acceptance[3] of the SSTs compared to the XB. Even more intriguing are the completely different angular patterns observed with the respective C and reconstructed H targets. While the two-proton events stemming from C are simply homogeneously distributed within the $(\vartheta_1, \vartheta_2)$ phase space, the proton-induced proton pairs bear a strong (anti-)correlation along a constant sum of their polar angles. That's precisely the expected correlation of a fixed common opening angle (figure 6.1c). The experimental observation is in perfect agreement with the (p,2p) kinematics, which becomes obvious by

[3] Only the four box-SSTs were used.

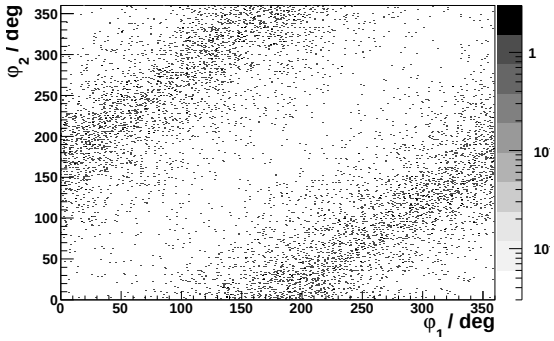

(a) 2p azimuthal angles, *via* XB, C target.

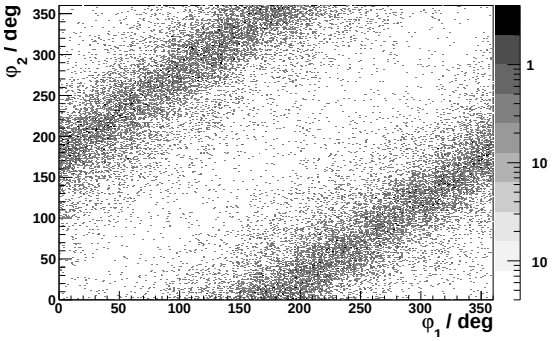

(b) 2p azimuthal angles, *via* XB, reconstructed H target.

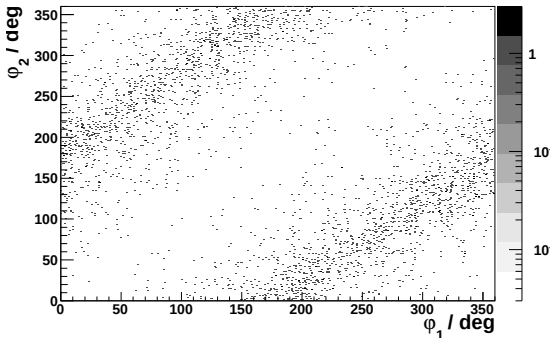

(c) 2p azimuthal angles, *via* SSTs, C target.

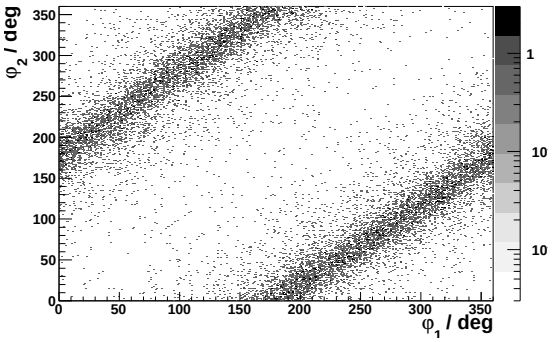

(d) 2p azimuthal angles, *via* SSTs, reconstructed H target.

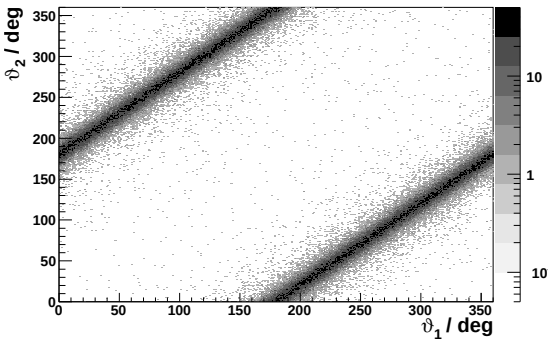

(e) 2p azimuthal angles, *via* (p,2p) kinematics calculation.

Figure 6.3: Azimuthal correlations of two protons, φ_2 vs. φ_1. Left column: C target, right column H target. Top row, (a-b): measurement with the XB. Middle row, (c-d): measurement with the four box-SSTs. Bottom row, (e): calculation using the code of L. Chulkov [78].

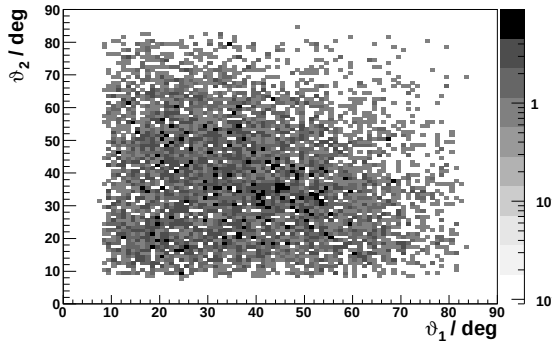

(a) 2p polar angles, *via* XB, C target.

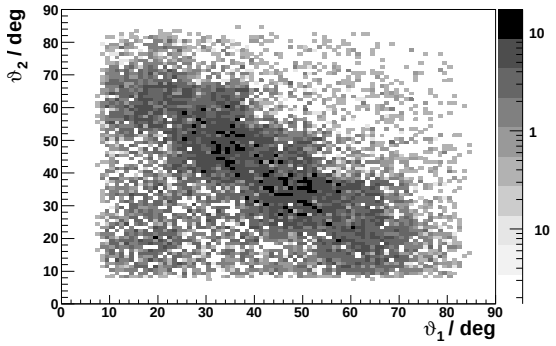

(b) 2p polar angles, *via* XB, reconstructed H target.

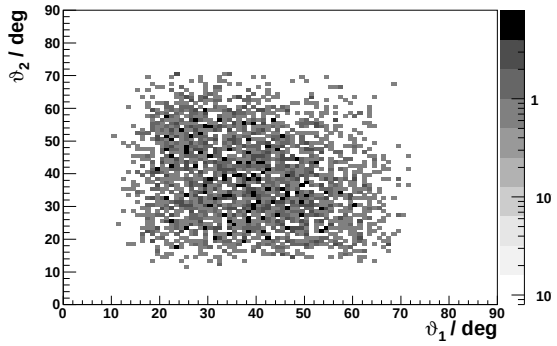

(c) 2p polar angles, *via* SSTs, C target.

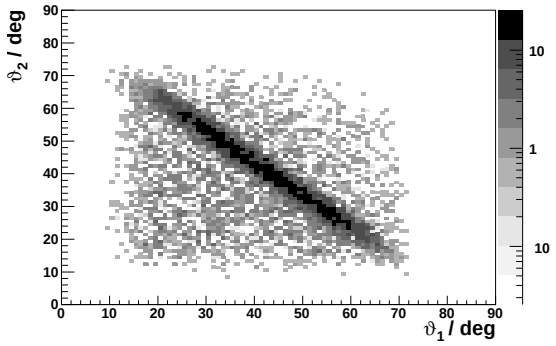

(d) 2p polar angles, *via* SSTs, reconstructed H target.

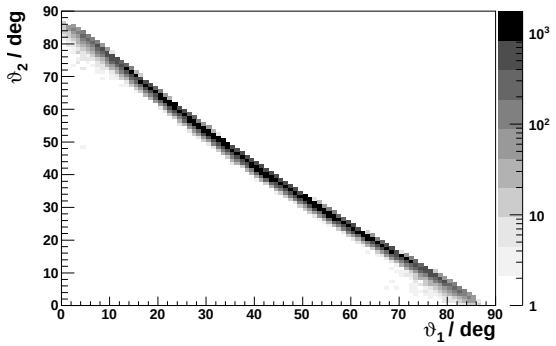

(e) 2p polar angles, *via* (p,2p) kinematics calculation.

Figure 6.4: Polar correlations of two protons, ϑ_2 vs. ϑ_1. Left column: C target, right column reconstructed H target. Top row (a-b): measurement with the XB, C and reconstructed H targets. Middle row (c-d): measurement with the SSTs, C and reconstructed H targets. Bottom row (e): calculation using the code of L. Chulkov [78].

comparing to the calculation shown in figure 6.4e; the deviations may be attributed to the not-included experimental response (vertex resolution and reduced acceptance). For

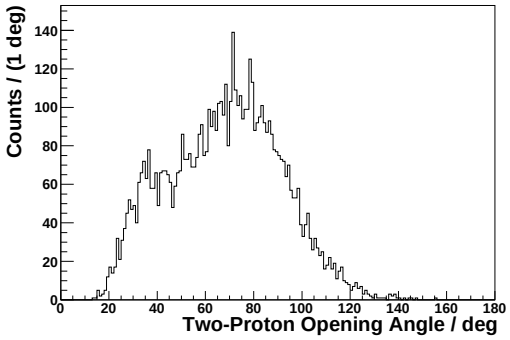

(a) 2p opening angle, *via* XB, C target.

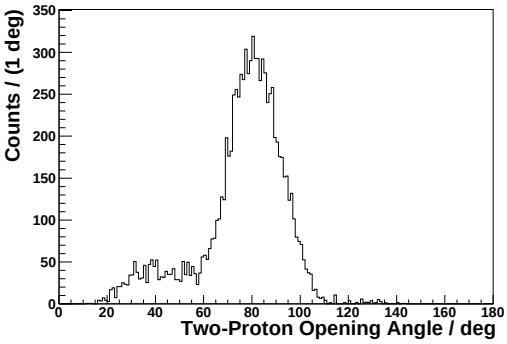

(b) 2p opening angle, *via* XB, reconstructed H target.

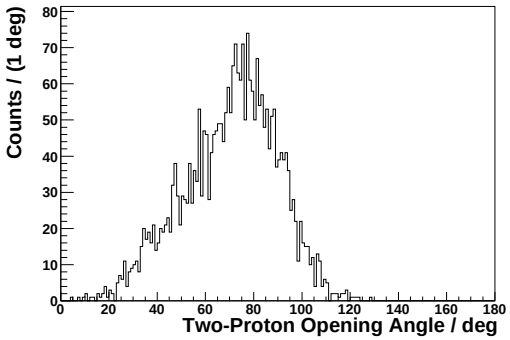

(c) 2p opening angle, *via* SSTs, C target.

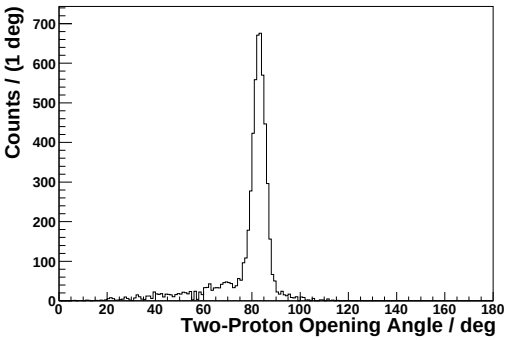

(d) 2p opening angle, *via* SSTs, reconstructed H target.

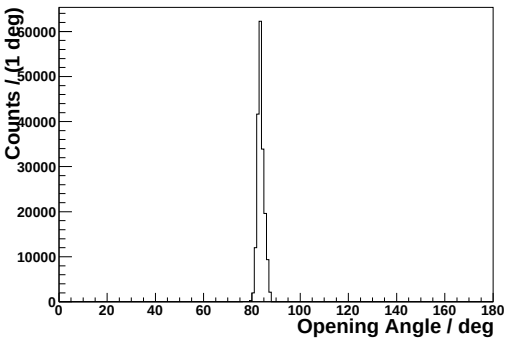

(e) 2p opening angle, *via* (p,2p) kinematics calculation.

Figure 6.5: Opening angle between two protons. Left column C target, right column reconstructed H target. Top row (a-b): measurement with the XB. Middle row (c-d): measurement with the SSTs. Bottom row (e): calculation using the code of L. Chulkov [78].

yet another view on the angular correlation of the two-proton events, figure 6.5 presents their opening-angle distributions, which are allowing for similar conclusions as the polar

correlations (figure 6.4). Two-proton events from the scattering with a proton target (right column) exhibit a fundamentally different angular pattern (namely a sharp and well-defined opening angle) than the ones from a carbon target. The previously described signatures of QFS reactions can clearly be identified with the CH_2 target and (after C and ET background subtraction) attributed to the hydrogen (proton) content in it. The actual value of the opening angle has been fitted by a Gaussian, and it results in $\vartheta_{exp} = 82.9\,^\circ$ ($\sigma_{exp} = 2.8\,^\circ$) from measurement, and in $\vartheta_{calc} = 83.7\,^\circ$ ($\sigma_{calc} = 1.3\,^\circ$) from the kinematics calculation, *ergo* in good agreement. When considering the simulated width as intrinsic, a contribution due to the experimental resolution of $\sigma_{res} = 2.5\,^\circ$ remains. By geometrical considerations this value is used to calculate a (CH_2) target thickness of 2.1 mm, in good agreement with the fabrication value of 2.3 mm. The conclusion drawn from this observation is, that the dominating contribution to the opening-angle resolution is the target thickness and the corresponding uncertainty of the position of the reaction vertex along the beam axis. Using two or more layers of SSTs, as planned for the R^{3}B experiment, will allow to suppress such an uncertainty.

6.1.3 Kinetic Energy of Recoil Protons

This section presents the measurement of the kinetic energy of (p,2p) protons and comparisons to simulation. The steps of energy calibration and gain matching of the XB for that purpose have been laid out in chapter 4.5.2. In figure 6.6, energy distributions of QFS (p,2p) protons as a function of their polar angle are shown. In particular, figure 6.6d presents the measurement of (p,2p)-proton energy loss in the XB versus their polar angle measured using the four box-SSTs. This is compared to corresponding distributions of: (a) a kinematics calculation of free p-p scattering, (b) a kinematics calculation of (p,2p) knockout with ^{17}Ne, and (c) a simulation of the measurement of ^{17}Ne(p,2p) including the experimental response, using R3BRoot. On first glance, the proton energy in the calculation of p-p scattering (figure 6.6a) does not seem to be closely related to the ^{17}Ne(p,2p) proton-energy measurement (figure 6.6d). With the guidance provided by figure 6.6b and figure 6.6c, though, the picture becomes clearer:
For free p-p scattering, the energy dependence on the polar angle is very sharp and well defined (figure 6.6a). Quasi-free knockout of bound protons[4] in ^{17}Ne with an intrinsic momentum width of $\sigma_{Goldhaber} = 51.2\,\mathrm{MeV/c}$ causes the distribution to become broad and diffuse, especially for higher energies at more forward angles (figure 6.6b). That data is used as an input to the R3BRoot simulation package in order to include the experimental response (figure 6.6c). The experimental response and resolution of the setup has been simulated with elastically scattered protons and is shown in figure B.1. The vertical red dashed lines drawn at 38.4 ° in all distributions indicate the (p-p scattering) proton-energy threshold (277 MeV for crystal punch-through). For higher energies (smaller angles), smaller fractions of the proton energy are deposited in the crystals, indicated by the down-sloping density profile towards smaller angles. The simulation compares reasonably to the measured data (figure 6.6d):
The limited angular acceptance (∼14 °–70 °) of the SSTs is visible in experimental as well as in the simulated data. The angle-dependent energy-loss profile, due to proton punch-

[4] Only knockout of the two valence protons is considered.

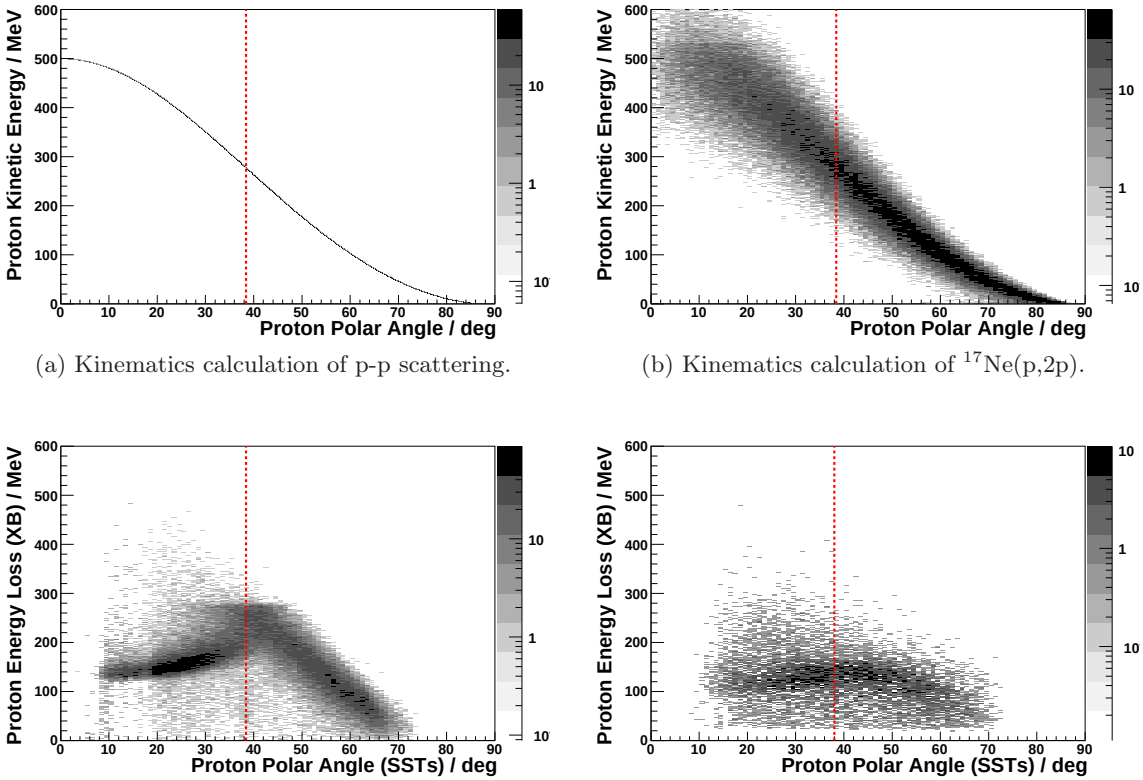

(a) Kinematics calculation of p-p scattering.

(b) Kinematics calculation of ^{17}Ne(p,2p).

(c) Simulation (R3BRoot) of ^{17}Ne(p,2p).

(d) Measurement of ^{17}Ne(p,2p), reconstructed H target.

Figure 6.6: Proton energy as a function of polar angle. (a) Kinematics calculation of free p-p scattering; (b) Kinematics calculation of ^{17}Ne(p,2p); (c) Simulation including the experimental response (R3BRoot) of ^{17}Ne(p,2p) *via* XB (energy) and SSTs (polar angle); (d) Measurement of ^{17}Ne(p,2p) *via* XB (energy) and SSTs (polar angle). The vertical red dashed line at 38.4 ° indicates the angle at which protons from free p-p scattering at 500 MeV incident have an energy of 277 MeV, above which (for smaller angles) they would punch through the crystals.

through at an angle of ∼38.4 °, is well visible and also reflected in the measured data. The measured energy distribution is understood as convolution of the ^{17}Ne(p,2p) kinematics with the experimental response. The determination of the experimental response will allow for an extraction of the reaction width, which in turn reflects the knockout proton's binding energy and intrinsic momentum width. Thus, the underlying picture for the ^{17}Ne(p,2p) knockout processes is confirmed here.

A further important observation is, that the absolute energy scales when comparing simulation to experiment do not match. Extrapolating the linear part of the proton energy data in figure 6.6d further to smaller polar angles would lead to a value of 250-300 MeV at 10 °, and not ∼500 MeV as expected by simulation. Apparently, the means of photon- and muon-based energy calibrations (chapter 4.5.2) do not apply properly for determining the proton energy loss. A probable source for this behaviour is quenching, *i.e.*, the reduction of

light yield per unit energy loss for particles with increasing ionisation density, as it is this case for protons compared to muons and photons.

6.1.4 Improvements of the Recoil-Proton Detection — a Discussion

The present means of proton calorimetry using scintillating crystals — in the Crystal Ball at the R^{3}B/LAND setup, and in future in the CALIFA detector at the R^{3}B setup — will never achieve an energy resolution ($\sim 10^{-4}$) as good as a magnetic spectrometer. Nevertheless, this drawback is more than compensated by the advantages of near 100 % acceptance, and the simultaneous γ-ray detection using the same detector. However, the proton energy-momentum measurement as such is crucial in (p,2p) reactions for the reconstruction of the proton-separation energy, that in turn will allow to determine the previously occupied single-particle state for the knocked-out proton. A few thoughts for improvements of these measurements are given below:

- Alternatively or additionally to using cosmic muons, a more convenient approach to calibrate the XB crystals for (p,2p) measurements would be to directly use proton beams at various energies impinging onto the CH_2 target. By illuminating the forward XB hemisphere with elastically scattered protons, a precise angular measurement with the SSTs yields a precise determination of proton energies which can in turn be used to calibrate the detector.

- Currently, the proton-energy-loss profile in the XB is strongly affected by the punch-through for forward angles (higher energies). This effect will complicate the determination of (p,2p) in that angular/energy region; *e.g.*, as seen in the measurements with proton beams (chapter 3.2.3.3), the energy resolution for punching-through protons is reduced. If one wants to deal only with fully stopped protons, either the beam energy has to be reduced, or the crystals' stopping power increased. Reducing the beam energy is not practical, as it would lead to a loss of acceptance for projectile-like fragments and protons due to the reduced forward-focusing, and additionally would blur the (p,2p) reactions by increasing the chance for secondary scattering processes of the initial and final protons due to the increasing nucleon-nucleon cross section towards lower energies.
  There is the option to change the stopping power of the crystals, as for the future CALIFA calorimeter at R^{3}B. Crystals of different material (CsI or LaBr, instead of NaI) and dimensions are to be chosen. A compromise has to be found considering not only the energy measurement of (p,2p) protons, but also the measurement of γ-rays, and the limits for the total size and cost of the detector.

- A measurement concept currently being prototyped and tested for high-energy recoil protons (300-700 MeV) in the forward end-cap section of the future CALIFA calorimeter are so-called Phosphor Sandwich (phoswich) scintillator detectors [82]. Those are crystal doublets of different scintillator material, being read out by a common PMT. Recently, stacks of $LaBr_3$(Ce) + $LaCl_3$(Ce) crystals have been tested using proton beams at energies between 120 and 180 MeV [82]. Those relatively modern scintillator materials exhibit different properties, *e.g.*, in terms of stopping power and decay time.

By means of pulse-shape analysis it is possible to disentangle the signal contributions from proton energy loss in both parts of the phoswich detector and thus determine with high precision the proton energy, also in the case of punch-through.

6.1.5 Inverse-Kinematics QFS — Conclusions

It has been found that QFS reactions of ^{17}Ne with a proton-rich CH_2 target can very well and nicely be identified by the angular correlations of the proton pairs registered in the XB and SSTs. Quantitatively, it is found that a tag on those reactions, *e.g.*, by a cut on the opening angle, is nearly background-free, meaning that the broad and unspecific underlying background can be attributed to stem from reactions on the C nuclei in the CH_2 target or the other material in the setup. QFS reactions are identified and well understood in terms of the observed agreement between experiment and simulation. The characteristic angular correlations can serve as a very clean tag or trigger of QFS for all other coincident observables.
The measurement of (p,2p) proton energy is found to be in qualitative agreement with the simulation. In terms of energy calibration and resolution, the experimental findings still promise room for improvement.

6.2 One-Proton Removal from ^{17}Ne — Relative Energy of the Unbound ^{16}F

In this section the tracking of projectile-like forward protons — from the instantaneous dissociation of the unbound ^{16}F into ^{15}O+p after a proton knockout from ^{17}Ne — and the reconstruction of the ^{16}F relative-energy spectrum are presented. The ^{16}F relative-energy spectrum is needed in order to distinguish 'halo' knockout causing the population of energetically lower-lying states from ^{15}O-core knockout populating higher states.
The tracker programme, as introduced in chapter 5.2, was used not only to track and select ^{15}O fragments, but also employed to find and track any possible number (0, 1, or 2 being realistic expectations) of forward protons, and determine their energies, angles and momenta. Correspondingly, the events have additionally been pre-filtered by requiring a trigger from the TFW ToF-wall (Tbit16), and by demanding reasonable values for the hit multiplicities in the proton detectors; that is, greater than zero and smaller than 6 for the PDCs and the TFW.
First, the observed hit multiplicities for forward protons will be shown. A discussion of the ^{16}F = ^{15}O+p relative-energy spectrum follows. The measurement of inclusive one-proton removal on the carbon target will be compared to data from (p,2p) quasi-free scattering on the CH_2 target, *i.e.*, events with a proton-cluster multiplicity of two in the XB.

6.2.1 Projectile-like Protons

Figure 6.7 presents the observed hit-multiplicities of forward (projectile-like) protons, found in coincidence with a ^{15}O fragment by the tracker program. Acceptance and efficiency determination and correction for the proton-tracking algorithm have not been performed yet.

The top row of figure 6.7, XB-inclusive[5] two-proton removal, shows little dependence of the

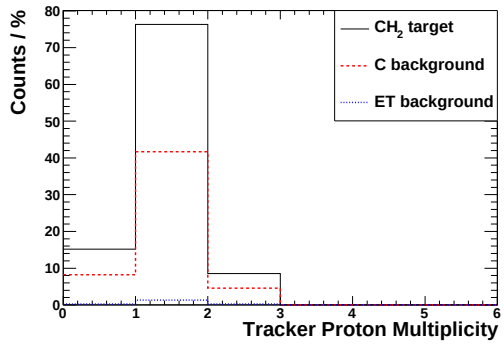

(a) CH_2 target (black-solid), with C (red-dashed) and ET (blue-dotted) background, XB-incl.

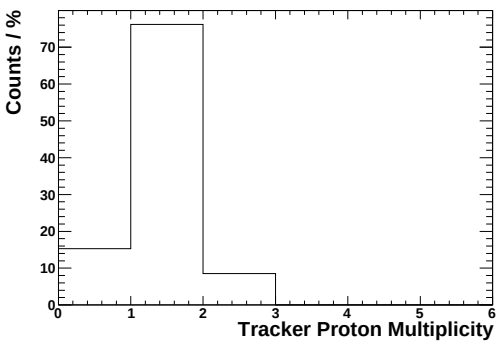

(b) H content of the CH_2 target, XB-incl.

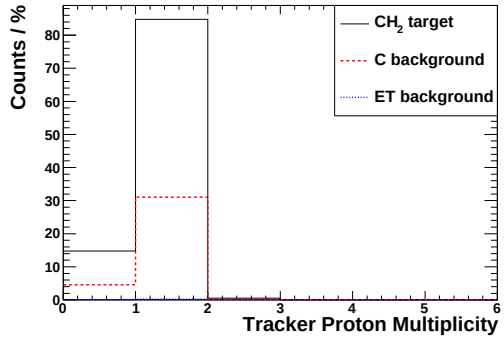

(c) CH_2 target (black-solid) with C (red-dashed) and ET (blue-dotted) background, (p,2p).

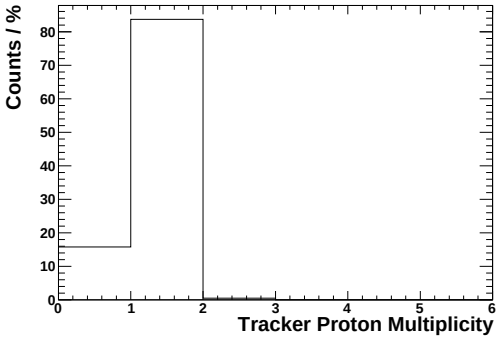

(d) H content of the CH_2 target, (p,2p).

Figure 6.7: Multiplicity distributions from tracked forward protons coincident with ^{17}Ne→^{15}O for different targets, and comparing XB-inclusive (top row) to (p,2p) knock-out (bottom row) channels; (p,2p) means that two high-energy clusters have been found in the XB. In the left column the CH_2 target and the normalised background contributions from C and ET targets are shown. CH_2 data is shown as a black-solid line, C red-dashed, and ET blue-dotted. The right column features the H content of the CH_2 target.

forward proton multiplicity on the target in use. With ^{15}O in the final channel (and the other pre-filters mentioned above), there are zero, one or two protons reconstructed, where one is being predominantly observed. For the H content of the CH_2 target the multiplicity distribution shows zero with 15.3 %, one with 76.2 %, and two with 8.5 % of all events; for the carbon target those numbers are very similar.
What is reflected in those multiplicities of zero, one, and two forward protons — neglecting the not yet performed corrections for efficiency and acceptance — are the relative contributions to the ^{15}O production from various proton-knockout processes or other types of inelastic breakup of ^{17}Ne. The observation of two forward protons within the acceptance simply indicates a soft excitation of ^{17}Ne above its 950 keV 2p threshold, dominantly

[5]That is, without any cut on any trigger or observable obtained from the Crystal Ball.

via electromagnetic or diffractive dissociation. One observed proton indicates a direct one-proton-removal reaction, like (p,2p) on the CH_2 target or peripheral knockout on the carbon target. Zero forward protons, finally, are a signature of either a direct two-proton knockout from ^{17}Ne, or a more violent inelastic process. A look to the bottom row of figure 6.7, having demanded a (p,2p) channel using the XB as outlined in the previous 6.1.1, confirms the inclusive picture. First of all, most of the multiplicity-2 events vanish. That is very reasonable, because of the nature of quasi-free one-proton knockout not leading to a continuum excitation of the whole projectile. The large majority of the events have a forward-proton multiplicity of one, as expected in one-proton knockout from ^{17}Ne. Events with multiplicity zero can be explained by either a mis-identification of the (p,2p) channel using the XB, or by missing efficiency and/or acceptance of the proton-arm detectors in combination with the tracking algorithm. For simplicity, these multiplicity-two events are interpreted by efficiency/acceptance of the proton-arm and tracking algorithm only, and it is concluded that the proton-detection efficiency using the C target amounts to about 87 %, and using the H content of the CH_2 target it amounts to about 84 %.

6.2.2 ^{15}O+p Relative-Energy Spectrum

Figure 6.8 presents the experimental data of the reconstructed $^{16}\mathrm{F} = {}^{15}\mathrm{O}+\mathrm{p}$ spectra, reconstructed *via* the invariant-mass approach laid out in chapter 5.3. Different targets (C, H) and different channels (XB-inclusive, 2-recoil-protons/(p,2p)) are compared. The energy (x) axis of the spectra in figure 6.8 is relative to the ^{15}O+p threshold; the ground state resonance of the unbound ^{16}F is at 535 keV. The eight lowest known resonance-states (width all below 100 keV) [83] are indicated by arrows. Those states are also shown schematically in figure 6.9b, together with the knockout processes they are assumed to be populated by in figure 6.9a [5]. Common to all four distributions is a quite prominent low-energy region at around 0–2 MeV, and a weaker and broader background-like structure from 2 to around 8 MeV. The low-energy region coincides well with the four lowest-lying negative-parity states of ^{16}F (orange arrows), and is attributed to halo-proton states in ^{17}Ne; 0^- and 1^- (at 535 keV and 728 keV, respectively) stem from s-proton knockout, and 2^- and 3^- (at 959 keV and 1256 keV) stem from d-proton knockout (see figure 6.9). The next four ^{16}F resonances of 1^+, 2^+, 3^+, and 1^+ (with energies 4293 keV, 4405 keV, 4907 keV, and 5189 keV) are indicated by purple arrows and can be assigned to the broad and weak high-energy region of the spectrum. There is great interest to distinguish the knockout-from-halo states from the knockout-from-core states in ^{17}Ne in order to be able to compare the data to theoretical calculations that concentrate on knockout from halo [5]. For practical reasons, as at the moment the situation with the ^{16}F spectrum cannot be qualified or quantified further, a cut of $\leq$2 MeV is chosen in order to select halo states. For events with proton-multiplicity two in the XB, $\eta^{p2p}_{halo}(C) = 72.2\,\%$ of the C target events are attributed as stemming from halo-knockout; for the H target that percentage is $\eta^{p2p}_{halo}(H) = 64.0\,\%$. This selection and quantification is crucial for a better specification of the reaction channel, and will be employed for the discussion in the following chapter 6.3 and chapter 6.4.

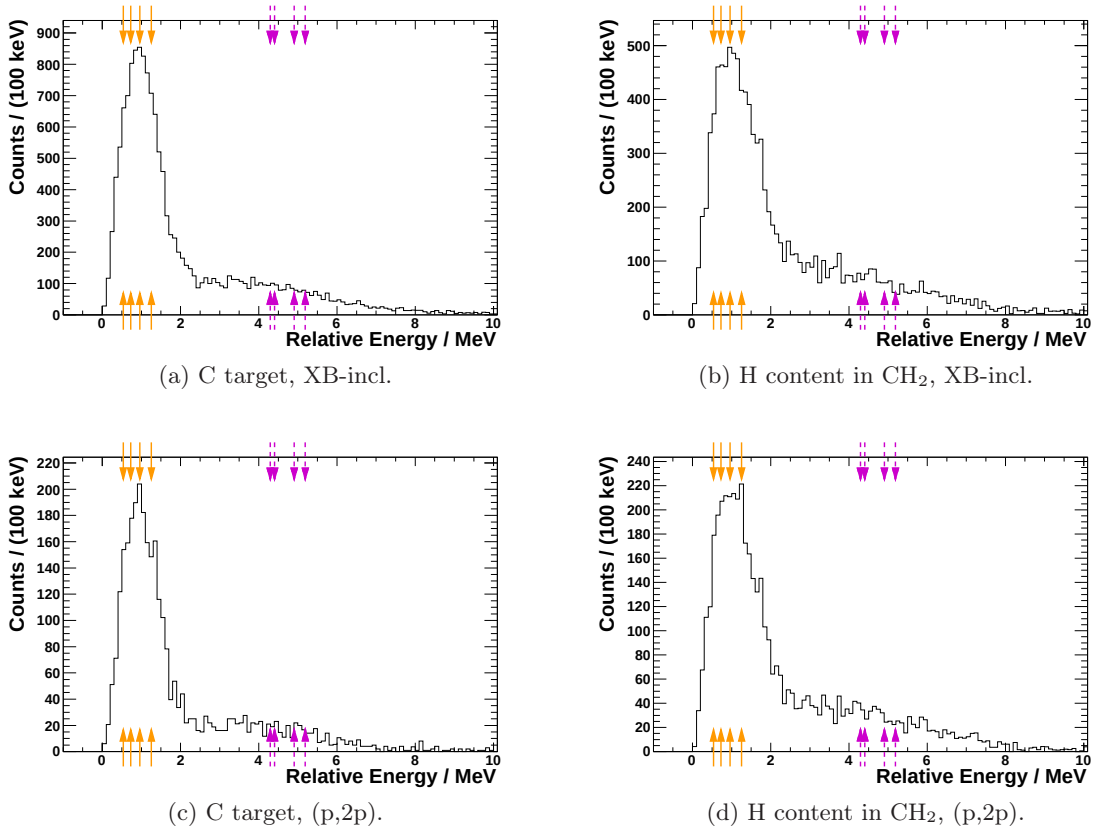

(a) C target, XB-incl.

(b) H content in CH_2, XB-incl.

(c) C target, (p,2p).

(d) H content in CH_2, (p,2p).

Figure 6.8: ^{16}F relative energy, relative to the ^{15}O+p threshold at 0 MeV. Compared are the XB-inclusive (top row) and the (p,2p) knockout (bottom row) channels, vs. the employed targets, carbon (left column) and H (right column), after subtraction of C and ET background from the CH_2 target. The arrows indicate the resonance-states of ^{16}F known from literature, and being shown in figure 6.9b. Orange arrows indicate states populated by the knockout of valence protons of ^{17}Ne, whereas purple arrows indicate knockout of core protons from ^{17}Ne. All resonance states have a width of $\leq$ 100 keV.

6.3 Inclusive Two-Proton-Removal Cross Sections

This section presents the results obtained for the inclusive two-proton-removal cross sections with the different targets from ^{17}Ne, *i.e.*, from the $^{17}\text{Ne}\xrightarrow{Target}{}^{15}\text{O}+\text{X}$ channel. In order to purify the channel selection, several steps had to be taken. First, the set of events with otherwise good initial ^{17}Ne was cut by around 40 % of those events with too largely negative angle in x-direction, *i.e.*, those with a too strong left-to-right inclination while passing the setup. This was necessary as those events would be deflected very far to the right when passing the ALADIN magnetic field so that they would have to penetrate the outer frame of the imminent first PDC before finally hitting the NTF. This extra material for a part of the beam is a source of breakup reactions that could such be inactivated. Second, additionally to the selection of oxygen isotopes in the NTF ToF-wall, both in-beam SSTs have been used

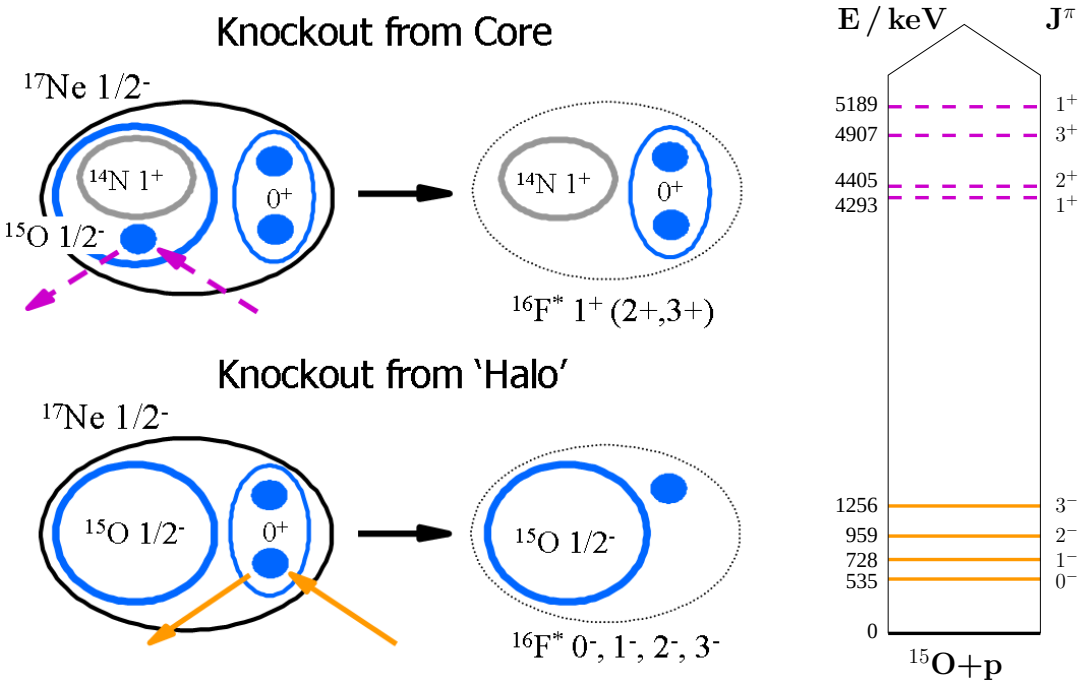

(a) Schemes of proton knockout processes from the core and halo of ^{17}Ne.

(b) Continuum states in ^{16}F = ^{15}O + p.

Figure 6.9: Proton knockout from halo (orange) and core states (purple) in ^{17}Ne, according to [5]. (a) Schemes of the knockout processes from 'halo' and from core states. (b) Corresponding ^{16}F energy level scheme. The two lowest resonances are populated by s-proton knockout, and the two next higher ones by d-proton knockout from ^{17}Ne.

to select final-state oxygen fragments directly after the reaction target[6]. This is crucial in order to suppress the background caused by further material in the beam, *e.g.*, beam-line components and detectors.
Figure 6.10 shows the energy-loss spectrum of the K-side of SST3, with a cut on non-neon isotopes on the S-side of SST3, for all targets of CH_2, C, Pb, and the reconstructed H. A summary of the results shown in figure 6.10 is given in table 6.1. The various employed targets are listed column-wise, while the four SST sides to employ for the auxiliary background-reduction cut are listed row-wise. The four values for four ways to purify the channel represent four independent measurements, the given errors are statistical.

6.4 Transverse-Momentum Distributions of Fragments

Relative to the (^{17}Ne) projectile centre-of-mass frame, the momentum of the (^{16}F / ^{15}O) final state fragment can be decomposed into a longitudinal component ($\vec{p}_{\parallel}$, parallel to the

[6]Practically, that means selecting events that are not neon, and not noise nor overflow. No atomic charges other than neon and oxygen are possible.

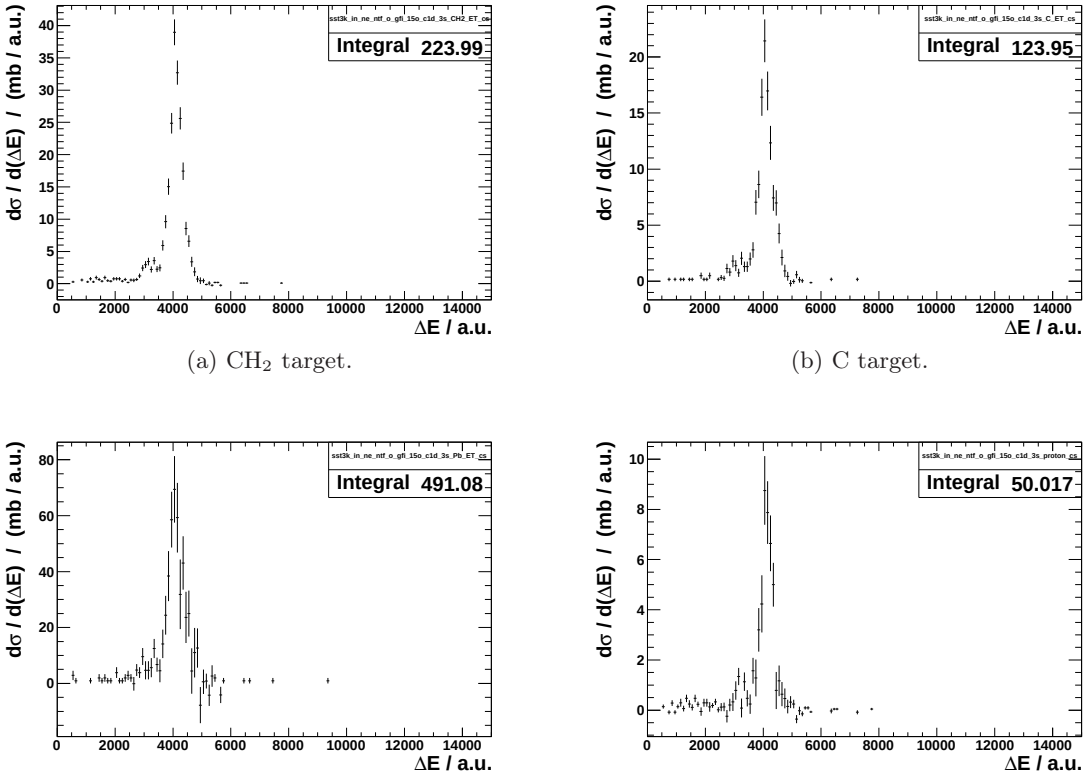

(a) CH_2 target.

(b) C target.

(c) Pb target.

(d) Reconstructed H target.

Figure 6.10: Differential cross section, as a function of the fragment's energy loss, measured with the K-Side of SST3, which is the short (y-oriented) side of the in-beam detector located directly behind the target. The peak-like distributions correspond to oxygen, the unreacted-beam background has been suppressed. ^{15}O has been selected using NTF and the GFIs, with an additional purification cut on not-neon using the S-side of SST3. Normalisation has been done with respect to the number of unreacted beam events and the target thickness parameter. Subplots (a) to (d) depict the spectra with CH_2, C, Pb, and the reconstructed H target (see chapter 5.1.2), respectively. The spectrum integrals are in the unit of mb and reflect the integral cross sections, since the ET-related background has been subtracted.

incoming projectile), and into a transverse component ($\vec{p}_\perp$, perpendicular to it)[7]:

$$\vec{p}(fragment) \quad = \quad \vec{p}_\parallel(fragment) + \vec{p}_\perp(fragment). \tag{6.1}$$

The absolute momentum of a final state fragment is obtained from the tracking program. Both momentum components equally well contain information of the quantum nature of the projectile and are worth analysing. For the presented setup, the resolution for the transverse

[7]Of course, the same statement holds true for any final state particle, as for instance the forward protons.

	Cross Section (mb)			
	CH_2	C	H	Pb
Cut: 3S	224 ± 5	124 ± 5	50 ± 3	491 ± 37
Cut: 3K	229 ± 5	128 ± 5	50 ± 3	506 ± 47
Cut: 6S	227 ± 5	124 ± 5	51 ± 3	515 ± 51
Cut: 6K	222 ± 6	127 ± 5	48 ± 3	511 ± 56
Average	226 ± 3	126 ± 2	50 ± 2	506 ± 23

Table 6.1: Summary of the ^{17}Ne → ^{15}O+X inclusive two-proton-removal cross sections, σ_{-2p}, measured with different targets, and by using different background-reduction cuts on either the S- or the K- sides of one of the two SST detectors directly behind the target, SST3 and SST6. The "H" target corresponds to the H content of the CH_2 target and has been obtained by subtracting a normalised fraction of the C from the CH_2 target and dividing the remainder by two.

component is far better than the one for the longitudinal component, and thus will alone be discussed here. Its main ingredient, the fragment scattering angle, is derived from the positions measured directly by the PSP and SST detectors as described in chapter 5.2.1. Before having a look at actual transverse-momentum distributions, the following section will briefly present and discuss the setup's mere angular resolution.

6.4.1 Angular Resolution of the Setup

As described in chapter 5.2.1.2, the angular resolution of the setup can be determined by analysing elastic scattering reactions, *e.g.*, ^{17}Ne→^{17}Ne. As a first step, it is helpful to verify the consistency and correctness of the determination of the angular straggling caused by the target, by comparing it to simulation calculations, *e.g.*, to ATIMA [70].
Experimentally, the straggling in the target, $\sigma_{straggling}(target)$, is derived from the quadratic subtraction of the widths[8] of the Gaussian-shaped elastic-scattering-angle distributions with and without target, ($\sigma_{total}(target)$) and ($\sigma_{total}(empty)$), respectively:

$$\sigma^2_{straggling}(target) \quad = \quad \sigma^2_{total}(target) - \sigma^2_{total}(empty) \tag{6.2}$$

In this case, the scattering angle width with the empty target, $\sigma_{total}(empty)$, signifies nothing but the actual angular resolution achievable with the setup (for ^{17}Ne at the specific energy)[9]. Figure 6.11 gives an example for such scattering angle distributions with the CH_2 target and with the empty target; x and y coordinates are considered separately. Although being different along x and y, the experimental widths presented in figure 6.11 lead to values for the target straggling contribution that are mostly consistent with each other;

[8] By width, the σ standard deviation of a Gaussian distribution is meant here.

[9] As a reminder, that angular resolution of the pure setup stems from the position resolution of the detectors, the straggling in them, and further passive material (here: POS) in between.

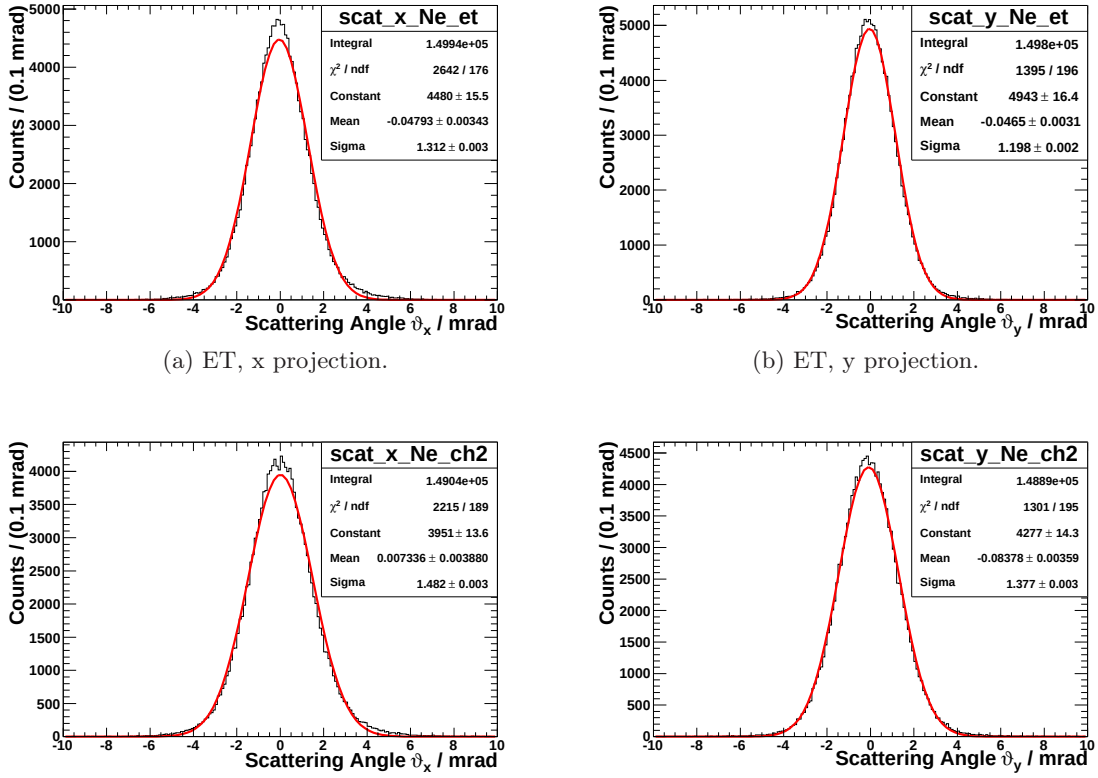

(a) ET, x projection.

(b) ET, y projection.

(c) CH_2, x projection.

(d) CH_2, y projection.

Figure 6.11: Example of elastic-scattering-angle distributions of ^{17}Ne→^{17}Ne, x projection (left column) and y projection (right column). Shown are counts (y) vs scattering angle (x), in mrad. The experimental distributions (black thin solid line) have been fitted by Gaussians (red thick solid line). Top row: empty target (ET). The Gaussian width-parameter (σ) in x is slightly larger (1.312 mrad) than the one in y (1.198 mrad). Bottom row: CH_2 target. The scattering angle width is 1.482 mrad along x and 1.377 mrad along y.

for example the CH_2 target: $\sigma_{str}(CH_2, x) = 0.69 \pm 0.01$ mrad, and $\sigma_{str}(CH_2, y) = 0.68 \pm 0.01$ mrad. The following table 6.2 summarises the obtained values of target straggling and compares them to the values simulated with ATIMA.

In table 6.2, the errors for the ATIMA-calculated values stem from the 2 % uncertainty of the target thickness. The only big deviation between measurement and calculation arises for the Pb target; if one trusts both ATIMA and the correctness of the measurement procedure as they agree well for C and CH_2, a possible interpretation is that the Pb target in reality was a bit thinner than stated by the producer. On the other hand, there might be a systematic uncertainty in the width determination of the experimental distributions as they are not perfectly described by a Gaussian, at their peaks, and partly at their tails.
Continuing the line of ^{17}Ne elastic scattering with ET data, the angular straggling $\sigma_{str}(setup)$ from the further relevant setup components (POS, PSP2, SST3) is calculated, yielding a value of 0.830 mrad. Employing equation 5.19, the angular resolution of the PSPs and the

	Angular Straggling (mrad)		
Target	Measured (x)	Measured (y)	ATIMA
CH_2	0.691 ± 0.009	0.679 ± 0.007	0.696 ± 0.007
C	0.931 ± 0.007	0.914 ± 0.006	0.941 ± 0.010
Pb	1.711 ± 0.006	1.719 ± 0.006	1.781 ± 0.018

Table 6.2: Angular straggling caused by the CH_2, C, and Pb targets for ^{17}Ne at 500 AMeV. The values derived from measurements of the x and y projections of scattering-angle distributions are compared to a simulation calculation using the ATIMA code using nominal experimental parameters.

SSTs — based on their mere position resolution — is determined; it results in $\sigma_{PSPs,SSTs}(x)$ = 1.016 mrad, and $\sigma_{PSPs,SST}(y)$ = 0.861 mrad. Obviously, the resolution in y is better, an observation that should be attributed naturally not to the isotropic PSPs, but to the SSTs and their different readout-strip pitch ($d_S = 110\,\mu$m, $d_K = 104\,\mu$m) along their respective S- and K-sides[10]. For convenience, the setup properties in terms of resolution and straggling as just derived are assumed to hold true also for different outgoing fragments, *e.g.*, ^{15}O at possibly slightly different velocities due to a precedent breakup reaction of ^{17}Ne.

6.4.2 Transverse-Momentum Resolution

Similarly to the idea of the previous chapter 6.4.1, it is necessary to determine the transverse-momentum resolution from elastic-scattering reactions of ^{17}Ne, *i.e.*, from the unreacted beam. Additionally to the angular resolution just described, the transverse-momentum resolution depends on the precision of the tracking procedure, and, to a very small extent though, on the ToF-resolution for the fragments[11]. As well as for the scattering angles, the respective projections along either x or y of the transverse momentum will be considered, that is, with $\vec{p}_\perp = \vec{p}_{\perp,x} + \vec{p}_{\perp,y}$, and $p_\perp^2 = p_{\perp,x}^2 + p_{\perp,y}^2$. As the tracking program provides the absolute value of the fragment momentum, its transverse components are calculated using the scattering angles:

$$p_\perp^{x,y} \quad = \quad p \cdot \sin \vartheta_{scat}^{x,y}. \tag{6.3}$$

The following plots in figure 6.12 depict the ^{17}Ne elastic-scattering transverse-momentum distributions for the various targets, for the example of the y projections. The experimental distributions tend to slightly deviate from a perfect Gaussian shape, mostly by a slight overshoot at the peak, and by slightly wider flanks at the foot. Nevertheless, for the purpose of quantifying the resolution, they are fitted by Gaussians and characterised by their Gaussian width parameter (σ). An overview of these results, including the x projections, is given in table 6.3.

[10] As a side note, the position resolution of the SST detectors could possibly be further improved/homogenised by an η-correction of the cluster centre-of-gravity (remind chapter 4.4.2). However, that procedure has just been established recently and is scheduled for application to the upcoming future.

[11] The ToF resolution is relevant to the longitudinal fragment momentum resolution, most of all.

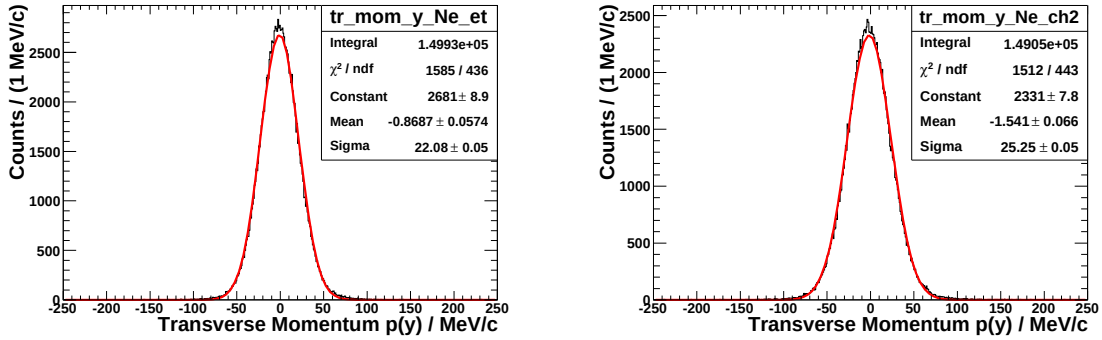

(a) ET, p_y.

(b) CH_2, p_y.

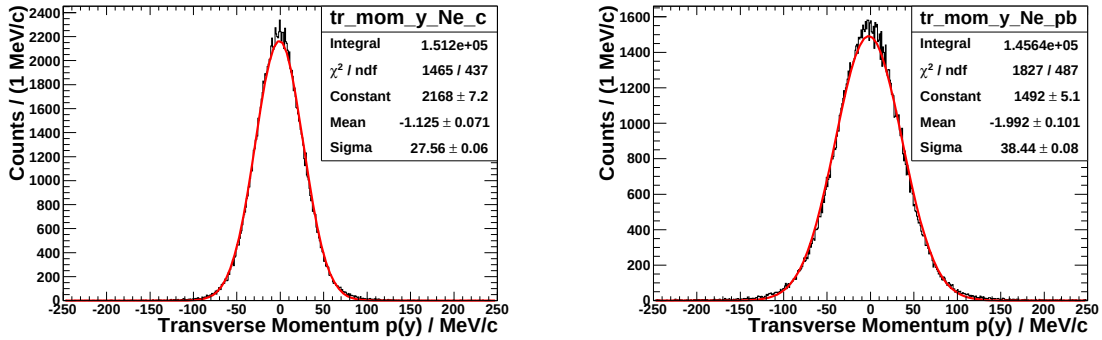

(c) C, p_y.

(d) Pb, p_y.

Figure 6.12: Transverse-momentum distributions of ^{17}Ne elastic scattering, y-projections. Shown are counts vs. MeV/c. Plots (a-d) are featuring ET, CH_2, C, and Pb targets, respectively. The experimental distributions (black thin solid lines) are approximated by Gaussians (red thick solid lines). The measured difference in the Gaussian width parameter (σ) for a target and ET is attributed to the straggling in that target.

	Transverse-Momentum Width and Straggling (MeV/c)			
Target	Width (x)	Width (y)	Straggling (x)	Straggling (y)
ET	24.16 ± 0.05	22.08 ± 0.05	—	—
CH_2	27.19 ± 0.06	25.25 ± 0.05	12.47 ± 0.17	12.26 ± 0.14
C	29.42 ± 0.06	27.56 ± 0.06	16.79 ± 0.14	16.49 ± 0.11
Pb	39.55 ± 0.09	38.44 ± 0.08	31.31 ± 0.12	31.48 ± 0.11

Table 6.3: Experimental widths of the x and y components of the transverse-momentum distributions of ^{17}Ne→^{17}Ne elastic-scattering reactions at 500 AMeV in the CH_2, C, and Pb targets, and without any target (ET). The straggling contribution by the respective targets is determined from a quadratic subtraction of the beam-intrinsic width which is reflected in the width measured without target (ET).

It is found that the straggling contribution to the transverse momentum caused by the presence of the targets is determined in a consistent way both from the x and the y measurement. The resolution in y is again — as for the scattering angle — found to be better than in x.
When presenting and discussing the transverse-momentum distributions from reactions, *e.g.*, with ^{15}O fragments in the final state, the contribution to their width from the just obtained resolution has to be taken into account and subtracted, in order to retain the width that stems from the actual reaction. As the momentum of a particle scales with its mass, $p \propto m$, in a first approximation the subtraction of the momentum width has to be done with a normalisation to the nuclear mass. For example for ^{15}O fragments the reaction width is determined as:

$$\sigma^2_{reaction}\left(^{17}\mathrm{Ne} \rightarrow {}^{15}\mathrm{O}\right) = \sigma^2_{total}\left(^{15}\mathrm{O}\right) - \left(\frac{m(^{15}\mathrm{O})}{m(^{17}\mathrm{Ne})}\sigma_{total}\left(^{17}\mathrm{Ne}\right)\right)^2 . \qquad (6.4)$$

6.4.3 ^{16}F Transverse-Momentum Distributions

As laid out in chapter 2.2.1, the momentum distribution of the residual fragments in knockout reactions in inverse kinematics reflects the intrinsic momentum distribution of the knocked-out nucleons. Its shape allows for the extraction of the nucleons' orbital angular momentum value l in the nucleus' ground-state wave function. In the present case of the study of one-proton knockout from ^{17}Ne, the residual ^{16}F fragment is unbound, and it immediately disintegrates into ^{15}O+p. In order to deduce the transverse momentum of ^{16}F, the momenta of ^{15}O and the proton, obtained using the tracking routines described in chapter 5.2, are added: $\vec{p}(^{16}\mathrm{F}) = \vec{p}(^{15}\mathrm{O}) + \vec{p}(\mathrm{proton})$. Figure 6.13 presents the x (left column) and y (right column) projections of the transverse momentum distributions of ^{16}F after one-proton knockout from ^{17}Ne. Knockout from 'halo'-states in ^{17}Ne (upper row) is compared to knockout from core-states (lower row), as discussed in chapter 6.2.2. Two main observations can be made. First, the momentum distributions stemming from 'halo' knockout are more narrow (smaller rms values) than the ones that are attributed to core knockout. Second, the x distributions are affected by acceptance limitations, as the drop-off at large negative values (strong left-to-right inclination through the ALADIN magnet) shows. The distributions are shown using a binning of 10 MeV/c, as that is reasonably below the determined resolution of 25-30 MeV/c described in the previous chapter 6.4.2. The resolution contribution of the protons has been neglected here.

Figure 6.14 shows the x (a) and y (b) projections of the ^{16}F transverse-momentum distribution, reconstructed *via* the addition of the momenta of a coincident ^{15}O+p pair, resulting from diffractive or one-proton-knockout reactions of ^{17}Ne on the C target. A condition on the ^{16}F relative energy to be smaller than 2 MeV ensures that valence (or 'halo') protons of ^{17}Ne have been removed. The data (black crosses) is described by a Glauber-model based calculation of the ^{16}F transverse-momentum projection in terms of a superposition (red full line) that consists of weighted contributions of knockout from s-wave valence protons (green dashed line) and d-wave valence protons; the respective amplitudes of the s- and d-wave

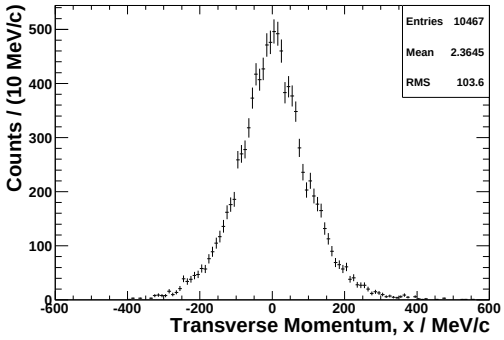

(a) ^{16}F $p_x^{\perp}$, ($E_{rel}(^{16}F) \leq 2$ MeV), C target.

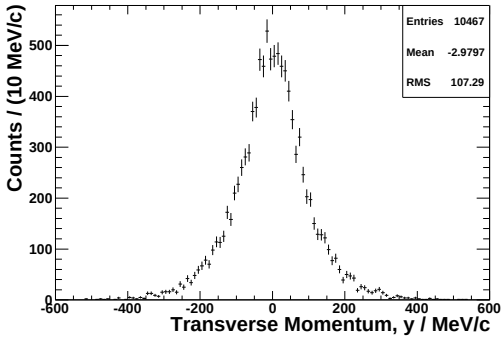

(b) ^{16}F $p_y^{\perp}$, ($E_{rel}(^{16}F) \leq 2$ MeV), C target.

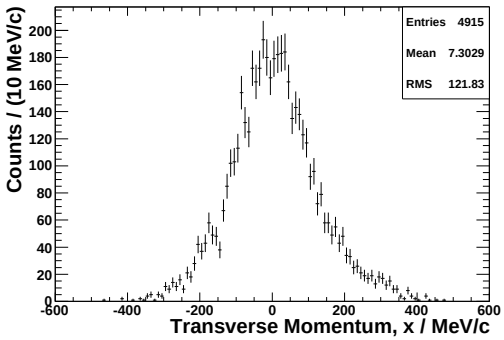

(c) ^{16}F $p_x^{\perp}$, ($E_{rel}(^{16}F) > 2$ MeV), C target.

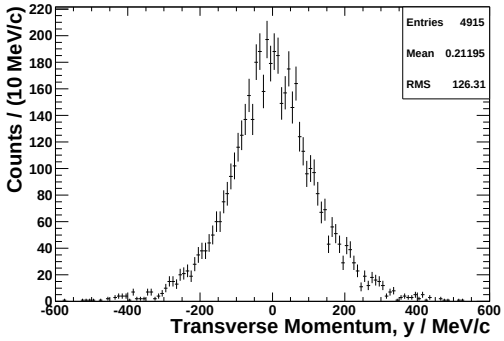

(d) ^{16}F $p_y^{\perp}$, ($E_{rel}(^{16}F) > 2$ MeV), C target.

Figure 6.13: Transverse momentum distributions of ^{16}F (^{15}O+p) resulting from one-proton knockout on ^{17}Ne. Shown are the projections along x (left column) and along y (right columns), which are measured in the dispersive and the non-dispersive plane, respectively. The first row depicts the distributions arising from the condition of the ^{16}F relative-energy being smaller than the chosen threshold value of 2 MeV, which corresponds to the knockout from halo states as suggested in chapter 6.2.2. The second row, in contrast, shows the distributions for a relative energy of ^{16}F larger then 2 MeV, which has been attributed to stemming from ^{17}Ne core knockout.

distributions, as well as the common x offset, were parameters of the fit. These distributions have been calculated by C. Bertulani [37], using the MOMDIS computer code [38].[12] According to the apparent acceptance, the x-projection distribution has been used and fitted within the limits of ±400 MeV/c, only, whereas for the y-projection distribution those

[12] As one of its features, the MOMDIS code allows for the calculation of longitudinal and transverse momentum distributions of the heavy, core-like, reaction residues stemming from stripping (knockout) and/or diffractive breakup reactions of loosely bound (core + nucleon) nuclei on light targets (^{9}Be or ^{12}C) at relativistic energies in inverse kinematics. The core-nucleon potential is parametrised in terms of a radial nuclear (Woods-Saxon plus spin-orbit), and a Coulomb potential; in the present case of ^{17}Ne, a ^{15}O+p system has been modelled in which the potential parameters have been adjusted to reproduce the known binding of (either of) the valence protons in ^{17}Ne relative to the respective s or d resonance states in the unbound ^{16}F, ∼1582 keV and ∼2058 keV. Before fitting them to the data, the calculated distributions have been broadened by the experimental x or y resolution as described in chapter 6.4.2.

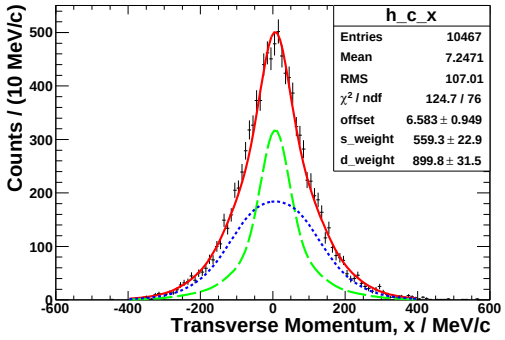

(a) ^{16}F $p_x^{\perp}$, ($E_{rel}(^{16}F) \leq 2$ MeV), C target.

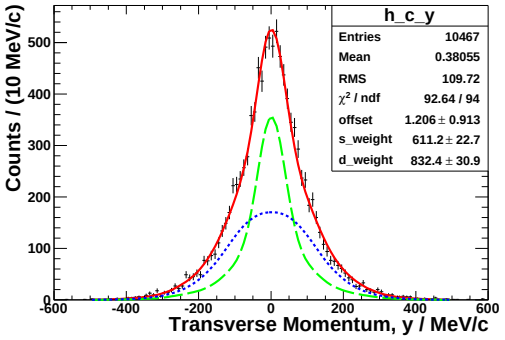

(b) ^{16}F $p_y^{\perp}$, ($E_{rel}(^{16}F) \leq 2$ MeV), C target.

Figure 6.14: Transverse-momentum distribution of ^{16}F, after one-proton knockout from halo states in ^{17}Ne on the C target, *via* the condition of $\leq$2 MeV of ^{16}F (^{15}O+p) relative energy. The x component (a) is compared to the y component (b). The experimental data (black crosses, indicating statistical uncertainty) is described as a superposition (red-solid line) of normalised distributions that represent the ^{16}F fragment's transverse-momentum distribution after knockout from ^{17}Ne of either an s-wave proton (green-dashed line) or a d-wave proton (blue-dotted line). The distributions have been calculated by C. Bertulani using the MOMDIS code [37,38], broadened by the experimental resolution (see chapter 6.4.2), and have finally been fitted to the data (within $\pm$400 MeV/c in x and $\pm$500 MeV/c in y), with the s and d amplitudes (weights) and a common x offset as free parameters.

limits are $\pm$500 MeV/c. In a single-particle picture, in which s^2- and d^2-states are the only possible configurations for ^{17}Ne's two valence protons so that the sum of their weights is two[13], $w(s^2) + w(d^2) = 2$, the s- and d-weights are extracted from the relative weights of the s-wave and d-wave fitting functions. The results obtained for the s-weight per proton are summarised in table 6.4.

s^2-content of the two valence protons in the ^{17}Ne ground state (%)	
x-projection	y-projection
38.3 $\pm$ 1.3	42.3 $\pm$ 1.3

Table 6.4: s^2 content in the ^{17}Ne ground state, extracted from the ^{16}F transverse momentum projections by weighted fitting using the calculated distributions by [37].

From those two measurements, in x and in y, combined with the calculation by [37], a χ^2-weighted average of $w(s^2)_{avg}$=40.8 $\pm$ 1.3$_{stat}$ $\pm$ 4.0$_{syst}$ % can be derived. This value is in good agreement with the value predicted by Grigorenko et al. [5], and in even very good agreement with the measurement/calculation by Geithner/Neff [14].

[13] In other words, the spectroscopic factor of either of the two protons — shared between s- and d-configuration — equals "1", so that the sum of both makes "2", in that picture.

7

Conclusions and Outlook

The transverse-momentum distributions from the carbon-induced one-proton-knockout channels have been interpreted and compared to model calculations. Under certain approximations, they have been linked to the s^2/d^2-configuration mixture of the two valence protons in the ^{17}Ne ground state, which was under vivid discussion in the past. A value of $40.8 \pm 1.3_{\mathrm{stat}} \pm 4.0_{\mathrm{syst}}$ % of s-wave probability has been deduced from the analysis of the x and y projections of the ^{16}F transverse-momentum distributions stemming from the carbon-induced knockout and diffraction of a proton from the halo of ^{17}Ne.
As a second aspect of this thesis, it was possible to implement upgrades to the detection capabilities of the R^{3}B/LAND reaction setup at GSI — in terms of the additional readout for high-energy protons in the Crystal Ball, together with a new silicon-strip array. It enables the use of proton-induced quasi-free-scattering reactions as a clean spectroscopic tool for studying single-particle properties of exotic nuclei. It was shown that such quasi-free-scattering reactions caused by the proton-content of a CH_2 target can be very cleanly identified by the angular correlations of the protons and separated from a kinematically unspecific broad background caused by the carbon content. Further desirable steps, both for the analysis of the ^{17}Ne data, as well as in general terms, are outlined hereafter.
Experimentally, the ^{16}F relative-energy spectrum must be understood in greater detail. With the help of a simulation, the efficiency and acceptance of the used tracking procedure can be determined in order to obtain a reliable correction for the energy-differential cross-section measurement. An inter-strip position-correction must be performed for the silicon-strip detectors, in order to improve their resolution. A more realistic ToF calculation and calibration in both the fragment and the proton tracking, including a continuous energy-loss calculation with a code such as ATIMA, is encouraged for the prospect of a higher longitudinal momentum resolution. Thus, with a better excitation-energy resolution, also the separation between the different ^{16}F states may become clearer, and an identification of halo- and core-knockout-based states will be clearer and easier to quantify. To complete the picture of the ^{16}F excitation spectrum, the inclusion of coincident γ-rays, *e.g.*, from excited ^{15}O states, must be performed. It is foreseen to modify and improve the proton and gamma addback algorithm for this purpose, in order to further suppress the bremsstrahlung background, and also to improve the hit-pattern-recognition routines. Simulations such as with R3BRoot are foreseen to guide and monitor such improvements, and can also be used to determine the proton and gamma efficiencies of the Crystal Ball in a consistent manner, as well as the energy-dependent response to the recoil protons. Further insight into the structure of ^{17}Ne will be gained from studying the angle and energy correlations between the final-state reaction residues, *i.e.*, within ^{15}O+p+p. Such investigations are already in progress.
A key ingredient to a reasonable interpretation of the experimental data, in terms of the observables that characterise the nuclear structure, is the understanding of the influence of the experimental technique, *i.e.*, the reaction mechanisms. For the presented example of the ^{16}F transverse-momentum distribution obtained from knockout/diffraction reactions in inverse kinematics, the necessary framework already exists in the form of certain programs,

such as the MOMDIS code used for the extraction of several properties of ^{17}Ne presented as results in this thesis. In the case of quasi-free-scattering reactions — (p,2p), (p,pn), (p,pα) — which are considered to play a major role in the R^{3}B experimental programme in the years to come, the development of a corresponding reaction code has already been initiated by C. Bertulani. In comparison to knockout reactions, a greater level of detail is necessary for the description of quasi-free scattering. Four distinct sub-processes have to be modelled: Firstly, the probing proton enters through a part of the nucleus. Secondly, the scattering process with the nucleon/cluster to be knocked out happens. And thirdly and fourthly, the striking and the struck proton/nucleon exit through a part of the nucleus.Different theoretical models of the structure of ^{17}Ne may be used then as an input to such a reaction code, and the interpretation of the experimental data can start.

As an outlook, from the current R^{3}B/LAND setup at GSI to its R^{3}B future at FAIR, the experimental possibilities promise to be exciting [67,84]. The new synchrotron SIS 100 will deliver primary beams 100 times higher in intensity, up to 10^{12} ions/s at 1.5-2 AGeV. At the same time, the new Super-FRS will provide a much larger acceptance than the existing FRS, prospectively yielding a 1000 times higher secondary-beam intensity than with the current setup. Simulations have shown that the chosen design of a solid graphite target at the Super-FRS will deliver beam intensities of up to 3×10^{11} uranium-ions/bunch [85–87]. Accordingly, many very exotic proton-neutron-asymmetric nuclei up to the driplines will be available for investigation, and quasi-free scattering in inverse kinematics is foreseen as one of the very promising instruments of study. In addition to plastic CH_2 targets, a liquid-hydrogen target is planned for kinematically even cleaner conditions, which are needed for the spectroscopy of the deeply bound s-states. At the present setup, in z component of the reaction vertex in the target cannot be determined to the desired precision due to the target thickness of several millimeters, which causes an uncertainty in the determination of the proton angles of several degrees, also affecting the precision of their energy. With R^{3}B, two layers of silicon-strip detectors are foreseen, allowing for a more precise tracking and angle measurement. The gamma and proton calorimeter CALIFA, surrounding the target, will be a strongly improved version of the current Crystal Ball. It will allow for proton and gamma measurements of much higher precision, due to an improved granularity *via* the use of several thousands of crystals.

A
Crystal Ball Randomisation

This section describes a C programme used to generate random angles within the solid angle of any crystal shape of the Crystal Ball. There is a stand-alone version with an interface to gnuplot in order to visualise the operations, and there is a ROOT-plugin version, which returns a corresponding pair of randomised azimuthal and polar (θ, ϕ) angles, when called with a crystal number.

A.1 Purpose of the Program

For a more realistic description of the Crystal Ball data a randomisation of hits within the solid angle of specific crystals is essential. It is used to plot realistic angular distributions of photon/proton hits. Before only the nominal (central) ϑ and ϕ coordinates of a crystal were used to plot the data, and at most could be box-randomised around those values. Because of that, the resulting spectra exhibited artifacts in terms of overlaps and gaps (figure A.1).

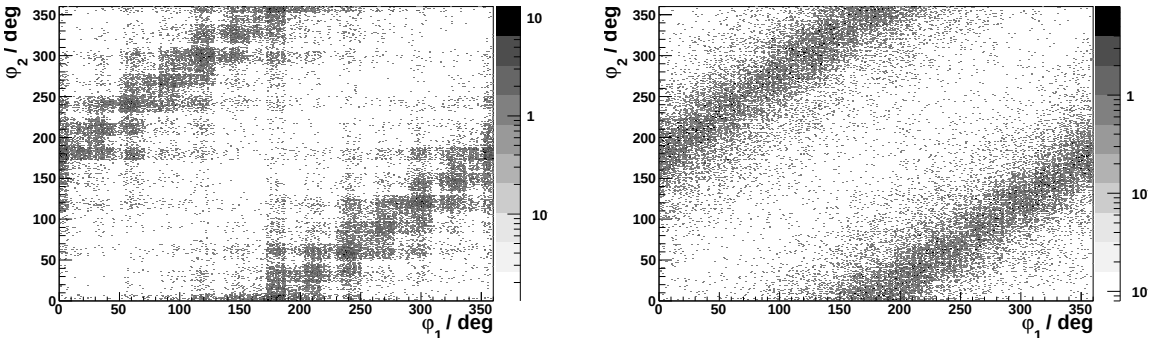

(a) Before: Box-Randomisation.

(b) Now: Realistic Randomisation.

Figure A.1: Azimuthal correlation between two protons (φ_2 vs φ_1) in a ^{17}Ne(p,2p) reaction with a CH_2 target. (a) The crystal angles are randomised in a box around the nominal value φ_0, with $\pm 7.5°$. This creates the visible artifacts showing up as horizontal and vertical bands discussed in the text. (b) The crystal angles are randomised realistically within their solid angle using the algorithm described in this chapter.

A.2 Programme Source and Usage

The code can be checked out from the CVS repository:

```
cvs -R -d /u/fwamers/.mycvsrep co xbtools
```

One will get a directory xbtools with three subdirectories, standalone, rootplugin, and geom_input.

A.2.1 geom_input

Four files bear the information with the necessary geometrical parameters of the Crystal Ball's crystals:

- cb_geometry.dat is a list of the 162 crystals, their reference angles, shape types, and a list of their respective neighbours.
- cb_corners.dat has the (x, y) coordinates of the corner points of the respective polygons of the four crystal face types.
- cb_rotations.dat holds the rotation angles for orienting the crystal faces accordingly towards the centre.
- cb_positions.dat holds the position vectors for placing the crystal faces in order to form a closed shell.

cb_rotations.dat and cb_positions.dat stem from an older Geant3-based package used for the geometrical description of the Crystal Ball.

A.2.2 standalone

The standalone version can readily be used by reading the included README file and following the instructions. The output consists of text files with random points in Cartesian and polar lab coordinates, and there is a 3D gnuplot visualisation (figure A.2).

A.2.3 rootplugin

The rootplugin version also features a README file for guidance. The geom_input directory is copied or linked into the directory of choice, the randomiser functionality can be directly included and invoked in a programme there, as outlined in the following example:

```
#include "xbtools.c"
...
TH1F *h_theta    = new TH1F("theta","theta",180,0,180);
TH1F *h_phi      = new TH1F("phi","phi",360,0,360);
double theta, phi;
...
eventloop
{
        theta=0;
        phi=0;
        ...
        randomiser(crystalNumber,&theta,&phi);
        h_theta->Fill(theta);
        h_phi->Fill(phi);
}
```

A.3 Programme Working Principle

A.3.1 Overview

- The randomiser programme is called with a crystal number as the first argument, and addresses to the theta and phi variables to be filled with randomised angle values.
- A random 2D point is produced within the facial shape of this crystal.
- This point/vector is rotated and moved in space, according to the crystal and its tabulated angles and position.
- The Cartesian coordinates of the transformed point are translated into spherical coordinates, ϑ and φ.

A.3.2 Details

1. When the programme is called with a crystal number as argument, cb_geometry.dat is scanned to check which shape the crystal has, A, B, C, or D. There are 4 different crystal shapes, the regular pentagon A, and the irregular hexagons B, C, and D. The corner point coordinates of those shapes are coming from the original comb-structure drawings. They are stored in the file cb_corners.dat, seven points per crystal, hence the starting and ending (two) points are redundant for the hexagons (pentagon). The common scaling factor "Rd", defining the absolute size of all shapes, is given in the code.

2. A random point is created in the (x,y) plane, with x pointing right, y up; a group of sub-routines checks whether that random point lies within the limiting edges of the chosen crystal's shape. The intrinsic orientation of a shape is different between the technical drawings (and cb_corners.dat) to the ones of the original Geant3 description from which the rotation angles and positioning vectors were obtained. Therefore, the programme rotates the B and C shapes by 270 ° around the z-axis, i.e. it rotates the coordinates of the random points for B and C crystals.
   In the experimental laboratory system L, the x-axis is pointing left (y up, z forward), so finally the x-coordinate of the random point is inverted (x → -x).

3. The original Geant3 coordinate system G is not identical to the Lab system L. When viewed from the L system, the x-axis of the G system is pointing up, y is pointing right, and z backwards. The translation vectors within positions.dat are described in the G system and are transformed into the L system. Their length is scaled to a common value "Rg".

4. A 3-vector (x,y,0) of the random point is created, and its coordinates are scaled with the ratio "Rg/Rd", so the corresponding crystal-shape has the correct size compared to how far out the translation vectors moves it out.

5. Finally, the rotations and translations are performed:

$$x^L_{trans,i} = M^{LG} \cdot \left(R_i^{-1} \cdot M^{GL} \cdot x_i^L - t_i^G \right), \tag{A.1}$$

with

$$R_i^{-1} = \begin{pmatrix} sin\theta_{x,i}cos\phi_{x,i} & sin\theta_{x,i}sin\phi_{x,i} & cos\theta_{x,i} \\ sin\theta_{y,i}cos\phi_{y,i} & sin\theta_{y,i}sin\phi_{y,i} & cos\theta_{y,i} \\ sin\theta_{x,i}cos\phi_{z,i} & sin\theta_{z,i}sin\phi_{z,i} & cos\theta_{z,i} \end{pmatrix}^{-1}, \tag{A.2}$$

and

$$M^{LG} = \begin{pmatrix} 0 & 1 & 0 \\ -1 & 0 & 0 \\ 0 & 0 & -1 \end{pmatrix}, M^{GL} = \begin{pmatrix} 0 & -1 & 0 \\ 1 & 0 & 0 \\ 0 & 0 & -1 \end{pmatrix}. \tag{A.3}$$

In words: For each crystal i the random point/vector x_i^L is created and given in the Lab co-ordinate system L. It is transformed into the Geant system G by M^{GL}, and then rotated by the inverse of the matrix R_i. R_i is the transformation from the crystal-specific daughter co-ordinate system C_i back into the Geant mother system G, so its inverse does the job of rotating from G to C_i. What is left is subtracting the translation vector t_i^G, already given in the Geant system, in order to place the rotated point/vector properly, and finally transforming back into the Lab system by M^{LG}.

6. The Cartesian (lab) coordinates are translated into spherical (lab) coordinates.

A.4 Overlapping Crystals

When having a look at the graphical output, a few unexplainable gaps/overlaps for a couple of crystals were found. There are irregularities in the translation vectors in positions.dat for some of the B and C crystals that are neighbouring the x, y and, z axes, i.e. B-crystals 2, 5, 76, 78, 85, 87, 158, 161, and C-crystals 55, 56, 66, 67, 96, 97, 107, 108. Those slightly wrong numbers were corrected, so no more significant overlaps are visible as shown in figure A.2.

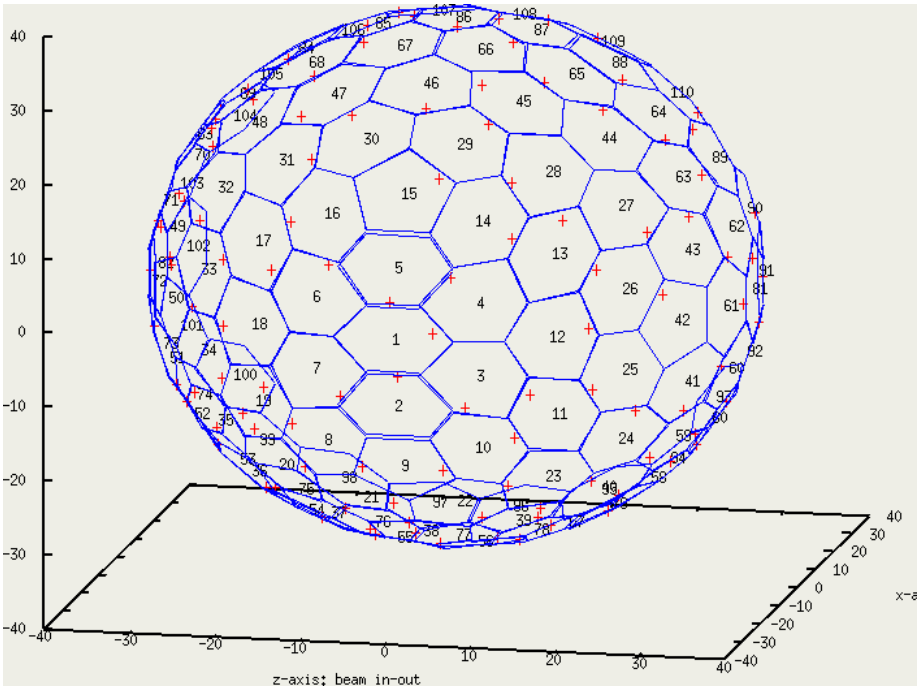

(a) with positions_mod.dat.bck

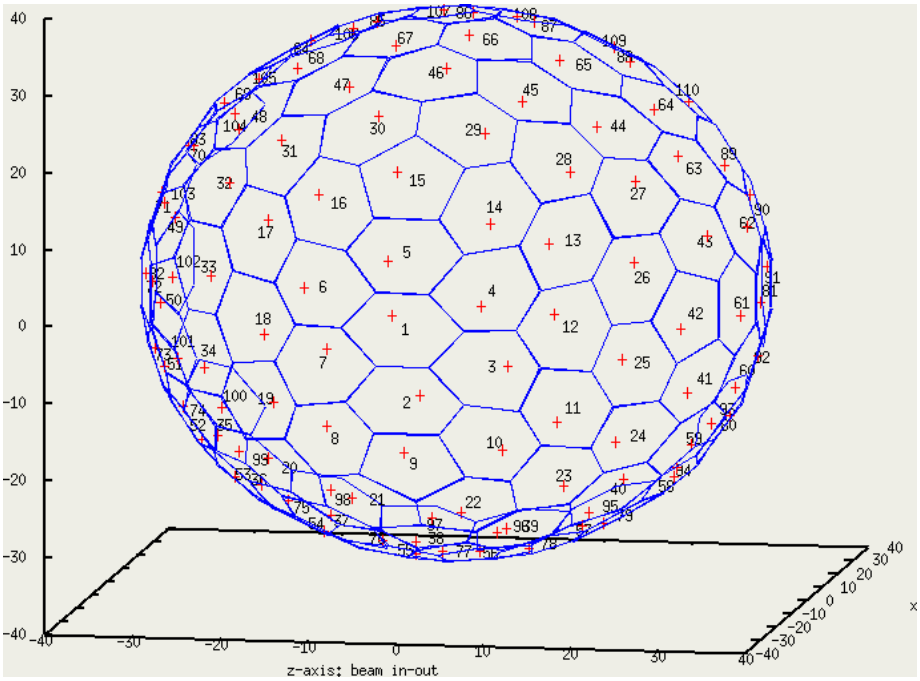

(b) with cb_positions.dat

Figure A.2: a) Crystal grid with old (original) translation vectors. Overlaps and gaps seen with crystals 2 and 5, e.g. b) Crystal grid with new (modified) translation vectors. The small crosses are points randomly created within a crystal's target-oriented face.

B

Simulation of the Crystal Ball Response to High-Energy Protons

The kinematics calculation [78] of free p-p scattering at 500 AMeV (shown in figure 6.6a) have been simulated using the R3BRoot package. The energy loss response of the Crystal Ball for protons at (p,2p) energies is shown in figure B.1.

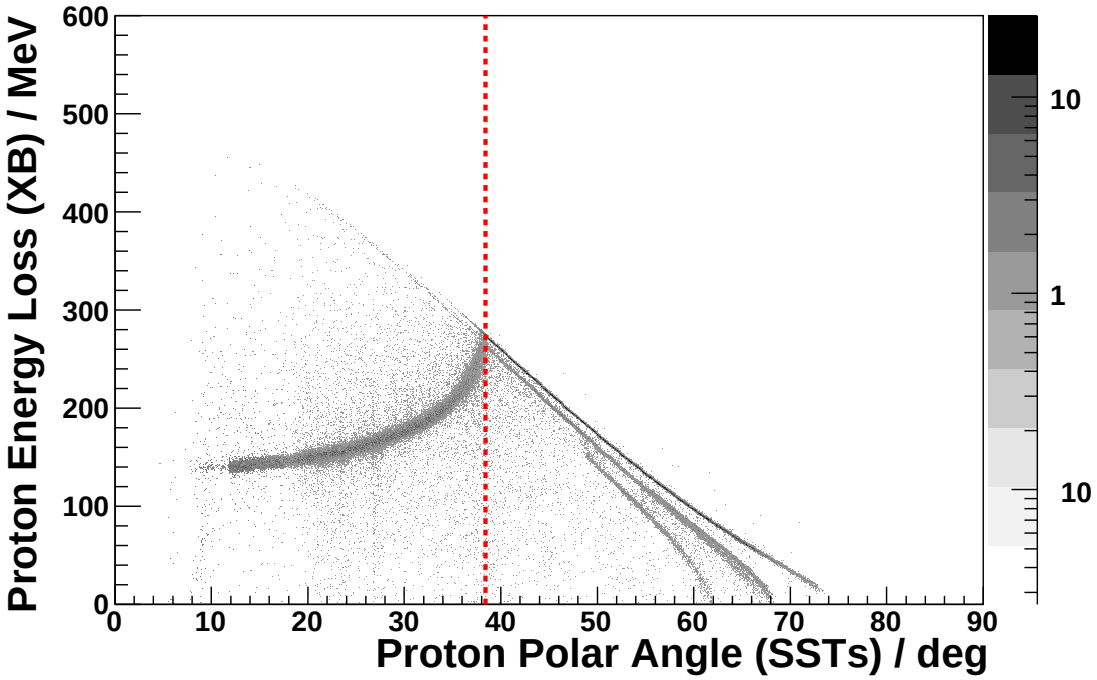

Figure B.1: Experimental response to protons from 500 AMeV p-p scattering, as simulated within R3BRoot. Energy loss is recorded in the XB, angles are measured in the SSTs. Proton punch-through occurs at 38 ° corresponding to 277 MeV, visible in the down-sloping of energy loss towards forward angles.

Proton punch-through (vertical red dashed line) occurs at polar angles below 38.4 °, that is, at energies above 277 MeV, corresponding to 275 MeV when entering the crystals after passing the vacuum chamber shell. The response band for the most probable values of proton energy loss is quite narrow and the expectable energy (loss) resolution is good: About 700 keV σ (0.4 % relative) for stopped protons at 50 °, and about 3 MeV σ (2 % relative) for punch-through protons at 20 °.

C

Crystal Ball Puzzle

(a) Old XB paper model, falling apart. Something needed to be done...

(b) New XB paper model, made from A3-sized printouts. Created together with student Martin Riedel.

Figure C.1: Paper models of the XB, old (a) and new (b).

For a lot of the data analysis related to the Crystal Ball it is handy to have a 3D model of the detector's geometry, for example when trying to understand the angular relations between hits in it. For that purpose a paper model existed, shown in figure C.1a, which was about to fall apart. Therefore a new and geometrically realistic model was designed. It was constructed by a visiting student, Martin Riedel, who cut and glued the hard-paper pieces, before we filled the shell with construction foam, and finally lacquered it (figure C.1b). The following pages contain the drawings for the individual-crystal pieces to be cut and glued. The numbers on the flaps indicate neighbouring numbers/shapes. The drawings as a separate .pdf document can be found on the web:

http://www-linux.gsi.de/~rplag/land02/public_land02/xb_bricolage.pdf.

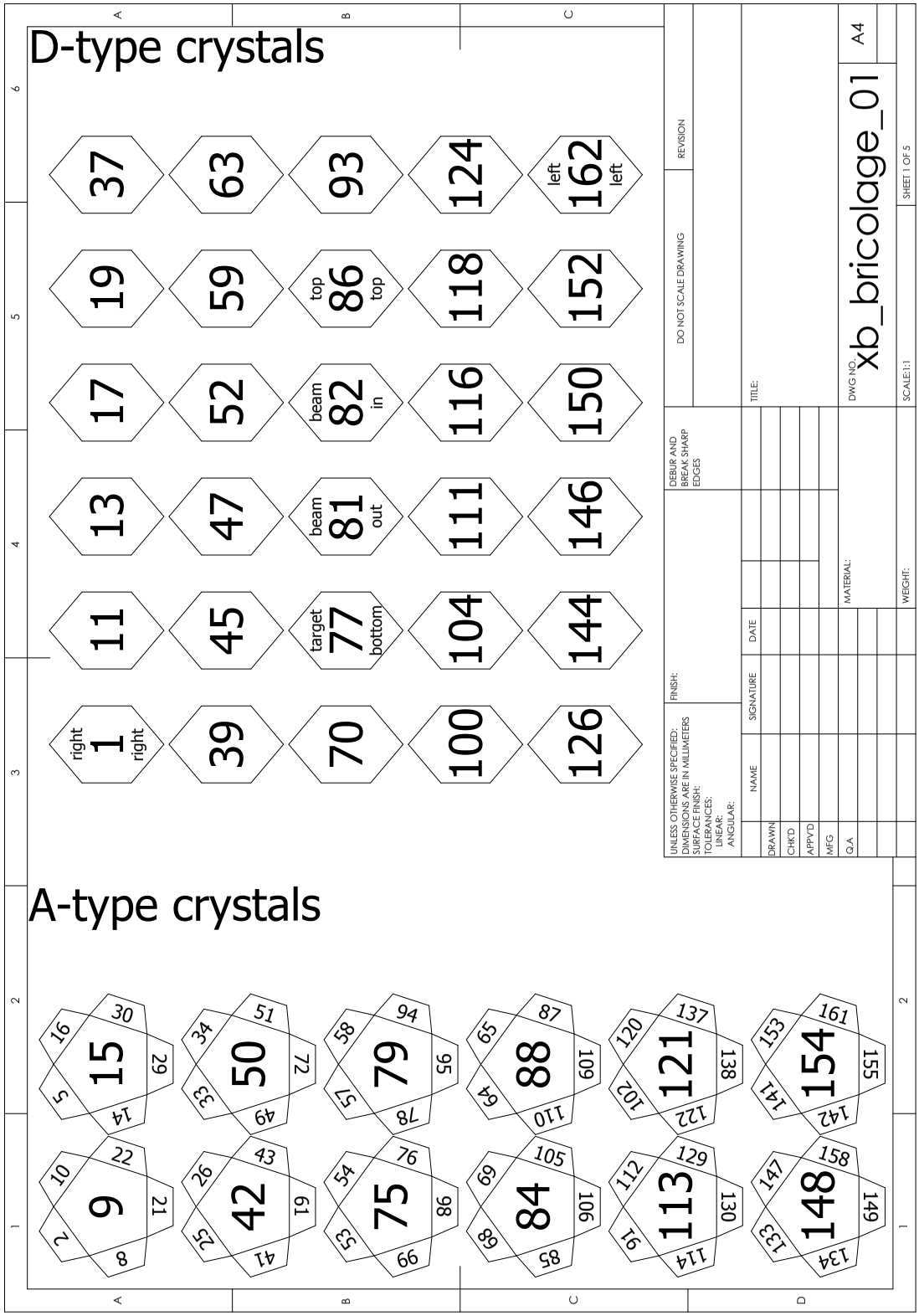
D-type crystals
right 1 right
11
13
17
19
37
39
45
47
52
59
63
target 70
target 77 bottom
beam 81 out
beam 82 in
top 86 top
93
100
104
111
116
118
124
126
144
146
150
152
left 162 left
A-type crystals
9
15
42
50
75
79
84
88
113
121
148
154
DO NOT SCALE DRAWING
REVISION
DEBUR AND BREAK SHARP EDGES
FINISH:
UNLESS OTHERWISE SPECIFIED:
DIMENSIONS ARE IN MILLIMETERS
SURFACE FINISH:
TOLERANCES:
LINEAR:
ANGULAR:
NAME
SIGNATURE
DATE
DRAWN
CHK'D
APPV'D
MFG
Q.A
MATERIAL:
TITLE:
DWG NO. xb_bricolage_01
A4
WEIGHT:
SCALE:1:1
SHEET 1 OF 5

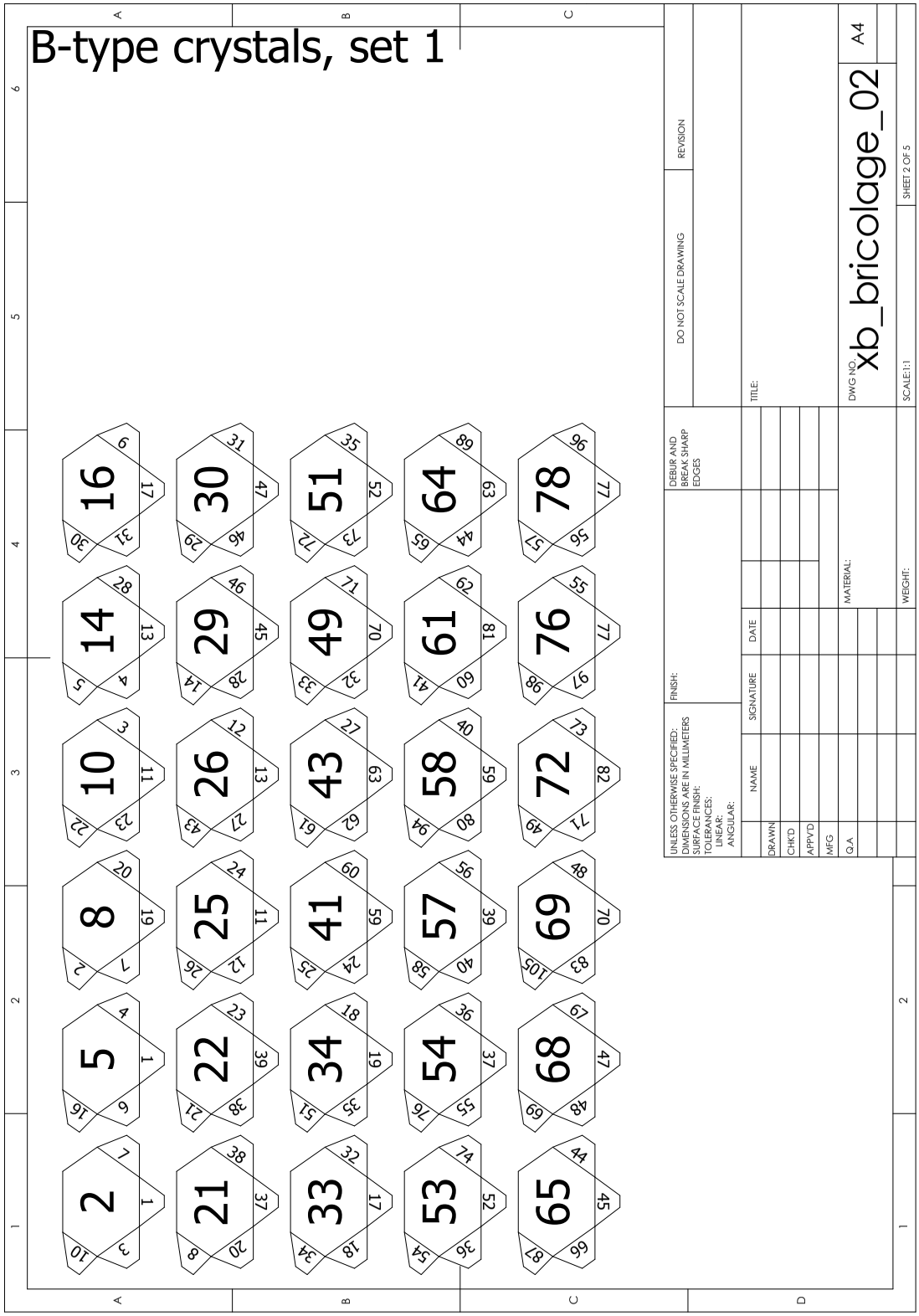
B-type crystals, set 1
2
5
8
10
14
16
21
22
25
26
29
30
33
34
41
43
49
51
53
54
57
58
61
64
65
68
69
72
76
78
UNLESS OTHERWISE SPECIFIED:
DIMENSIONS ARE IN MILLIMETERS
SURFACE FINISH:
TOLERANCES:
LINEAR:
ANGULAR:
FINISH:
DEBUR AND BREAK SHARP EDGES
DO NOT SCALE DRAWING
REVISION
NAME
SIGNATURE
DATE
DRAWN
CHK'D
APPV'D
MFG
Q.A
MATERIAL:
TITLE:
DWG NO.
xb_bricolage_02
A4
WEIGHT:
SCALE:1:1
SHEET 2 OF 5

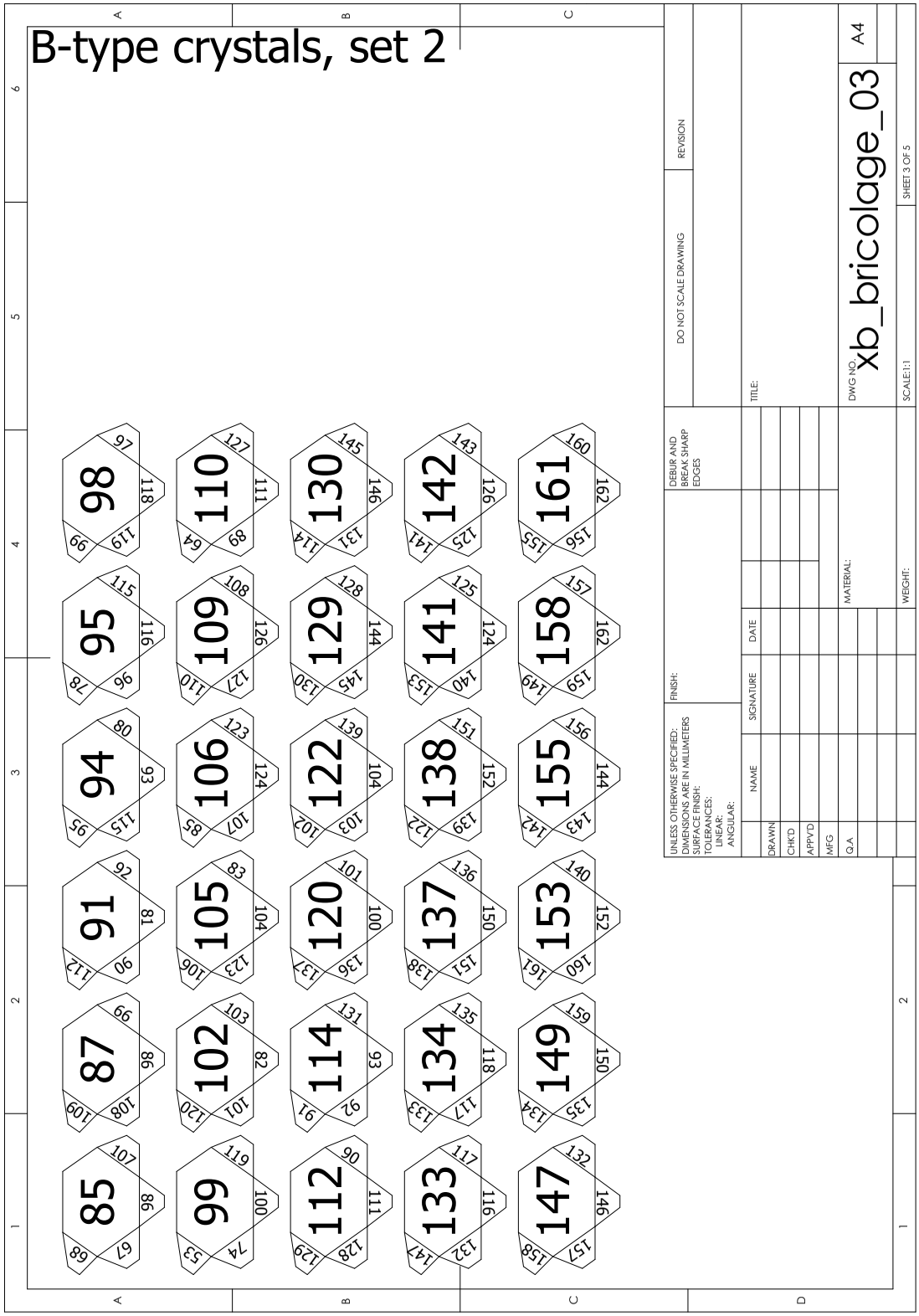
B-type crystals, set 2
98
95
94
91
87
102
114
134
149
110
109
106
105
120
137
153
130
129
122
138
155
142
141
158
161
85
99
112
133
147
DO NOT SCALE DRAWING
REVISION
DEBUR AND BREAK SHARP EDGES
FINISH:
UNLESS OTHERWISE SPECIFIED:
DIMENSIONS ARE IN MILLIMETERS
SURFACE FINISH:
TOLERANCES:
LINEAR:
ANGULAR:
NAME
SIGNATURE
DATE
DRAWN
CHK'D
APPV'D
MFG
Q.A
MATERIAL:
WEIGHT:
TITLE:
DWG NO.
xb_bricolage_03
A4
SCALE:1:1
SHEET 3 OF 5

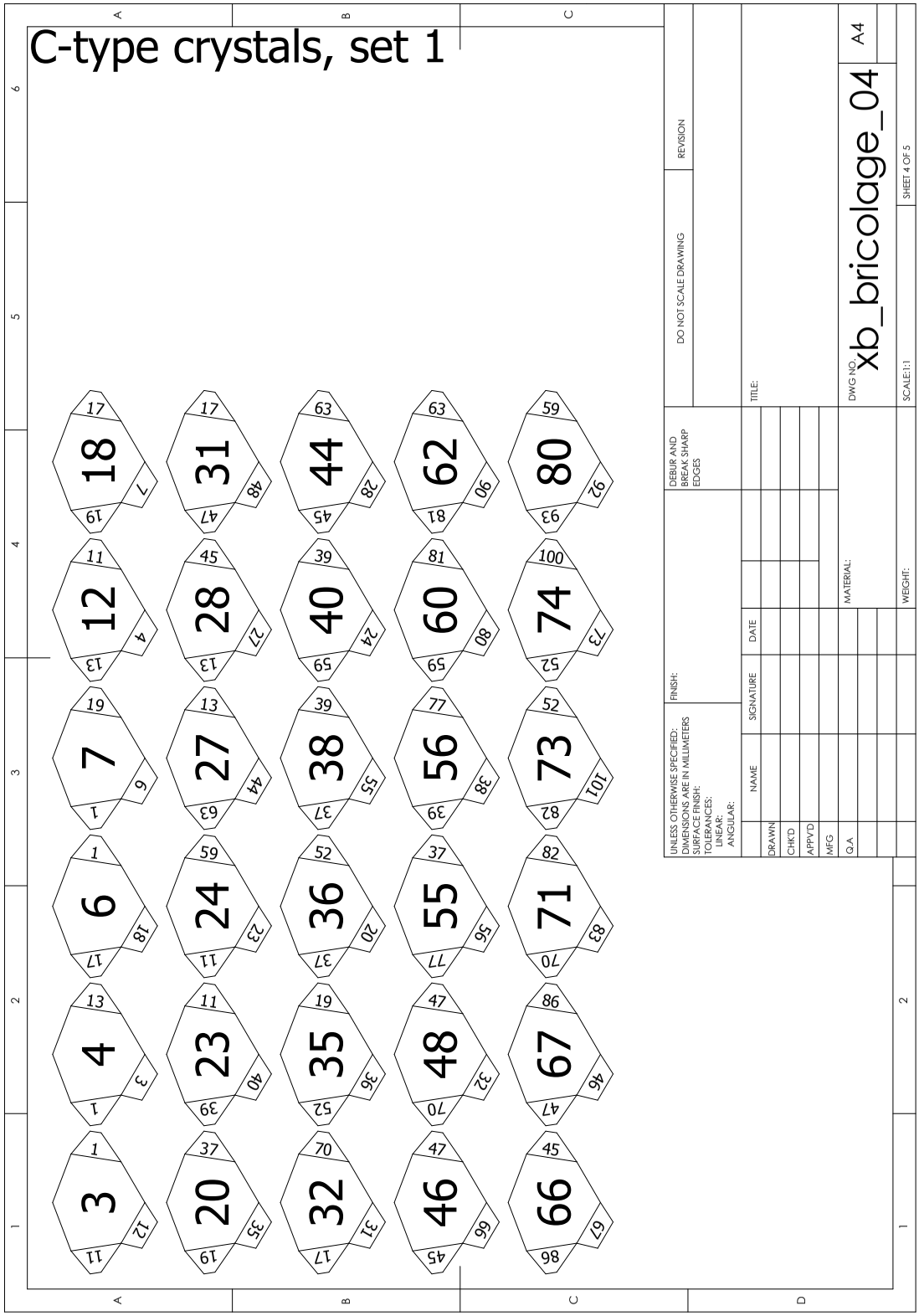
C-type crystals, set 1
3
20
32
46
66
4
23
35
48
67
6
24
36
55
71
7
27
38
56
73
12
28
40
60
74
18
31
44
62
80
DO NOT SCALE DRAWING
REVISION
DEBUR AND BREAK SHARP EDGES
FINISH:
UNLESS OTHERWISE SPECIFIED:
DIMENSIONS ARE IN MILLIMETERS
SURFACE FINISH:
TOLERANCES:
LINEAR:
ANGULAR:
NAME
SIGNATURE
DATE
DRAWN
CHK'D
APPV'D
MFG
Q.A
MATERIAL:
WEIGHT:
TITLE:
DWG NO.
xb_bricolage_04
A4
SCALE:1:1
SHEET 4 OF 5

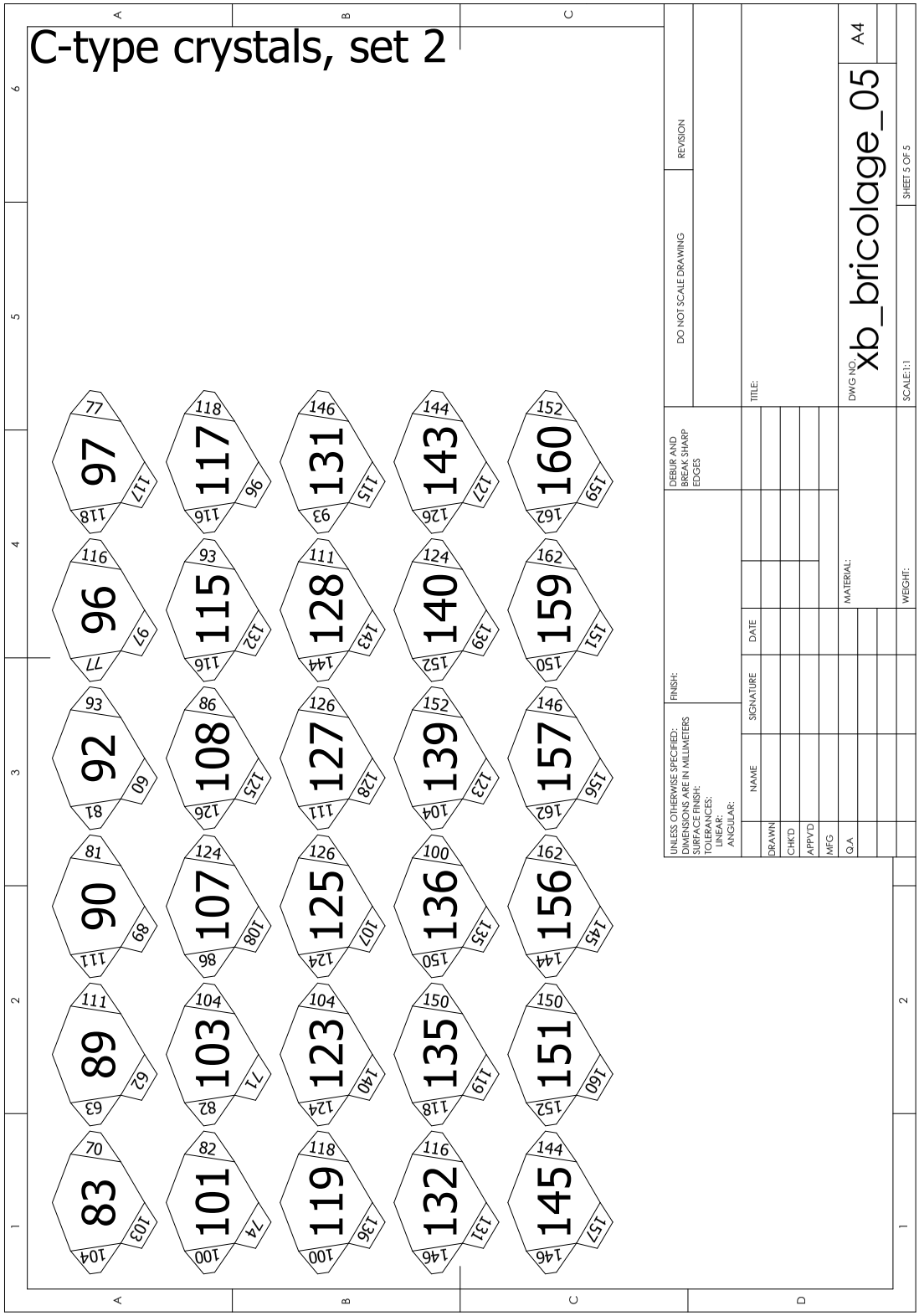
C-type crystals, set 2
97
96
92
90
89
83
117
115
108
107
103
101
131
128
127
125
123
119
143
140
139
136
135
132
160
159
157
156
151
145
DO NOT SCALE DRAWING
REVISION
DEBUR AND BREAK SHARP EDGES
FINISH:
UNLESS OTHERWISE SPECIFIED:
DIMENSIONS ARE IN MILLIMETERS
SURFACE FINISH:
TOLERANCES:
LINEAR:
ANGULAR:
NAME
SIGNATURE
DATE
DRAWN
CHK'D
APPV'D
MFG
Q.A
MATERIAL:
TITLE:
DWG NO.
xb_bricolage_05
A4
WEIGHT:
SCALE:1:1
SHEET 5 OF 5

Bibliography

[1] M. Goeppert-Mayer: *On closed shells in nuclei.* Physical Review, **74** (3), pages 235–239, 1948.

[2] O. Haxel, J. H. D. Jensen, and H. E. Suess: *On the "magic numbers" in nuclear structure.* Physical Review, **75** (11), page 1766, 1949.

[3] R. Kanungo, C. Nociforo, A. Prochazka, T. Aumann, D. Boutin, D. Cortina-Gil, B. Davids, M. Diakaki, F. Farinon, H. Geissel, R. Gernhäuser, J. Gerl, R. Janik, B. Jonson, B. Kindler, R. Knöbel, R. Krücken, M. Lantz, H. Lenske, Y. Litvinov, B. Lommel, K. Mahata, P. Maierbeck, A. Musumarra, T. Nilsson, T. Otsuka, C. Perro, C. Scheidenberger, B. Sitar, P. Strmen, B. Sun, I. Szarka, I. Tanihata, Y. Utsuno, H. Weick, and M. Winkler: *One-Neutron Removal Measurement Reveals ^{24}O as a New Doubly Magic Nucleus.* Physical Review Letters, **102** (15), page 152501, 2009.

[4] M. V. Zhukov and I. J. Thompson: *Existence of proton halos near the drip line.* Physical Reveview C, **52** (6), pages 3505–3508, 1995.

[5] L. V. Grigorenko, Y. L. Parfenova, and M. V. Zhukov: *Possibility to study a two-proton halo in ^{17}Ne.* Physical Review C (Nuclear Physics), **71** (5), page 051604, 2005.

[6] M. Borge, J. Deding, P. G. Hansen, B. Jonson, G. Martinez-Pinedo, P. Møller, G. Nyman, A. Poves, A. Richter, K. Riisager, and O. Tengblad: *Beta-decay to the proton halo state in ^{17}F.* Physics Letters B, **317**, pages 25–30, 1993.

[7] A. Ozawa, M. Fujimaki, S. Fukuda, S. Ito, T. Kobayashi, S. Momota, T. Suzuki, I. Tanihata, K. Yoshida, G. Kraus, and G. Münzenberg: *Measurement of the β-decay branching ratio of ^{17}Ne into the first excited state of ^{17}F.* Journal of Physics G: Nuclear and Particle Physics, **24** (1), pages 143–150, 1998.

[8] A. C. Morton, J. C. Chow, J. D. King, R. N. Boyd, N. P. T. Bateman, L. Buchmann, J. M. D'Auria, T. Davinson, M. Dombsky, and W. Galster: *Beta-delayed particle decay of ^{17}Ne.* Nuclear Physics A, **706** (1-2), pages 15–47, 2002.

[9] A. Ozawa, T. Kobayashi, H. Sato, D. Hirata, I. Tanihata, O. Yamakawa, K. Omata, K. Sugimoto, D. Olson, W. Christie, and H. Wieman: *Interaction cross sections and radii of the mass number A=17 isobar (^{17}N, ^{17}F, and ^{17}Ne).* Physics Letters B, **334**, pages 18–22, 1994.

[10] K. Tanaka, M. Fukuda, M. Mihara, M. Takechi, T. Chinda, T. Sumikama, S. Kudo, K. Matsuta, T. Minamisono, and T. Ohtubo: *Density distribution of proton drip-line nucleus ^{17}Ne.* Nuclear Physics A, **746**, pages 532–535, 2004.

[11] R. Kanungo, M. Chiba, S. Adhikari, D. Fang, N. Iwasa, K. Kimura, K. Maeda, S. Nishimura, Y. Ogawa, and T. Ohnishi: *Possibility of a two-proton halo in ^{17}Ne.* Physics Letters B, **571** (1-2), pages 21–28, 2003.

[12] R. Kanungo, M. Chiba, B. Abu-Ibrahim, S. Adhikari, D. Q. Fang, N. Iwasa, K. Kimura, K. Maeda, S. Nishimura, T. Ohnishi, A. Ozawa, C. Samanta, T. Suda, T. Suzuki, Q. Wang, C. Wu, Y. Yamaguchi, K. Yamada, A. Yoshida, T. Zheng, and I. Tanihata: *Observation of a two-proton halo in ^{17}Ne.* European Physics Journal A, **25** (Supplement 1), pages 327–330, 2005.

[13] L. V. Grigorenko, I. G. Mukha, and M. V. Zhukov: *Prospective candidates for the two-proton decay studies I: structure and Coulomb energies of ^{17}Ne and ^{19}Mg.* Nuclear Physics A, **713** (3-4), pages 372–389, 2003.

[14] W. Geithner, T. Neff, G. Audi, K. Blaum, P. Delahaye, H. Feldmeier, S. George, C. Guénaut, F. Herfurth, A. Herlert, S. Kappertz, M. Keim, A. Kellerbauer, H.-J. Kluge, M. Kowalska, P. Lievens, D. Lunney, K. Marinova, R. Neugart, L. Schweikhard, S. Wilbert, and C. Yazidjian: *Masses and Charge Radii of $^{17-22}Ne$ and the Two-Proton-Halo Candidate ^{17}Ne.* Physical Review Letters, **101** (25), page 252502, 2008.

[15] T. Oishi, K. Hagino, and H. Sagawa: *Diproton correlation in the proton-rich borromean nucleus ^{17}Ne.* Phys. Rev. C, **82** (2), page 024315, 2010.

[16] K. Tanaka, M. Fukuda, M. Mihara, M. Takechi, D. Nishimura, T. Chinda, T. Sumikama, S. Kudo, K. Matsuta, T. Minamisono, T. Suzuki, T. Ohtsubo, T. Izumikawa, S. Momota, T. Yamaguchi, T. Onishi, A. Ozawa, I. Tanihata, and T. Zheng: *Density distribution of ^{17}Ne and possible shell-structure change in the proton-rich sd-shell nuclei.* Physical Review C, **82** (4), page 044309, 2010.

[17] J. Görres, M. Wiescher, and F.-K. Thielemann: *Bridging the waiting points: The role of two-proton capture reactions in the rp process.* Physical Review C, **51** (1), pages 392–400, 1995.

[18] L. Grigorenko, K. Langanke, N. Shul'gina, and M. Zhukov: *Soft dipole mode in ^{17}Ne and the astrophysical 2p capture on ^{15}O.* Physics Letters B, **641** (3-4), pages 254 – 259, 2006.

[19] M. J. Chromik, P. G. Thirolf, M. Thoennessen, B. A. Brown, T. Davinson, D. Gassmann, P. Heckman, J. Prisciandaro, P. Reiter, E. Tryggestad, and P. J. Woods: *Two-proton spectroscopy of low-lying states in ^{17}Ne .* Physical Review C, **66** (2), page 024313, 2002.

[20] I. Mukha, K. Sümmerer, L. Acosta, M. A. G. Alvarez, E. Casarejos, A. Chatillon, D. Cortina-Gil, J. Espino, A. Fomichev, J. E. García-Ramos, H. Geissel, J. Gómez-Camacho, L. Grigorenko, J. Hoffmann, O. Kiselev, A. Korsheninnikov, N. Kurz, Y. Litvinov, I. Martel, C. Nociforo, W. Ott, M. Pfutzner, C. Rodríguez-Tajes, E. Roeckl, M. Stanoiu, H. Weick, and P. J. Woods: *Observation of two-proton radioactivity of ^{19}Mg by tracking the decay products.* Physical Review Letters, **99** (18), page 182501, 2007.

[21] I. Tanihata, H. Hamagaki, O. Hashimoto, Y. Shida, N. Yoshikawa, K. Sugimoto, O. Yamakawa, T. Kobayashi, and N. Takahashi: *Measurements of interaction cross sections and nuclear radii in the light p-shell region.* Physical Review Letters, **55** (24), pages 2676–2679, 1985.

[22] B. Jonson: *Light dripline nuclei.* Physics Reports, **389** (1), pages 1–59, 2004.

[23] P. G. Hansen and B. Jonson: *The neutron halo of extremely neutron-rich nuclei.* Europhysics Letters, **4** (4), page 409, 1987.

[24] J. Al-Khalili *An Introduction to Halo Nuclei* In J. Al-Khalili and E. Roeckl, editors, *The Euroschool Lectures on Physics with Exotic Beams, Vol. I*, volume 651 of *Lecture Notes in Physics*, pages 77–112. Springer Berlin / Heidelberg, 2004.

[25] K. Riisager *Nuclear Halos and Experiments to Probe Them* In J. Al-Khalili and E. Roeckl, editors, *The Euroschool Lectures on Physics with Exotic Beams, Vol. II*, volume 700 of *Lecture Notes in Physics*, pages 1–36. Springer Berlin / Heidelberg, 2006.

[26] A. S. Jensen, K. Riisager, D. V. Fedorov, and E. Garrido: *Structure and reactions of quantum halos.* Reviews of Modern Physics, **76** (1), page 215, 2004.

[27] R. Palit, P. Adrich, T. Aumann, K. Boretzky, B. V. Carlson, D. Cortina, U. Datta Pramanik, T. W. Elze, H. Emling, H. Geissel, M. Hellström, K. L. Jones, J. V. Kratz, R. Kulessa, Y. Leifels, A. Leistenschneider, G. Münzenberg, C. Nociforo, P. Reiter, H. Simon, K. Sümmerer, and W. Walus: *Exclusive measurement of breakup reactions with the one-neutron halo nucleus* ^{11}Be. Physical Review C, **68** (3), page 034318, 2003.

[28] S. N. Ershov, L. V. Grigorenko, J. S. Vaagen, and M. V. Zhukov: *Halo formation and breakup: lessons and open questions.* Journal of Physics G: Nuclear and Particle Physics, **37** (6), page 064026, 2010.

[29] S. Paschalis: *Relativistic One-Nucleon Removal Reactions.* PhD thesis, University of Liverpool, 2008.

[30] P. Hansen and J. Tostevin: *Direct reactions with exotic nuclei.* Annual Review of Nuclear and Particle Science, **53** (1), pages 219–261, 2003.

[31] R. J. Glauber: *Deuteron stripping processes at high energies.* Physical Review, **99** (5), pages 1515–1516, 1955.

[32] H. Simon: *Aufbruchreaktionen der Halokerne* ^{11}Li *und* ^{14}Be *bei relativistischen Energien.* Dissertation, Technische Universität Darmstadt, 1998.

[33] T. Aumann, A. Navin, D. P. Balamuth, D. Bazin, B. Blank, B. A. Brown, J. E. Bush, J. A. Caggiano, B. Davids, T. Glasmacher, V. Guimarães, P. G. Hansen, R. W. Ibbotson, D. Karnes, J. J. Kolata, V. Maddalena, B. Pritychenko, H. Scheit, B. M. Sherrill, and J. A. Tostevin: *One-neutron knockout from individual single-particle states of* ^{11}be. Physical Review Letters, **84** (1), pages 35–38, 2000.

[34] J. Enders, T. Baumann, B. A. Brown, N. H. Frank, P. G. Hansen, P. R. Heckman, B. M. Sherrill, A. Stolz, M. Thoennessen, J. A. Tostevin, E. J. Tryggestad, S. Typel, and M. S. Wallace: *Spectroscopic factors measured in inclusive proton-knockout reactions on* ^{8}B *and* ^{9}C *at intermediate energies.* Physical Review C, **67** (6), page 064301, 2003.

[35] J. Al-Khalili and F. Nunes: *Reaction models to probe the structure of light exotic nuclei.* Journal of Physics G: Nuclear and Particle Physics, **29** (11), page R89, 2003.

[36] T. Aumann. *Private communication.*

[37] C. Bertulani. *Private communication.*

[38] C. Bertulani and A. Gade: *MOMDIS: a Glauber model computer code for knockout reactions.* Computer Physics Communications, **175** (5), pages 372 – 380, 2006.

[39] G. Jacob and T. A. J. Maris: *Quasi-Free Scattering and Nuclear Structure.* Reviews of Modern Physics, **38**, pages 121–142, 1966.

[40] G. Jacob and T. A. J. Maris: *Quasi-Free Scattering and Nuclear Structure. II.* Reviews of Modern Physics, **45**, pages 6–21, 1973.

[41] GSI Helmholtzzentrum für Schwerionenforschung GmbH: *LINAC Department.* `http://www-inj.gsi.de/index.php?section=3`.

[42] GSI Helmholtzzentrum für Schwerionenforschung GmbH: *SIS18.* `http://www.gsi.de/beschleuniger/sis18/sis.html`.

[43] H. Geissel, P. Armbruster, K. H. Behr, A. Brünle, K. Burkard, M. Chen, H. Folger, B. Franczak, H. Keller, O. Klepper, B. Langenbeck, F. Nickel, E. Pfeng, M. Pfützner, E. Roeckl, K. Rykaczewski, I. Schall, D. Schardt, C. Scheidenberger, K. H. Schmidt, A. Schröter, T. Schwab, K. Sümmerer, M. Weber, G. Münzenberg, T. Brohm, H. G. Clerc, M. Fauerbach, J. J. Gaimard, A. Grewe, E. Hanelt, B. Knödler, M. Steiner, B. Voss, J. Weckenmann, C. Ziegler, A. Magel, H. Wollnik, J. P. Dufour, Y. Fujita, D. J. Vieira, and B. Sherrill: *The GSI projectile fragment separator (FRS): a versatile magnetic system for relativistic heavy ions.* Nuclear Instruments and Methods in Physics Research Section B: Beam Interactions with Materials and Atoms, **70** (1-4), pages 286 – 297, 1992.

[44] H. Weick. *Private communication.*

[45] D. Morrissey and B. Sherrill *In-Flight Separation of Projectile Fragments* In J. Al-Khalili and E. Roeckl, editors, *The Euroschool Lectures on Physics with Exotic Beams, Vol. I*, volume 651 of *Lecture Notes in Physics*, pages 113–135. Springer Berlin / Heidelberg, 2004.

[46] LAND Collaboration, T. Blaich, T. W. Elze, H. Emling, H. Freiesleben, K. Grimm, W. Henning, R. Holzmann, G. Ickert, J. G. Keller, H. Klingler, W. Kneissl, R. König, R. Kulessa, J. V. Kratz, D. Lambrecht, J. S. Lange, Y. Leifels, E. Lubkiewicz, M. Proft, W. Prokopowicz, C. Schütter, R. Schmidt, H. Spies, K. Stelzer, J. Stroth, W. Walus, E. Wajda, H. J. Wollersheim, M. Zinser, and E. Zude: *A large area detector for high-energy neutrons.* Nuclear Instruments and Methods in Physics Research Section A: Accelerators, Spectrometers, Detectors and Associated Equipment, **314**, pages 136–154, 1992.

[47] J. Hubele, P. Kreutz, J. C. Adloff, M. Begemann-Blaich, P. Bouissou, G. Imme, I. Iori, G. J. Kunde, S. Leray, V. Lindenstruth, Z. Liu, U. Lynen, R. J. Meijer, U. Milkau, A. Moroni, W. F. J. Müller, C. Ngo, C. A. Ogilvie, J. Pochodzalla, G. Raciti, G. Rudolf, H. Sann, A. Schüttauf, W. Seidel, L. Stuttge, W. Trautmann, and A. Tucholski: *Fragmentation of gold projectiles: From evaporation to total disassembly.* Zeitschrift für Physik A Hadrons and Nuclei, **340**, pages 263–270, 1991 10.1007/BF01294674.

[48] T. Aumann: *Reactions with fast radioactive beams of neutron-rich nuclei.* The European Physical Journal A - Hadrons and Nuclei, **26**, pages 441–478, 2005.

[49] H. T. Johansson: *The DAQ always runs.* Licenciate thesis, Chalmers University of Technology, Göteborg, 2006.

[50] D. Rossi. *Private communication.*

[51] J. Cub, G. Stengel, A. Grünschloß, K. Boretzky, T. Aumann, W. Dostal, B. Eberlein, T. W. Elze, H. Emling, G. Ickert, J. Holeczek, R. Holzmann, J. V. Kratz, R. Kulessa, Y. Leifels, H. Simon, K. Stelzer, J. Stroth, A. Surowiec, and E. Wajda: *A large-area scintillating fibre detector for relativistic heavy ions.* Nuclear Instruments and Methods in Physics Research Section A: Accelerators, Spectrometers, Detectors and Associated Equipment, **402** (1), pages 67 – 74, 1998.

[52] K. Mahata, H. Johansson, S. Paschalis, H. Simon, and T. Aumann: *Position reconstruction in large-area scintillating fibre detectors.* Nuclear Instruments and Methods in Physics Research Section A: Accelerators, Spectrometers, Detectors and Associated Equipment, **608** (2), pages 331 – 335, 2009.

[53] D. Rossi: *Investigation of the Dipole Response of Nickel Isotopes in the Presence of a High-Frequency Electromagnetic Field.* PhD thesis, Johannes Gutenberg-Universität, Mainz, 2010.

[54] C. Wimmer: *To be published.* PhD thesis, Johan Wolfgang Goethe Universität, Frankfurt, 2010.

[55] Gamma Medica, Inc.: *Home | gamma medica.* `http://www.gm-ideas.com/`. 2010.

[56] G. M. Viertel and M. Capell: *The ALPHA Magnetic Spectrometer.* Nuclear Instruments and Methods in Physics Research Section A: Accelerators, Spectrometers, Detectors and Associated Equipment, **419** (2-3), pages 295 – 299, 1998.

[57] B. Alpat, G. Ambrosi, C. Balboni, R. Battiston, A. Biland, M. Bourquin, W. J. Burger, Y. H. Chang, A. E. Chen, N. Dinu, P. Extermann, E. Fiandrini, S. R. Hou, M. Ionica, R. Ionica, W. T. Lin, W. Lustermann, G. Maehlum, M. Menichelli, M. Pauluzzi, N. Produit, D. Rapin, D. Ren, M. Ribordy, H. Sann, D. Schardt, K. Sümmerer, G. Viertel, D. Vité, W. Wallraff, and S. X. Wu: *High-precision tracking and charge selection with silicon strip detectors for relativistic ions.* Nuclear Instruments and Methods in Physics Research Section A: Accelerators, Spectrometers, Detectors and Associated Equipment, **446** (3), pages 522 – 535, 2000.

[58] W. R. Leo: *Techniques for Nuclear and Particle Physics Experiments.* Springer-Verlag, second revised edition edition, 1994.

[59] P. Azzarello: *Tests And Production Of The AMS-02 Silicon Tracker Detectors.* PhD thesis, Université de Genève, 2004.

[60] J. Alcaraz, B. Alpat, G. Ambrosi, P. Azzarello, R. Battiston, B. Bertucci, J. Bolmont, M. Bourquin, W. Burger, M. Capell, F. Cardano, Y. Chang, V. Choutko, E. Cortina, N. Dinu, G. Esposito, E. Fiandrini, D. Haas, S. Haino, H. Hakobyan, M. Ionica, R. Ionica, A. Jacholkowska, A. Kounine, V. Koutsenko, G. Lamanna, A. Lebedev, C. Lechanoine-Leluc, C. Lin, M. Menichelli, S. Natale, A. Oliva, M. Paniccia, M. Pauluzzi, E. Perrin, M. Pohl, D. Rapin, M. Sapinski, I. Sevilla, W. Wallraff, P. Zuccon, and C. Zurbach: *The alpha magnetic spectrometer silicon tracker: Performance results with protons and helium nuclei.* Nuclear Instruments and Methods in Physics Research Section A: Accelerators, Spectrometers, Detectors and Associated Equipment, **593** (3), pages 376 – 398, 2008.

[61] D. Habs, F. S. Stephens, and R. M. Diamond *A proposal for a crystal ball detector system* Technical report, Report LBL-8945, Lawrence Berkeley Laboratory, 1979.

[62] P. Adrich, A. Klimkiewicz, M. Fallot, K. Boretzky, T. Aumann, D. Cortina-Gil, U. Datta Pramanik, T. W. Elze, H. Emling, H. Geissel, M. Hellström, K. L. Jones, J. V. Kratz, R. Kulessa, Y. Leifels, C. Nociforo, R. Palit, H. Simon, G. Surówka, K. Sümmerer, and W. Walus: *Evidence for Pygmy and Giant Dipole Resonances in ^{130}Sn and ^{132}Sn.* Physical Review Letters, **95** (13), page 132501, 2005.

[63] M. AL-Turany, D. Bertini, R. Karabowicz, I. Koenig, and F. Uhlig: *FairRoot Simulation and Analysis Framework.* `http://cbmroot.gsi.de/index.htm`. 2010.

[64] W. Weiter: *Nachweis von Gammastrahlen und Neutronen mit NaJ(Tl)- und BGO-Detektoren und deren Verwendung in einem 4pi-Kristalkugelspektrometer.* Diplomarbeit, Ruprecht-Kars-Universität Heidelberg, 1981.

[65] V. Metag, R. D. Fischer, W. Kühn, R. Mühlhans, R. Novotny, D. Habs, U. V. Helmolt, H. W. Heyng, R. Kroth, D. Pelte, D. Schwalm, W. Hennerici, H. J. Hennrich, G. Himmele, E. Jaeschke, R. Repnow, W. Wahl, E. Adelberger, A. Lazzarini, R. S. Simon, R. Albrecht, and B. Kolb: *Physics with 4π-γ-detectors.* Nuclear Physics A, **409**, pages 331–342, 1983.

[66] V. Metag, D. Habs, K. Helmer, U. v. Helmolt, H. Heyng, B. Kolb, D. Pelte, D. Schwalm, W. Hennerici, H. Hennrich, G. Himmele, E. Jaeschke, R. Repnow, W. Wahl, R. Simon, and R. Albrecht *The Darmstadt-Heidelberg-crystal-ball* In W. von Oertzen, editor, *Detectors in Heavy-Ion Reactions*, volume 178 of *Lecture Notes in Physics*, pages 163–178. Springer Berlin / Heidelberg, 1983.

[67] GSI Helmholtzzentrum für Schwerionenforschung GmbH:. `http://www.gsi.de/fair/experiments/NUSTAR/R3b_e.html`.

[68] FAIR: *Facility for Antiproton and Ion Research: FAIR Home.* `http://www.fair-center.com/`.

[69] GSI Helmholtzzentrum für Schwerionenforschung GmbH: *FAIR Conceptual Design Report.* `http://www.gsi.de/GSI-Future/cdr/`.

[70] H. Geissel, C. Scheidenberger, P. Malzacher, J. Kunzendorf, and H. Weick: *ATIMA*. `http://www-linux.gsi.de/~weick/atima/`.

[71] T. Le Bleis: *Experimental Study of Collective Electric Dipole Mode in Neutron-Rich Nickel Nuclei*. PhD thesis, Université de Strasbourg, 2009.

[72] H. T. Johansson: *Hunting Tools Beyond the Driplines*. PhD thesis, Chalmers University of Technology, Göteborg, 2010.

[73] R. Plag: *Land02: featuring the unofficial guide to the unofficial version of land02*. `http://www-linux.gsi.de/~rplag/land02/`.

[74] Y. Aksyutina: *Light Unbound Nuclear Systems beyond the Dripline*. PhD thesis, Johann Wolfgang Goethe Universitiät, Frankfurt, 2009.

[75] G. F. Knoll: *Radiation Detection and Measurement*. John Wiley & Sons, Inc., 1979.

[76] M. N. Achasov, A. D. Bukin, D. A. Bukin, V. P. Druzhinin, V. B. Golubev, V. N. Ivanchenko, S. V. Koshuba, and S. I. Serednyakov: *Energy calibration of the NaI(T1) calorimeter of the SND detector using cosmic muons*. Nuclear Instruments and Methods in Physics Research Section A: Accelerators, Spectrometers, Detectors and Associated Equipment, **401** (2-3), pages 179 – 186, 1997.

[77] J. Bakken, L. Barone, J. Blaising, T. Boehringer, B. Borgia, D. Boutigny, J. Burq, M. Chemarin, R. Clare, G. Coignet, P. Denes, F. D. Notaristefani, M. Diemoz, C. Dionisi, H. Elmamouni, P. Extermann, S. Falciano, F. Ferroni, G. Gratta, B. Ille, P. Kaaret, Y. Karyotakis, P. Klok, P. Lebrun, P. Lecoq, P. Li, E. Longo, D. Luckey, L. Luminari, J. Martin, M. Micke, U. Micke, G. Morand, S. Morganti, J. Ossmann, P. Piroué, W. Ruckstuhl, S. Salsedo, G. Sauvage, T. Schaad, D. Schmitz, M. Schneegans, D. Stickland, R. Sumner, C. Taylor, E. Valente, M. Vivargent, L. Vuilleumier, W. Walk, R. Weill, and T. Wynen: *High energy cosmic muons and the calibration of the L3 electromagnetic calorimeter*. Nuclear Instruments and Methods in Physics Research Section A: Accelerators, Spectrometers, Detectors and Associated Equipment, **275** (1), pages 81 – 88, 1989.

[78] L. Chulkov. *Private communication*.

[79] J. Taylor. *Private communication*.

[80] L. Chulkov, F. Aksouh, A. Bleile, O. Bochkarev, D. Cortina-Gil, A. Dobrovolsky, P. Egelhof, H. Geissel, M. Hellström, N. Isaev, O. Kiselev, B. Komkov, M. Matos, F. Moroz, G. Münzenberg, M. Mutterer, V. Mylnikov, S. Neumaier, V. Pribora, D. Seliverstov, L. Sergeev, A. Shrivastava, K. Sümmerer, S. Torilov, H. Weick, M. Winkler, and V. Yatsoura: *Quasi-free scattering with ^{6,8}He beams*. Nuclear Physics A, **759** (1-2), pages 43 – 63, 2005.

[81] A. Goldhaber: *Statistical models of fragmentation processes*. Physics Letters B, **53** (4), pages 306 – 308, 1974.

[82] A. Bülling, L. Jansson, K. Jareteg, R. Masgren, G. Risting, and S. Shojaee: *Analysis of CALIFA Detector Prototypes and Silicon Strip Detectors.* Bachelor Thesis, Chalmers University of Technology, 2011.

[83] D. R. Tilley, H. R. Weller, and C. M. Cheves: *Energy levels of light nuclei A = 16-17.* Nuclear Physics A, **564** (1), pages 1 – 183, 1993.

[84] Thomas Aumann: *Prospects of nuclear structure at the future GSI accelerators.* Progress in Particle and Nuclear Physics, **59** (1), pages 3 – 21, 2007 International Workshop on Nuclear Physics 28th Course - Radioactive Beams, Nuclear Dynamics and Astrophysics, Ettore Majorana Center for Scientific Culture.

[85] N. Tahir, V. Kim, A. Matvechev, A. Ostrik, A. Shutov, I. Lomonosov, A. Piriz, J. Lopez Cela, and D. Hoffmann: *High energy density and beam induced stress related issues in solid graphite Super-FRS fast extraction targets.* Laser and Particle Beams, **26** (02), pages 273–286, 2008.

[86] N. Tahir, H. Weick, A. Shutov, V. Kim, A. Matveichev, A. Ostrik, V. Sultanov, I. Lomonosov, A. Piriz, J. Lopez Cela, and D. Hoffmann: *Simulations of a solid graphite target for high intensity fast extracted uranium beams for the Super-FRS.* Laser and Particle Beams, **26** (03), pages 411–423, 2008.

[87] N. Tahir, A. Matveichev, V. Kim, A. Ostrik, A. Shutov, V. Sultanov, I. Lomonosov, A. Piriz, and D. Hoffmann: *Three-dimensional simulations of a solid graphite target for high intensity fast extracted uranium beams for the super-frs.* Laser and Particle Beams, **27** (01), pages 9–17, 2009.

Acknowledgements

This thesis represents work done within four and a half years. Some parts of it may be exclusively my own, but without any doubt the by far largest portion of it was only possible due to the help of, and the encouragement and support by many, many people. These final words shall represent an attempt to express my gratitude towards them.

First of all, I'd like to thank the two supervisors and referees of my thesis, Prof. Dr. Thomas Aumann, and Prof. Dr. Dr. h.c. RUS Dieter H.H. Hoffmann.
Prof. Aumann introduced me to the LAND collaboration and to the R^3B/LAND experimental setup at GSI and supervised my practical work in analysing the data. Prof. Hoffmann helped me tremendously in overcoming the initial difficulties in becoming and being a PhD-student, and he was a mentor who always provided help and advice. Prof. Aumann's and Prof. Hoffmann's great interest in my work, their support and encouragement, but also their patience in the process of completing it are highly appreciated.
I also would like to cordially thank Prof. Dr. Norbert Pietralla for providing the financial support during my time within the HGS-HIRe scholarship programme.

A very special "thanks!" is dedicated to Dr. Haik Simon, a dear colleague within the LAND group at GSI, who sacrificed considerable amounts of his scarce time for proof-reading my manuscripts, improving my understanding of physics in many aspects, and for providing all sorts of general practical help related to my thesis. Within the same breath I want to thank Dr. Tudi Le Bleis, a dear and long-time office-mate and friend, who as well offered great support in the final phase of this work.

I'd like to thank a lot my colleagues who worked (and still work) with me on the still ongoing analysis of the "S318" experiment around ^{17}Ne, for the not only fruitful but also friendly collaboration. Those are in particular Dr. Justyna Marganiec, Dr. Ralf Plag, Dr. Michael Heil, but also our close external collaborators: Dr. Leonid Grigorenko, Prof. Carlos Bertulani, Dr. Leonid Chulkov, and their co-workers.

An important, if not crucial, point to contribute to the success and completion of this thesis has been the professional, but also fantastically good-spirited atmosphere in the LAND group at GSI, and also in whole the R^3B collaboration. Ideas for problem-solving, humour, and mutual practical and moral support - all was and is there. There is no specific priority in the names of the people involved in the following list - if not for a more or less chronological order of how I got to know them. Academical titles are omitted here for brevity: K. Sümmerer, K. Boretzky, A. Chatillon, A. Klimkiewicz, K. Mahata, S. Paschalis, H.T. Johansson, G. Schrieder, D. Rossi, C. Wimmer, Y. Aksyutina, O. Kiselev, A. Bacquias, G. Ickert, K. Larsson, B. Streicher, R. Reifarth, C. Langer, A. Kelić-Heil, V. Ricciardi, V. Föhr, V. Panin, J. Vignote, O. Ershova, O. Lepyoshkina, V. Volkov, C. Caesar, A. Movsesyan, T. Heftrich, M. Heine, D. Gonzales, A. Ignatov, G. Rastrepina, D. Savran and B. Löher.
In the same way I want to thank my external and international colleagues from the NuSTAR and R^3B collaborations that I unfortunately cannot all name here. I spent time with

them on numerous meetings, workshops, and experiments, and those were really good and productive times.

But maybe most of all I would like to thank my family, for their ever-present love, patience, and support. I'd like to thank my parents and my brother for being there when needed. And finally I want to thank the most important person in my life - Thank you, Monica, for all your patience and love!

Eidesstattliche Erklärung

Hiermit erkläre ich, dass ich die vorliegende Dissertation selbständig verfasst, keine anderen als die angegebenen Hilfsmittel verwendet und bisher noch keinen Promotionsversuch unternommen habe.

Darmstadt, im April 2011